



# 1 Multi-year simulations at kilometre scale with the Integrated 2 Forecasting System coupled to FESOM2.5/NEMOv3.4

3 Thomas Rackow<sup>1,2</sup>, Xabier Pedruzo-Bagazgoitia<sup>1</sup>, Tobias Becker<sup>1</sup>, Sebastian Milinski<sup>1</sup>, Irina Sandu<sup>1</sup>,  
4 Razvan Aguridan<sup>1</sup>, Peter Bechtold<sup>1</sup>, Sebastian Beyer<sup>2</sup>, Jean Bidlot<sup>1</sup>, Souhail Boussetta<sup>1</sup>, Michail  
5 Diamantakis<sup>1</sup>, Peter Dueben<sup>1</sup>, Emanuel Dutra<sup>3</sup>, Richard Forbes<sup>1</sup>, Helge F. Goessling<sup>2</sup>, Ioan Hadade<sup>1</sup>, Jan  
6 Hegewald<sup>4</sup>, Sarah Keeley<sup>1</sup>, Lukas Kluft<sup>5</sup>, Nikolay Koldunov<sup>2</sup>, Alexei Koldunov<sup>2</sup>, Tobias Kölling<sup>5</sup>, Josh  
7 Kousal<sup>1</sup>, Kristian Mogensen<sup>1</sup>, Tiago Quintino<sup>1</sup>, Inna Polichtchouk<sup>1</sup>, Domokos Sármany<sup>1</sup>, Dmitry  
8 Sidorenko<sup>2</sup>, Jan Streffing<sup>2</sup>, Birgit Sützl<sup>1</sup>, Daisuke Takasuka<sup>6,7</sup>, Steffen Tietsche<sup>1</sup>, Mirco Valentini<sup>1</sup>, Benoît  
9 Vannière<sup>1</sup>, Nils Wedi<sup>1</sup>, Lorenzo Zampieri<sup>8</sup>, and Florian Ziemer<sup>9</sup>

10 <sup>1</sup>European Centre for Medium-Range Weather Forecasts (ECMWF), Bonn, Germany; Reading, UK

11 <sup>2</sup>Alfred Wegener Institute, Helmholtz Centre for Polar and Marine Research (AWI), Bremerhaven, Germany

12 <sup>3</sup>Portuguese Weather Service (IPMA), Lisbon, Portugal

13 <sup>4</sup>Gauß-IT-Zentrum, Braunschweig University of Technology (GITZ), Braunschweig, Germany

14 <sup>5</sup>Max-Planck-Institute for Meteorology (MPI-M), Hamburg, Germany

15 <sup>6</sup>Atmosphere and Ocean Research Institute (AORI), The University of Tokyo, Kashiwa, Japan

16 <sup>7</sup>Japan Agency for Marine-Earth Science and Technology (JAMSTEC), Yokohama, Japan

17 <sup>8</sup>Foundation Euro-Mediterranean Center on Climate Change (CMCC), Bologna, Italy

18 <sup>9</sup>Deutsches Klimarechenzentrum (DKRZ), Hamburg, Germany

19 *Correspondence to:* Thomas Rackow (thomas.rackow@ecmwf.int)

20 **Abstract.** We report on the first multi-year km-scale global coupled simulations using ECMWF's Integrated Forecasting System (IFS)  
21 coupled to both the NEMO and FESOM ocean-sea ice models, as part of the H2020 Next Generation Earth Modelling Systems (nextGEMS)  
22 project. We focus mainly on the two unprecedented IFS-FESOM coupled setups, with an atmospheric resolution of 2.8km and 4.4km,  
23 respectively, and the same spatially varying ocean resolution that reaches locally below 5km grid-spacing. This is enabled by a refactored  
24 ocean model code that allows for more efficient coupled simulations with IFS in a single-executable setup, employing hybrid parallelisation  
25 with MPI and OpenMP. A number of shortcomings in the original NWP-focussed model configurations were identified and mitigated over  
26 several cycles collaboratively by the modelling centres, academia, and the wider nextGEMS community. The main improvements are (i)  
27 better conservation properties of the coupled model system in terms of water and energy balance, which benefit also ECMWF's operational  
28 9 km IFS-NEMO model, (ii) a realistic top-of-the-atmosphere (TOA) radiation balance throughout the year, (iii) improved intense  
29 precipitation characteristics, and (iv) eddy-resolving features in large parts of the mid- and high-latitude oceans (finer than 5km grid-spacing)  
30 to resolve mesoscale eddies and sea ice leads. New developments made at ECMWF for a better representation of snow and land use, including  
31 a dedicated scheme for urban areas, were also tested on multi-year timescales. We provide first examples of significant advances in the  
32 realism and thus opportunities of these km-scale simulations, such as a clear imprint of resolved Arctic sea ice leads on atmospheric  
33 temperature, impacts of km-scale urban areas on the diurnal temperature cycle in cities, and better propagation and symmetry characteristics  
34 of the Madden-Julian Oscillation.



## 35 **1 Introduction**

36 Current state-of-the-art climate models with typical spatial resolutions of 50-100km still rely heavily on parametrizations for  
37 under-resolved processes, such as deep convection, the effects of sub-grid orography and gravity waves in the atmosphere, or  
38 the effects of meso-scale eddies in the ocean. The emerging new generation of km-scale climate models can explicitly represent  
39 and combine several of these energy-redistributing small-scale processes and physical phenomena that were historically  
40 approximated or even neglected in coarse-resolution models (Palmer 2014). The advantage of km-scale models thus lies in  
41 their ability to more directly represent phenomena such as tropical cyclones (Judt et al. 2021) or the atmospheric response to  
42 small-scale features in the topography, e.g. mountains, orography gradients, lakes, urban areas, and cities. The distribution and  
43 intensity (and particularly the extremes) of precipitation (Judt and Rios-Berrios 2021), winds, and potentially also temperature  
44 will be different at improved spatial resolution. Importantly, features of deep convection start to be explicitly resolved at km-  
45 scale resolutions. This does not only improve the local representation of the diurnal cycle, convective organisation, and the  
46 propagation of convective storms (Prein et al., 2015; Satoh et al., 2019; Schär et al., 2020), but can also impact the large-scale  
47 circulation (Gao et al. 2023). Ultimately, the replacement of parametrizations by explicitly resolved atmospheric dynamics is  
48 also expected to help narrowing the still large uncertainty range of cloud-related feedbacks and thus climate sensitivity (Bony  
49 et al. 2015; Stevens et al. 2016).

50  
51 Km-scale resolutions are also particularly beneficial for the ocean, where mesoscale ocean eddies (Frenger et al. 2013), leads  
52 opening up in the sea ice cover, and the response of oceanic heat transport to the presence of narrow canyons (Morrison et al.  
53 2020) can be studied directly. The small scales in the ocean, in particular mesoscale ocean eddies, have large-scale impacts on  
54 climate and control the distribution of nutrients, heat uptake, and carbon cycling (Hogg et al., 2015). Eddies also play an  
55 important role in the comprehensive response of the climate system to warming (Hewitt et al. 2022; Rackow et al. 2022,  
56 Griffies et al. 2015). In addition to the influence of mesoscale ocean features on the predictability of European weather  
57 downstream of the Gulf Stream area (Keeley et al., 2012), it has been proposed that higher-resolution simulations can enhance  
58 the representation of local heterogeneities in the sea-ice cover (Hutter et al., 2022). Via their impact on small-scale ocean  
59 features such as eddies, atmospheric storms can impact deep water formation in the Labrador Sea (Gutjahr et al. 2022), an  
60 ocean region of global significance because of its role in the meridional overturning circulation of the ocean. Coupled ocean-  
61 atmosphere variability patterns such as the El Nino-Southern Oscillation (ENSO), the largest signal of interannual variability  
62 on Earth, may also benefit from km-scale resolutions since ENSO-relevant ocean meso-scale features (Wengel et al. 2021) as  
63 well as westerly wind bursts should be better resolved.

64  
65 High-resolution simulations pose significant challenges in terms of numerical methods, data management, storage and analysis  
66 (Schär et al., 2020). To exploit the potential of km-scale modelling, it is essential to develop scalable models that can run  
67 efficiently on large supercomputers and take advantage of the next generation of exascale computing platforms (Bauer et al.,



68 2021, Taylor et al., 2023). Global atmosphere-only climate simulations at km-scale were pioneered by the NICAM group  
69 (Nonhydrostatic ICosahedral Atmospheric Model) almost two decades ago. On sub-seasonal to seasonal time scales, a global  
70 aqua-planet configuration at 3.5km resolution was performed (Tomita et al. 2005), and the MJO was realistically reproduced  
71 at 7km and 3.5km resolutions (Miura et al. 2007). In the last decade, the NICAM group as well as the European Centre for  
72 Medium-Range Weather Forecasts (ECMWF) ran simulations on climate time scales around 10-15km resolution. In particular,  
73 14km resolution 30-year AMIP (Kodama et al. 2015) and HighResMIP simulations (Kodama et al. 2021) were performed with  
74 NICAM. During Project Athena, the sensitivity to horizontal resolution of ECMWF's Integrated Forecasting System in terms  
75 of climate and seasonal predictive skill has been analysed at resolutions up to 10km via many 13 months simulations (totalling  
76 several decadal simulations), and with help of a 48-year AMIP-style simulation plus future time slices at 15km resolution  
77 (Jung et al. 2012). Recently, the NICAM group presented 10-year AMIP simulations at 3.5km using an updated NICAM  
78 version (Takasuka et al. 2024). Other modelling groups around the world have also increased their model resolution towards  
79 the km-scale, and many participated in the recent DYAMOND intercomparison project (DYNAMICS of the Atmospheric general  
80 circulation Modeled On Non-hydrostatic Domains) with a grid spacing as fine as 2.5km, simulations running over 40 days,  
81 and some of them already coupled to an ocean (Stevens et al., 2019).

82  
83 While different modelling groups push global atmosphere-only simulations towards unprecedented resolutions, e.g. 220m  
84 resolution in short simulations with NICAM, another scientific frontier has emerged around running km-scale simulations on  
85 multi-year timescales, coupled to an equally refined ocean model. Indeed, in the last years, there have been several examples  
86 of km-scale simulations that have been run on up to monthly and seasonal timescales (Stevens et al., 2019, Wedi et al., 2020),  
87 but not many beyond these timescales, and not yet with a km-scale ocean (Miyakawa et al. 2017). This is due to the fact that  
88 even the most efficient high-resolution coupled models are computationally expensive and require substantial resources to run.  
89 This in turn limits the number of simulations and realisations that can be performed, making it difficult to calibrate and optimise  
90 the model settings. Coarser resolution models have been tuned for decades to be relatively reliable on the spatial scales that  
91 they can resolve, and to match the historical period well for which high-quality observations are available. Nevertheless, this  
92 is often achieved by compensating errors, which can not necessarily be expected to compensate in a warming climate. These  
93 models also have some long-standing biases that can locally be larger than the interannual variability or the climate change  
94 signal (Rackow et al. 2019, Palmer and Stevens, 2019). The lack of explicitly simulated small-scale features is one potential  
95 source for these long-standing biases in weather and climate models (Schär et al., 2020). Coarser resolution models also  
96 struggle with answering some important climate questions, such as what will happen to extreme events in a warmer world, and  
97 with providing accurate information on climate changes at regional scale.

98  
99 The European H2020 Next Generation Earth Modelling Systems (nextGEMS) project aims to build a new generation of eddy-  
100 and storm-resolving global coupled Earth System Models to be used for multi-decadal climate projections at km-scale. By  
101 providing globally consistent information at scales where extreme events and the effects of climate change matter and are felt,



102 global km-scale multi-decadal projections will support the increasing need to provide localised climate information to inform  
103 local adaptation measures. The nextGEMS models build upon models that are also operationally used for numerical weather  
104 prediction (NWP): ICON, which is jointly developed by DWD and MPI-M (Hohenegger et al., 2023), and the Integrated  
105 Forecasting System (IFS) of ECMWF, coupled to the NEMO and FESOM ocean models. NextGEMS revolves around a series  
106 of hackathons, in which the simulations performed with the two models are examined in detail by an international community  
107 of more than 100 participants, followed by new model development iterations or ‘Cycles’. The nextGEMS models have been  
108 (re-)designed for scalability and portability across different architectures (Satoh et al. 2019, Schulthess et al. 2019, Müller et  
109 al. 2019, Bauer et al. 2020, Bauer, Quintino, and Wedi 2022) and lay the foundation for the Climate Change Adaptation Digital  
110 Twin developed in the EU’s Destination Earth initiative (DestinE).

111  
112 The operational NWP system at ECMWF uses an average 9km grid-spacing for the atmosphere coupled to an ocean at 0.25°  
113 spatial resolution (NEMO v3.4), which translates to a horizontal grid spacing of about 25km along the equator. While many  
114 coupled effects such as the atmosphere-ocean interactions during tropical cyclone conditions (Mogensen et al. 2017) can be  
115 realistically simulated at this resolution, ocean eddies in the mid latitudes are still only ‘permitted’ due to their decreasing size  
116 with latitude (Hallberg 2013). This setup is far from our goal to explicitly resolve mesoscale ocean eddies all around the globe  
117 (Sein et al., 2017). In this study, we therefore focus mainly on two configurations in which km-scale versions of IFS (one at  
118 2.8km and one at 4.4km grid spacing in the atmosphere and land) are coupled to the FESOM2.5 ocean-sea ice model at about  
119 5km grid spacing, developed by the Alfred Wegener Institute, Helmholtz Centre for Polar and Marine Research (AWI). These  
120 configurations allow us to resolve many essential climate processes directly, for example mesoscale ocean eddies and sea ice  
121 leads in large parts of the mid- and high-latitude ocean, atmospheric storms, as well as certain small-scale features in the  
122 topography and land surface. We also test new developments of the IFS carried out in the last years at ECMWF to improve  
123 the representation of snow cover, land surface, and cities world-wide.

124  
125 This paper documents the coupled km-scale model configurations with the Integrated Forecasting System in Section 2. The  
126 technical and scientific model improvements, carried out along the nextGEMS model development cycles based on feedback  
127 by the nextGEMS community, are presented in Section 3. A first set of emerging advances stemming from the km-scale  
128 character of the simulations is presented in Section 4, and more in-depth process studies will be the focus of dedicated future  
129 work. The paper closes with a summary and discussion of future steps in Section 5.

## 130 **2 Model configurations**

### 131 **2.1 The Integrated Forecasting System and its coupling to NEMO and FESOM**

132 The Integrated Forecasting System (IFS) is a spectral-transform atmospheric model with two-time-level semi-implicit, semi-  
133 Lagrangian time-stepping (Temperton et al., 2001; Hortal, 2002; Diamantakis and Váňa, 2022). It is coupled to other Earth



134 System components (land, waves, ocean, sea-ice), and it is used in its version 48r1 (<https://www.ecmwf.int/en/publications/ifs->  
135 documentation, last access 26 March 2024), which has been used for operational forecasts at ECMWF since July 2023 (plus  
136 modifications that will be detailed in this study). In its operational configuration ('oper'), the atmospheric component is  
137 coupled to the NEMO v3.4 ocean model. A Gaussian octahedral grid (TCo) is used for the atmospheric grid-point calculations  
138 (advection, physical parametrizations, product of terms), which implies higher effective resolution and better efficiency than  
139 other standard (linear) Gaussian grids. It acts as a numerical filter without the need for expensive de-aliasing procedures,  
140 requires little diffusion, and produces small total mass conservation errors for medium-range forecasts (Wedi 2014, Malardel  
141 et al., 2016). A hybrid, pressure-based vertical coordinate is used which is a monotonic function of pressure and depends on  
142 the surface pressure (Simmons and Strüfing, 1983). The vertical coordinate follows the terrain at the lowest level and relaxes  
143 to a pure pressure-level vertical coordinate system in the upper part of the atmosphere. The vertical discretization scheme is a  
144 finite element method using cubic B-spline basis functions (Vivoda et al., 2018, Untch and Hortal, 2004).

145  
146 The atmosphere component of the IFS has a full range of parametrizations described in detail in ECMWF (2023a,b). The moist  
147 convection parameterization, originally described in Tiedtke (1989), is based on the mass-flux approach, and represents deep,  
148 shallow and mid-level convection. For deep convection the mass-flux is determined by removing a modified Convective  
149 Available Potential Energy (CAPE) over a given time scale (Bechtold et al., 2008, 2014), taking into account an additional  
150 dependence on total moisture convergence and a grid resolution dependent scaling factor to reduce the cloud base mass flux  
151 further at grid resolutions higher than 9km (Becker et al., 2021). The sub-grid cloud and precipitation microphysics scheme is  
152 based on Tiedtke (1993) and has since been substantially upgraded with separate prognostic variables for cloud water, cloud  
153 ice, rain, snow and cloud fraction, and an improved parametrization of microphysical processes (Forbes et al. 2011; Forbes  
154 and Ahlgrim, 2014). The parametrization of sub-grid turbulent mixing follows the Eddy-Diffusivity Mass-Flux (EDMF)  
155 framework, with a K-diffusion turbulence closure and a mass-flux component to represent the non-local eddy fluxes in unstable  
156 boundary layers (Siebesma et al., 2007; Kohler et al., 2011). The orographic gravity wave drag is parametrized following Lott  
157 and Miller (1997) and Beljaars et al. (2004) and a non-orographic gravity wave drag parametrization is described in Orr et al.  
158 (2010). The radiation scheme is described in Hogan and Bozzo (2018, ecRad). Full radiation computations are calculated on a  
159 reduced resolution grid every hour with approximate updates for radiation-surface interactions every timestep at full resolution.

160  
161 The land model of the IFS is ECLand (Bousetta et al. 2021), which runs on the identical grid and is fully coupled to the  
162 atmosphere through an implicit flux solver. ECLand represents the surface processes that interact with the atmosphere in the  
163 form of fluxes. The ECLand version used in this work currently contains among others, a 4-layer soil scheme, a lake model,  
164 an urban model, a simple vegetation model, a multi-layer snow scheme, and a vast range of global maps describing the surface  
165 characteristics. A wave model component is provided by ecWAM to account for sea state dependent processes in the IFS  
166 (ECMWF, 2023c). The wave model runs on a reduced lat-lon grid with 0.125° resolution, 36 frequencies, and 36 directions.  
167 This means that the distance between latitudes is 0.125°, and the number of points per latitude is reduced polewards in order



168 to keep the actual distance between grid points roughly equal to the spacing between two consecutive latitudes. The frequency  
169 discretisation is such that ocean waves with periods between 1 and 28 seconds are represented.

170

171 For the purpose of nextGEMS and other related projects such as the DestinE Climate Change Adaptation Digital Twin, where  
172 also an IFS-NEMO configuration with a 1/12 degree ocean (NEMO v4) is applied, the complementary IFS-FESOM model  
173 option was developed. We coupled the Finite Volume Sea ice-Ocean Model FESOM2 (Danilov et al. 2017, Scholz et al. 2019,  
174 Koldunov et al. 2019, Sidorenko et al. 2019) to IFS (see details below). Instead of using a coupler for this task, as for the  
175 OpenIFS-FESOM (Steffing et al. 2022), the alternative adopted here is to follow the strategy for IFS-NEMO coupling, where  
176 the ocean and IFS models are integrated into a single executable and share a common time stepping loop (Mogensen, Keeley,  
177 and Towers, 2012). In this sequential coupling approach (akin to the model physics-dynamics and land-surface coupling that  
178 occurs every model timestep), the atmosphere advances for 1 hour (length of the coupling interval) and fluxes are passed as  
179 upper boundary condition to the ocean, which then in turn advances for 1 hour, up to the same checkpoint. The following  
180 atmospheric step then uses updated surface ocean fields as lower boundary condition for the next coupling interval (Mogensen,  
181 Keeley, and Towers, 2012). Note that there is no need to introduce a lag of one coupling timestep because the ocean and  
182 atmosphere models run sequentially and not overlapping in parallel. A study into the effect of model lag on flux/state  
183 convergence by Marti et al. (2021) found that sequential instead of parallel coupling reduces the error nearly to the fully  
184 converged solution.

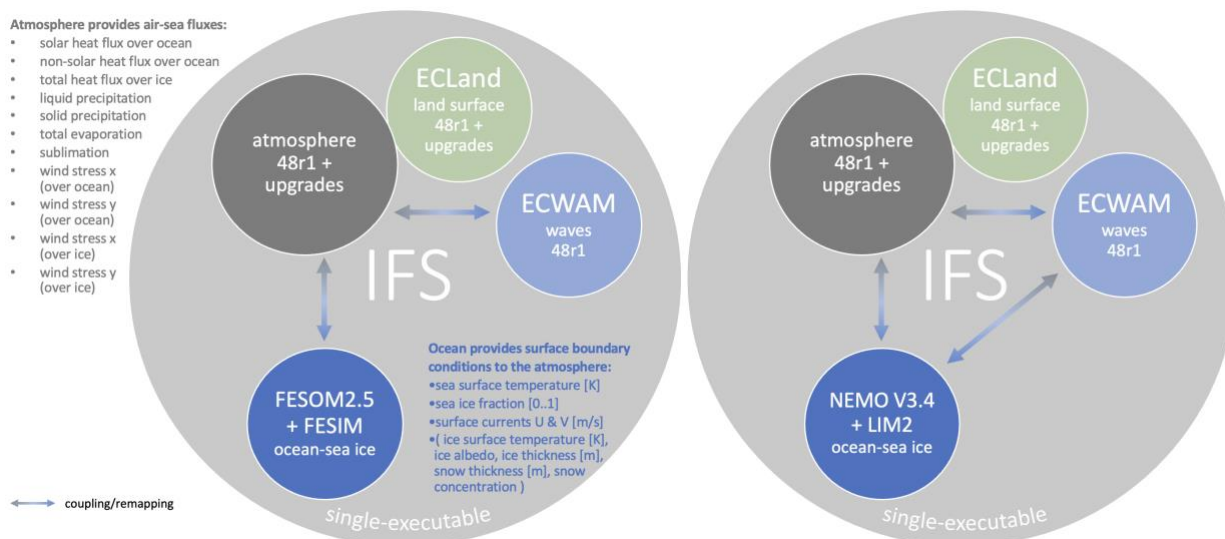
185

186 In the operational IFS, in areas where sea ice is present in the ocean model, currently a sea ice thickness of 1.5m and no snow  
187 cover are assumed for the computation of the conductive heat flux on the atmospheric side. Our initial implementation for the  
188 multi-year simulations carried out in nextGEMS does not divert yet from this assumption of the operational configuration, in  
189 which the atmosphere ‘sees’ only the sea-ice fraction computed by the ocean/sea-ice model. There are more consistent options  
190 available to couple the simulated sea ice albedo, ice surface temperature, ice and snow thickness from the ocean models to the  
191 atmospheric component (Mogensen, Keeley, and Towers, 2012) and those will also be considered in future setups.

192

193 In order to run the IFS on different High Performance Computing (HPC) architectures, we adopted ECMWF’s “RAPS” (Real  
194 Applications on Parallel Systems) benchmark configuration. The RAPS code has been further adopted for use as a running  
195 environment for multi-annual runs. RAPS is a set of mostly shell scripts that allow to build, configure, and submit coupled IFS  
196 experiments on external HPC hardware, other than ECMWF’s on-premise Atos computer in Bologna, Italy. In this  
197 environment, FESOM can be linked as an external ocean library to the IFS. This allows the IFS to control the ocean as a  
198 subroutine and to trigger the ocean initialisation, time-stepping, and finalisation steps (see Section 2.2).





199

200

201

202

203

204

205

206

207

208

209

210

211

212

213

214

215

216

217

218

219

220

221

**Figure 1: Coupling of the Integrated Forecasting System (IFS) components in (left) IFS-FESOM and (right) IFS-NEMO in nextGEMS configurations.** Coupling between the unstructured FESOM grid and the Gaussian grid of the atmosphere is via pre-prepared remapping weights in SCRIP format (Jones 1999). Direct coupling between the surface wave model (ECWAM) and the ocean is at the moment only implemented in IFS-NEMO; in IFS-FESOM, the ocean and waves interact only indirectly via the atmosphere. ECWAM and the atmosphere have their own set of remapping weights for direct coupling, while ECLand and the atmosphere are more closely coupled to each other.

The oceans provide surface boundary conditions to the atmosphere (sea surface temperature, sea ice concentration, zonal and meridional surface currents) while the atmospheric component provides air-sea fluxes to the ocean models (as listed in Fig. 1). The exchange between the different model grids is implemented as a Gaussian distance-weighted interpolation for both directions. Since the implementation accepts any weight files as long as they are provided in SCRIP format (Jones 1999), future setups will explore other interpolation strategies, such as the use of conservative remapping weights for the air-sea fluxes to ensure better flux conservation. River runoff for the ocean models is taken from climatology; for IFS-FESOM, the runoff from the COREv2 (Large and Yeager 2009) flux dataset is applied based on Dai et al. (2009).

In order to couple FESOM with IFS, the existing single-executable coupling interface (i.e. the set of Fortran subroutines) between IFS and NEMO (Mogensen, Keeley, and Towers, 2012) has been extracted and newly implemented directly in the FESOM source code (Rackow et al. 2023c). From the perspective of the atmospheric component, after linking, FESOM and NEMO thus appear to IFS virtually identical in terms of provided fields and functionality in forecast runs with IFS. Clear gaps and differences to the operational configuration with NEMO v3.4 remain in terms of ocean data assimilation capabilities (NEMOVAR), ocean initial condition generation, and missing surface ocean-wave coupling (Fig. 1). However, these differences do not critically impact the multi-year simulations for nextGEMS described in this study or multi-decadal simulations planned for nextGEMS and Destination Earth.



## 222 **2.2 Technical refactoring for the FESOM2.5 ocean-sea ice model code**

223 Prior to the start of nextGEMS, FESOM had been fully MPI-parallelised only and was shown to scale well on processor counts  
224 beyond 100,000 (Koldunov et al. 2019). In the nextGEMS configuration with IFS, which is set up in a single-executable  
225 environment with a hybrid MPI-OpenMP parallelisation approach, experience from Cycle 1 had shown that it had become  
226 necessary to rewrite the ocean model code to fully support hybrid MPI-OpenMP parallelization for the planned multi-year  
227 high-resolution simulations in order for the ocean to make use of the available resources to full extent. In detail, this meant  
228 rewriting numerous non-iterative loops in the ocean model code to support OpenMP parallelisation with release of FESOM  
229 version 2.5.

230 The FESOM model has been significantly refactored also in other aspects over the last years to support coupling with IFS. In  
231 the single executable coupled system, the IFS initializes the MPI communicator (Mogensen, Keeley, and Towers, 2012) and  
232 passes it to the ocean model for initialisation of FESOM. In particular, FESOM's main routine has been split into 3 cleanly  
233 defined steps, namely the initialisation, time stepping, and finalisation steps. This was a necessary step for the current single-  
234 executable coupled model strategy at ECMWF, where the ocean is called and controlled from within the atmospheric model.  
235 The single-executable configuration is a necessary condition for coupled data assimilation at ECMWF. The adopted strategy  
236 means that some IFS-NEMO developments can be directly applied also to IFS-FESOM configurations. Similar to what is done  
237 for the wave and atmosphere components of the IFS, we implemented a fast "memory dump" restart mechanism for FESOM.  
238 This has the advantage that the whole coupled model can be quickly restarted as long as the parallel distribution (number of  
239 MPI tasks and OpenMP processes) does not change during the simulation.

## 241 **2.3 Model output and online diagnostics**

242  
243 One of the concerns for the scientific evaluation of multi-year high-resolution simulations is the need to read large volumes of  
244 output from the global parallel filesystem. This is required for certain processing tasks, such as the computation of monthly  
245 averages in a climate context and regridding to regular meshes, so that the relevant information can be easily analysed and  
246 visualised. One way to mitigate this burden is to move these computations closer to where the data is produced and process  
247 the data in memory. Many of these computations are currently not possible in the IFS code, so we used MultIO (Sármány et  
248 al., 2023), a set of software libraries that provide, among other functionalities, user-programmable processing pipelines that  
249 operate on model output directly. IFS has its own Fortran-based I/O-server that is responsible for aggregating geographically  
250 distributed three-dimensional information and creating layers of horizontal two-dimensional fields. It passes these pre-  
251 aggregated fields directly to MultIO for the on-the-fly computation of temporal means and data regridding.

252  
253 One of the key benefits of this approach is that with the in-memory computation of, for example, monthly statistics, the





254 requirement of storage space may be reduced significantly. Higher-frequency data may only be required for the computation  
255 of these statistics and as such would not need to be written to disk at all. For the nextGEMS runs in this study, however, the  
256 decision was taken to make use of MultiIO for user-convenience mostly, i.e. to produce post-processed output in addition to  
257 the native high-frequency output. The computational overhead associated with this (approximately 15% in this case) is more  
258 than offset by the increased productivity gained from much faster and easier evaluation of high-resolution climate output,  
259 particularly in the context of hackathons with a large number of participants. As a result, the MultiIO pipelines have been  
260 configured to support the following five groups of output:

- 261
- 262 • Hourly or six-hourly output (depending on variable) on native grids.
  - 263 • Hourly or six-hourly output (depending on variable), interpolated to regular (coarser) meshes for ease of data analysis.  
264 The MultiIO configuration uses parts of the functionality of the Meteorological Interpolation and Regridding package  
265 (MIR), ECMWF's open-source re-gridding software, to be able to execute this in memory.
  - 266 • Monthly means for all output variables on native grids.
  - 267 • Monthly means for all output variables on regular (coarser) meshes, interpolated by MultiIO calling MIR.
  - 268 • All fields are encoded or re-encoded in GRIB by MultiIO calling ECCODES, an open-source encoding library.
- 269

270 At the end of each pipeline, all data are streamed to disk, more specifically to the Fields DataBase (FDB, Smart et al., 2017),  
271 an indexed domain-specific object store for archival and retrieval – according to a well-defined schema – of meteorological  
272 and climate data. This mirrors the operational setup at ECMWF. For the nextGEMS hackathons, all simulations and their  
273 GRIB data in the corresponding FDBs have been made available in Jupyter notebooks (Kluyver et al. 2016) via intake catalogs  
274 (<https://intake.readthedocs.io/en/latest/>, last access 25 March 2024) using gribscan. The gribscan tools scans GRIB files and  
275 creates Zarr-compatible indices (Kölling, Klufft, and Rackow, 2024).

## 276 **2.4 Performed nextGEMS runs**

277 The nextGEMS project relies on several model development cycles, in which the high-res models are run and improved based  
278 on community feedback from the analysis of successive runs. In an initial set of km-scale coupled simulations (termed 'Cycle  
279 1'), the models were integrated for 75 days, starting on 20 January 2020 (Table 1). For Cycle 1, ECMWF's IFS has been run  
280 at 9km (TCO1279 in Gaussian octahedral grid notation) and 4.4km (TCO2559) global spatial resolution. The runs at 9km were  
281 performed with the deep convection parametrization, while at 4.4km, the IFS was run with and without the deep convection  
282 parametrization. The underlying ocean models NEMO and FESOM2.1 had been run on an eddy-permitting 0.25° resolution  
283 grid in this initial model cycle (ORCA025 for NEMO and a triangulated version of this for FESOM, tORCA025). Based on  
284 the analysis by project partners during a hackathon organised in Berlin in October 2021, several key issues were identified  
285 both in the runs with IFS, and in those run with ICON (Hohenegger et al. 2023).



286 As will be detailed below, the IFS has been significantly improved for the longer ‘Cycle 2’ simulations (IFS nextGEMS Cycle  
 287 2 4.4km 1-year simulation, <https://dx.doi.org/10.21957/1n36-qg55>; Wieners et al., 2023), where a 2.8km simulation  
 288 (TCo3999) has also been performed. For the purpose of nextGEMS Cycle 2 and 3, an ocean grid with up to 5km resolution  
 289 (‘NG5’) has been introduced for the FESOM model, which is eddy-resolving in most parts of the global ocean (see Appendix  
 290 B). The NG5 ocean has been spun up for a duration of 5 years in stand-alone mode, with ERA5 atmospheric forcing (Hersbach  
 291 et al. 2020) until 20 January 2020. In contrast, NEMO performs active data assimilation to estimate ocean initial conditions  
 292 for 20 January 2020.

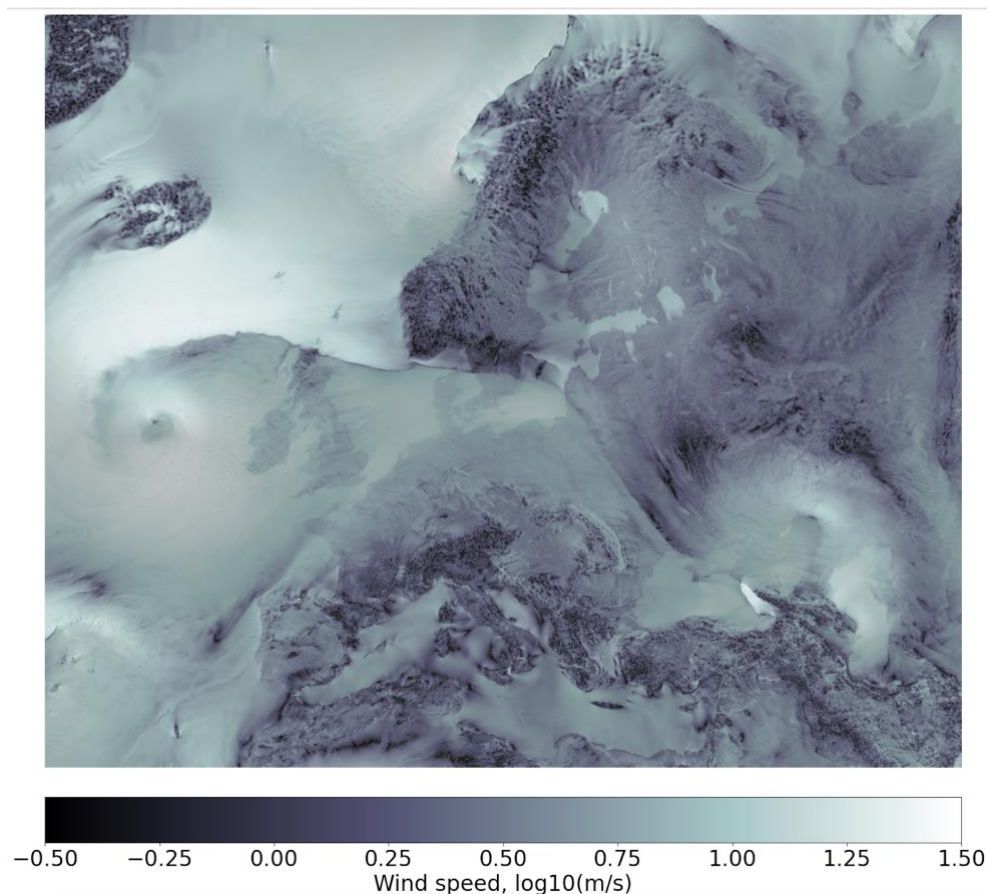
293 Based on feedback from the 2nd hackathon in Vienna in 2022, ‘Cycle 3’ simulations for the recent 3rd hackathon in Madrid  
 294 (June 2023) have been further improved. The ocean has been updated to FESOM2.5 (Rackow et al, 2023c), and run coupled  
 295 for up to 5 years (see Fig. 2 for an example wind speed snapshot at 4.4km resolution). In the following section, we will detail  
 296 the series of scientific improvements in the atmosphere, ocean, and land components of IFS-NEMO/FESOM that were  
 297 performed to address the identified key issues, and how these successive steps result in a better representation of the coupled  
 298 physical system.

299  
 300 **Table 1: nextGEMS configurations of the IFS and coupled simulations analysed in this study.** The Gaussian octahedral grid  
 301 notations TCo1279, TCo2559, and TCo3999 refer to 9km, 4.4km, and 2.8km global atmospheric spatial resolution,  
 302 respectively. The simulations were performed with constant greenhouse gas forcing from the year 2020 (CO<sub>2</sub> = 413.72 ppmv,  
 303 CH<sub>4</sub> = 1914.28 ppbv, N<sub>2</sub>O = 331.80 ppbv, CFC11 = 857.38 pptv, CFC12 = 497.10 pptv), prognostic ozone, no volcanic  
 304 aerosols, and the CAMS aerosol climatology (Bozzo et al. 2020).

Configuration	Length of simulations	Ocean settings
IFS-NEMO, TCo1279 (‘oper’)  Cycle 3, 2, 1	5 years (Cycle 3) 2 years (Cycle 2) 75 days (Cycle 1)	NEMO V3.4, ORCA025 (0.25° 3-polar grid)
IFS-FESOM, TCo1279-NG5  Cycle 3	1 year (Cycle 3)	FESOM2.5, NG5 grid (3-4km in high-res regions; 13km in tropics)
IFS-FESOM, TCo3999-NG5  Cycle 2	8 months (Cycle 2)	FESOM2.1, NG5 grid (3-4km in high-res regions; 13km in tropics)
IFS-FESOM, TCo2559-NG5  Cycle 3 & 2	5 years (Cycle 3) 1 year (Cycle 2)	FESOM2.1/2.5, NG5 grid (3-4km in high- res regions; 13km in tropics)



305



306

307 **Figure 2: Wind speed snapshot over Europe as simulated by IFS with a 4.4km spatial resolution in the atmosphere.**

308 The wind speed map is overlaid with a map of the zonal wind component in a grey-scale colormap for further shading, which

309 is made partly transparent. The figure does not explicitly plot land. The high-resolution simulation nevertheless clearly shows

310 the continental land masses and orographic details due to larger surface friction and hence smaller wind speeds (darker areas

311 depict lower wind speeds). The image is a reproduction with Cycle 3 data of the award winning entry by N. Koldunov for

312 2022's Helmholtz Scientific Imaging Contest [https://helmholtz-imaging.de/about\\_us/overview/index\\_eng.html](https://helmholtz-imaging.de/about_us/overview/index_eng.html)).

### 313 **3 Model developments for multi-year coupled km-scale IFS simulations**

314 This section details model developments for the atmosphere (3.1), ocean and sea ice (3.2), wave (3.3), and land (3.4)

315 components of IFS-NEMO/FESOM in the different cycles of nextGEMS. Following a short overview of identified key issues

316 and developments at the beginning of each section, we present how those successive development steps translate to a better

317 representation of the coupled physical system.



318 **3.1 Atmosphere**

319 **3.1.1 Key issues and model developments**

320 **Water and energy imbalances**

321 At the first nextGEMS hackathon, strong water and energy imbalances were identified as key issues in the Cycle 1 simulations,  
322 which led to large biases in the top-of-atmosphere (TOA) radiation balance. If run for longer than 75 days, e.g. multiple years,  
323 this would lead to a strong drift in global mean 2m temperature. Analysis confirmed that most of the energy imbalance in the  
324 IFS was related to water non-conservation, and that this issue gets worse (i) when spatial resolution is increased, and (ii) when  
325 the parametrization of deep convection is switched off (hereafter ‘Deep Off’). This is because the semi-Lagrangian advection  
326 scheme used in the IFS is not conserving the mass of advected tracers, e.g. the water species (see Appendix A). However,  
327 while this issue was acknowledged to be detrimental for the accuracy of climate integrations, so far it was thought that it was  
328 small enough to not significantly affect the quality of numerical weather forecasts, which span timescales ranging from a few  
329 hours to seasons ahead. To address the problem of water non-conservation in the IFS, a tracer global mass fixer was activated  
330 for all prognostic hydrometeors (cloud liquid, ice, rain and snow) in nextGEMS Cycle 2, as well as water vapour (for more  
331 details, see Appendix A describing the mass-fixer approach). The tracer mass fixer ensures global mass conservation, but it  
332 cannot guarantee local mass conservation. However, it estimates where the mass conservation errors are larger and inserts  
333 larger corrections in such regions, which is often beneficial for local mass conservation and accuracy (see Diamantakis and  
334 Agusti-Panareda, 2017). When adding tracer mass fixers to a simulation, the computational cost increases by a few percentage  
335 points (typically less than 5%). Water and energy conservation in Cycle 1 versus Cycle 2 is discussed in Section 3.1.2.

336 **Top-of-atmosphere radiation balance**

337 To reduce drift in global mean surface temperature, it is essential that the global top-of-atmosphere (TOA) radiation imbalance  
338 is small. In the nextGEMS Cycle 2 simulation at 4.4 km resolution coupled to FESOM2.1 (Table 1), the TOA net imbalance,  
339 relative to observed fluxes from the CERES-EBAF product (Loeb et al. 2018), had been about  $+3 \text{ Wm}^{-2}$  (positive values  
340 indicate downward fluxes), resulting from a  $+5 \text{ Wm}^{-2}$  shortwave imbalance that was partly balanced by a  $-2 \text{ Wm}^{-2}$  longwave  
341 imbalance. Because of anthropogenic greenhouse gas emissions, CERES shows a  $+1 \text{ Wm}^{-2}$  imbalance. Due to the larger TOA  
342 imbalance, the nextGEMS Cycle 2 simulations warmed too much, by about 1K over the course of one year (see Section 3.1.3).  
343 Thus, addressing the TOA radiation imbalance was a major development focus in preparation for the 5-year integration in  
344 nextGEMS Cycle 3.

345 On top of IFS 48r1, in Cycle 3 we used a combination of model changes targeting a reduced TOA radiation imbalance, mostly  
346 affecting cloud amount. Changes that increased the fraction of low clouds are (i) a change restricting the detrainment of mid-  
347 level convection to the liquid phase, (ii) a reduction of cloud edge erosion following Fielding et al. (2020) and (iii) a reduction  
348 of the cloud inhomogeneity, which increases cloud amount as it reduces the rate of accretion. This change is in line with  
349 nextGEMS’s km-scale resolutions as cloud inhomogeneity is expected to be smaller at high resolutions. High clouds were



350 increased in areas with strong deep convective activity by (iv) decreasing a threshold that limits the minimum size of ice  
351 effective radius, in agreement with observational evidence and (v) changing from cubic to linear interpolation for the departure  
352 point interpolation of the Semi-Lagrangian advection scheme for all moist species except water vapour. The resulting TOA  
353 balance in Cycle 3 is discussed in Section 3.1.3.

### 354 **Representation of intense precipitation and convective cells**

355 Precipitation has many important roles in the climate system. It is not only important for the water cycle over land and ocean,  
356 but also provides a source of energy to the atmosphere, as heat is released when water vapour condensates and rain forms,  
357 which balances radiative cooling. Precipitation is also often associated with meso-scale or large-scale vertical motion and the  
358 corresponding overturning circulation is crucial for the horizontal and vertical redistribution of moisture and energy within the  
359 atmosphere.

360 In km-scale simulations in which the deep convection parametrization is switched off (e.g, Cycle 2 at 4.4 km and 2.8 km  
361 resolution), convective cells tend to be too localised, too intense, and they lack organisation into larger convective systems  
362 (e.g, Crook et al., 2017, Becker et al., 2021). The characteristics of meso-scale organisation of convection also affect the larger  
363 scales, for instance zonal mean precipitation and the associated large-scale circulation. For example, with deep convection  
364 parametrization off in Cycle 2 (Deep Off), the ITCZ often organises into a continuous and persistent line of deep convection  
365 over the Pacific at 5°N (see Fig. D1 in Appendix D), and the zonal mean precipitation at 5°N is strongly overestimated.

366 To address these issues, instead of switching the deep convection scheme off completely, we have reduced its activity by  
367 reducing the cloud-base mass flux in Cycle 3. The cloud-base mass flux is the key ingredient of the convective closure, and  
368 depends on the convective adjustment time scale  $\tau$ , which assures a transition to resolved convection at high resolution via an  
369 empirical scaling function that depends on the grid spacing (discussed in more detail in Becker et al., 2021). To significantly  
370 reduce the activity of the deep convection scheme in Cycle 3, we use the value of the empirical scaling function that is by  
371 default used at 700m resolution (TCo15999) already at 4.4 km resolution (TCo2559), which corresponds to a reduction of the  
372 empirical value that determines the cloud base mass flux by a factor of 6 compared to its value at 9 km resolution. Precipitation  
373 characteristics in Cycle 3 vs Cycle 2 are discussed in Section 3.1.4.

374

### 375 **3.1.2 Improvements of mass and energy conservation in Cycle 2 vs Cycle 1**

376 To address the water non-conservation mentioned in Section 3.1.1, tracer mass fixers for all moist species were introduced in  
377 Cycle 2. Figure 3 shows that the Cycle 1 simulations with the IFS have an artificial source of water in the atmosphere. This  
378 artificial source is responsible for 4.6% of total precipitation in the 9 km simulation with deep convection parametrization  
379 switched on (hereafter ‘Deep On’), which is also used for ECMWF’s operational high-resolution ten-day forecasts, and for  
380 10.7% at 4.4 km with Deep Off. Further analysis after the hackathon by the modelling teams at ECMWF has shown that about  
381 50% of the artificial atmospheric water source is created as water vapour. The additional water vapour not only affects the



382 radiation energy budget of the atmosphere, but it can also cause energy non-conservation when heat is released through  
 383 condensation. The other 50% of water is created as cloud liquid, cloud ice, rain or snow. This is related to the higher-order  
 384 interpolation in the semi-Lagrangian advection scheme introduced for cloud liquid, cloud ice, rain and snow in IFS Cycle 47r3,  
 385 which can result in spurious maxima and minima, including negative values, which are then clipped to remain physical. It  
 386 turns out that the spurious minima are in excess of the spurious maxima and by clipping them, the mass of cloud liquid, cloud  
 387 ice, rain and snow is effectively increased. When activating global tracer mass fixers, global water non-conservation is  
 388 essentially eliminated (about 0.1%) in the Cycle 2 simulations (Figure 3).

389  
 390 On a global scale, the total energy budget of the atmosphere can be defined as

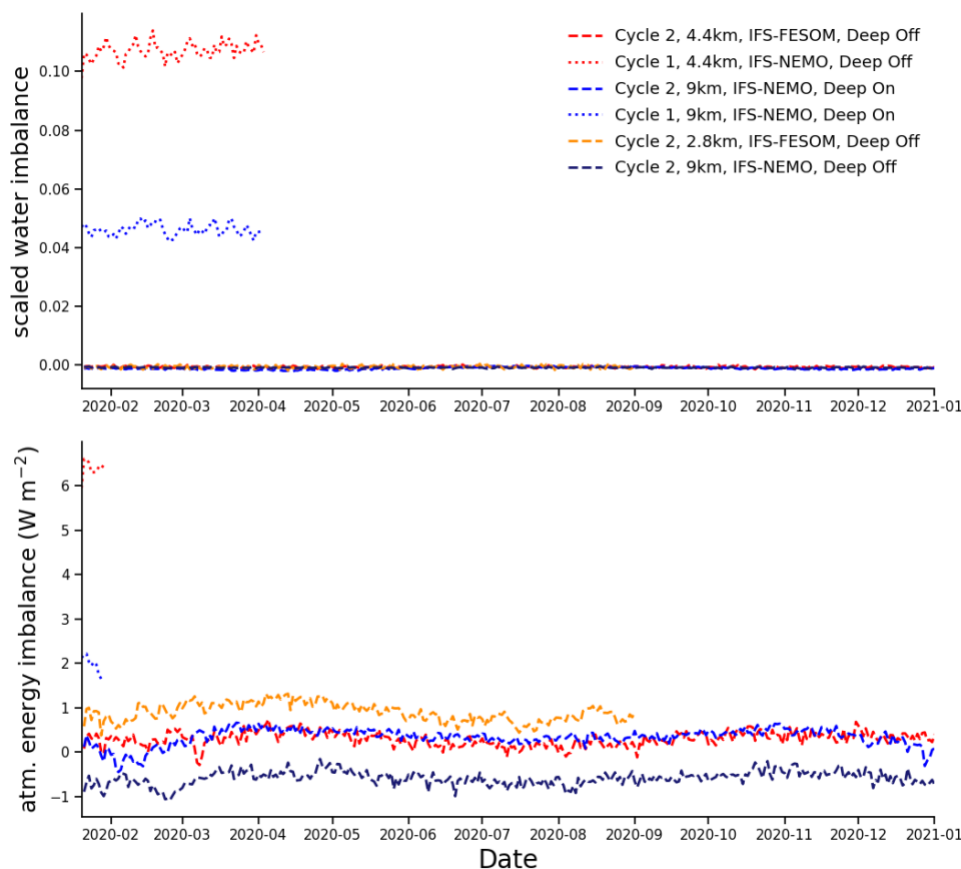
$$\begin{aligned}
 & \frac{c_{pd}}{g} \int_{p_{surf}}^0 \frac{dT}{dt} dp_h + \frac{L_{v0}}{g} \int_{p_{surf}}^0 \frac{dq_v}{dt} dp_h - \frac{L_{s0} - L_{v0}}{g} \int_{p_{surf}}^0 \frac{dq_i + dq_s}{dt} dp_h + \int_{p_{surf}}^0 \frac{dKE}{dt} dp_h \\
 & = F_s + F_q - F_{rad}^{top} + F_{rad}^{surf} + (L_{s0} - L_{v0})P_s,
 \end{aligned}$$

391  
 392  
 393  
 394 where  $T$  is temperature,  $q_v$ ,  $q_l$  and  $q_i$  are water vapour, cloud ice and snow. Together, these terms describe the change in  
 395 vertically-integrated frozen moist static energy over time, while the last term on the left-hand-side of the equation is the change  
 396 in vertically-integrated kinetic energy ( $KE$ ). Sources and sinks of the atmosphere's total energy are  $F_s$  and  $F_q$ , which are the  
 397 surface turbulent sensible and latent heat fluxes,  $F_{rad}^{top}$  and  $F_{rad}^{surf}$ , which are the TOA and surface net radiative shortwave and  
 398 longwave fluxes, and  $(L_{s0}-L_{v0})P_s$  is the energy required to melt snow at the surface. Note that dissipation is not a source or sink  
 399 of total energy.

400  
 401 Using this equation to calculate the global energy budget imbalance in Figure 3, the Cycle 1 simulation with 9 km resolution  
 402 has an atmospheric energy imbalance of  $2.0 \text{ Wm}^{-2}$ , and this imbalance increased to  $6.4 \text{ Wm}^{-2}$  at 4.4 km resolution with Deep  
 403 Off. In Cycle 2, the energy budget imbalance due to the mass conservation of water species is substantially smaller, having  
 404 reduced to less than  $1 \text{ Wm}^{-2}$ . This remaining imbalance can be related to the explicit and semi-implicit dynamics because they  
 405 are still non-conserving, for example causing an error in surface pressure, as well as the mass fixers. The remaining imbalance  
 406 could be removed by adding a total energy fixer to the model. The discussed setup with improved water and energy  
 407 conservation is part of ECMWF's recent operational IFS upgrade in June 2023 (48r1) because it improves the skill scores of  
 408 the operational weather forecasts (ECMWF Newsletter 172, 2022).

409





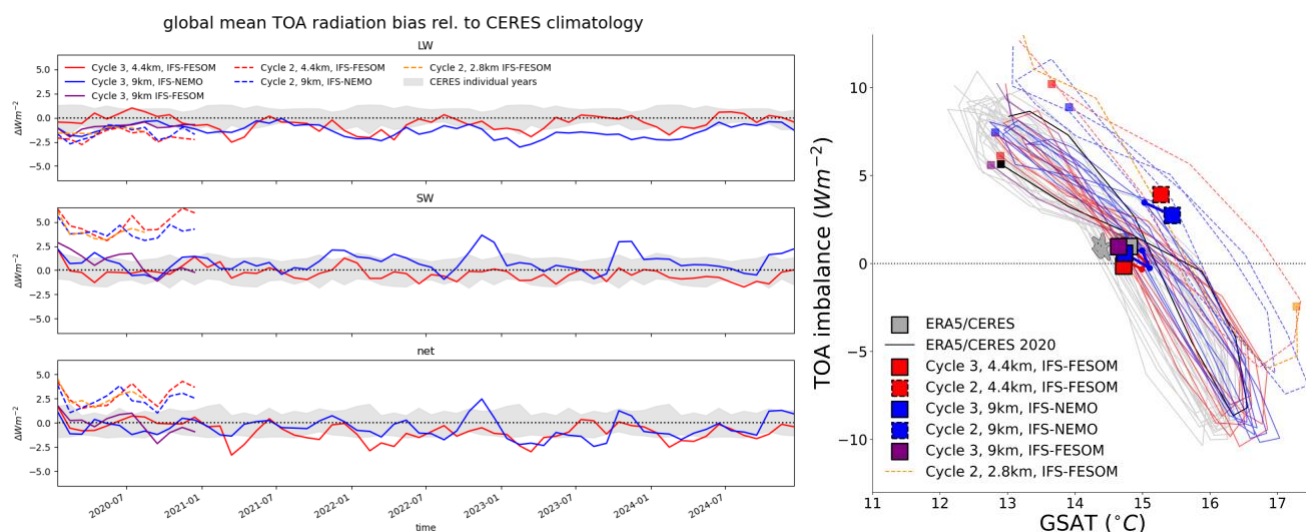
410

411 **Figure 3: Daily mean water non-conservation (left) and daily-mean atmospheric energy imbalance (right), as a function**  
 412 **of lead time for Cycle 1 and Cycle 2 simulations.** Water non-conservation is computed as the daily change in globally  
 413 integrated total water, taking account of surface evaporation and precipitation, as a fraction of the daily precipitation. The  
 414 atmospheric energy imbalance is calculated with Equation 1.

415

416 **3.1.3 Realistic TOA radiation balance and surface temperature evolution in Cycle 3**

417 Due to the model changes detailed in Section 3.1.1, the nextGEMS Cycle 3 simulations with the IFS have at all resolutions a  
 418 TOA radiation imbalance that is within observational uncertainty, with respect to the net, shortwave and longwave fluxes  
 419 (Figure 4). This is not only true for the annual mean value, but also for the annual cycle of TOA imbalance (8-shape in Figure  
 420 4).



421

422 **Figure 4: Global-mean TOA radiation deviation from the CERES climatology in the 5-year-long nextGEMS**

423 **simulations and global-mean TOA imbalance as function of global-mean surface air temperature (GSAT).** a) Grey

424 shading shows the climatological range of individual CERES years. Due to the free-running nature of the nextGEMS

425 simulations, variations within the grey envelope are to be expected even in the absence of any bias. b) Grey lines show the

426 climatological range of individual CERES years (2001–2020) over ERA5 GSAT data (Hersbach et al. 2020). Thin lines are

427 tracing monthly mean values with a small square marking the final month for each simulation. Big squares depict annual means

428 (dashed for Cycle 2, solid for Cycle 3) and for multi-year simulations thick solid lines are tracing annual means for each year

429 with the big square marking the last simulated annual mean.

430

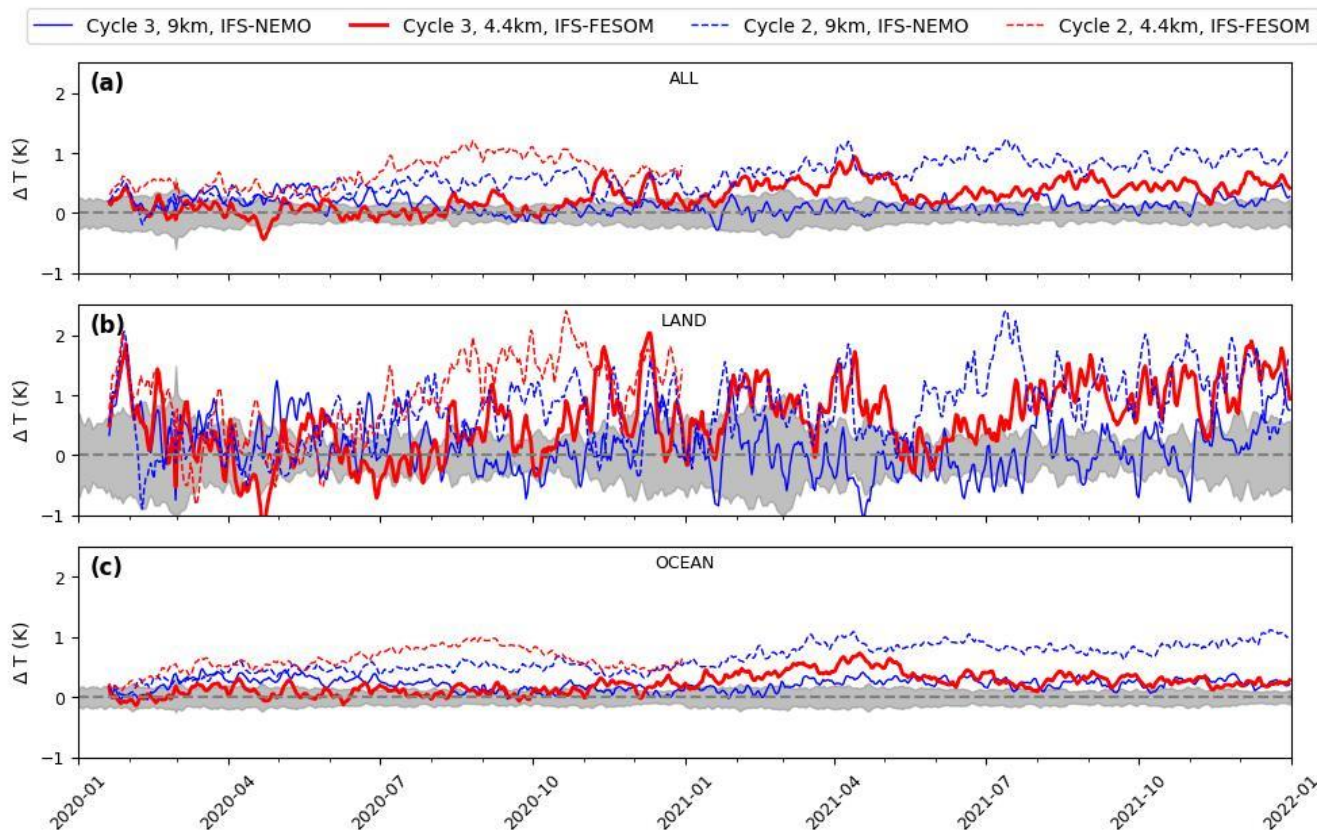
431 As a result, the global mean surface temperature in the Cycle 3 simulations is in close agreement with the ERA5 reanalysis

432 (Hersbach et al. 2020), and stays in close agreement over the 5 years of coupled simulations (Figure 5 and Figure C1 in

433 Appendix C).

434 Going from Cycle 2 to Cycle 3, the warming over time is not evident anymore in IFS-FESOM and IFS-NEMO (Figure 5).

435 Differences in local warming over the Southern Ocean in the two models are further discussed in section 3.2.2.



436

437

**Figure 5: Timeseries of 2-metre temperature global (a), only over land (b) and only over ocean (c) with respect to ERA5, for the years 2020-2021.** The shaded area shows the ERA5 standard deviation between 2012-2021. The evolution of the 2-metre temperature over 5 years is shown in Figure C1 in Appendix C.

438

439

440

441

### 3.1.4 Improved precipitation characteristics in Cycle 3 vs Cycle 2 and larger-scale impacts

442

Snapshots of cloudy brightness temperature and precipitation over the Indian Ocean (Fig. 6) illustrate that after 12 days of simulation in Cycle 3, there are biases in the characteristics of precipitating deep convection compared to satellite observations, even after the developments for Cycle 3 (see Section 3.1.1) were introduced. The observations show multiple mesoscale convective systems (MCS), which are associated with strong precipitation intensities and large anvil clouds. Neither the baseline 9 km Cycle 3 simulation nor the 4.4 km simulation manage to represent the MCS as observed. At 9 km, the convective cells are not well defined with wide-spread areas of weak precipitation. Indeed, precipitation intensity is underestimated in this setup, with precipitation intensity rarely exceeding 10 mm/hour (Fig. 7a). Instead of organising into MCS, hints of spurious gravity waves initiated from parametrized convective cells can be seen in the precipitation snapshot, emanating in different directions.

443

444

445

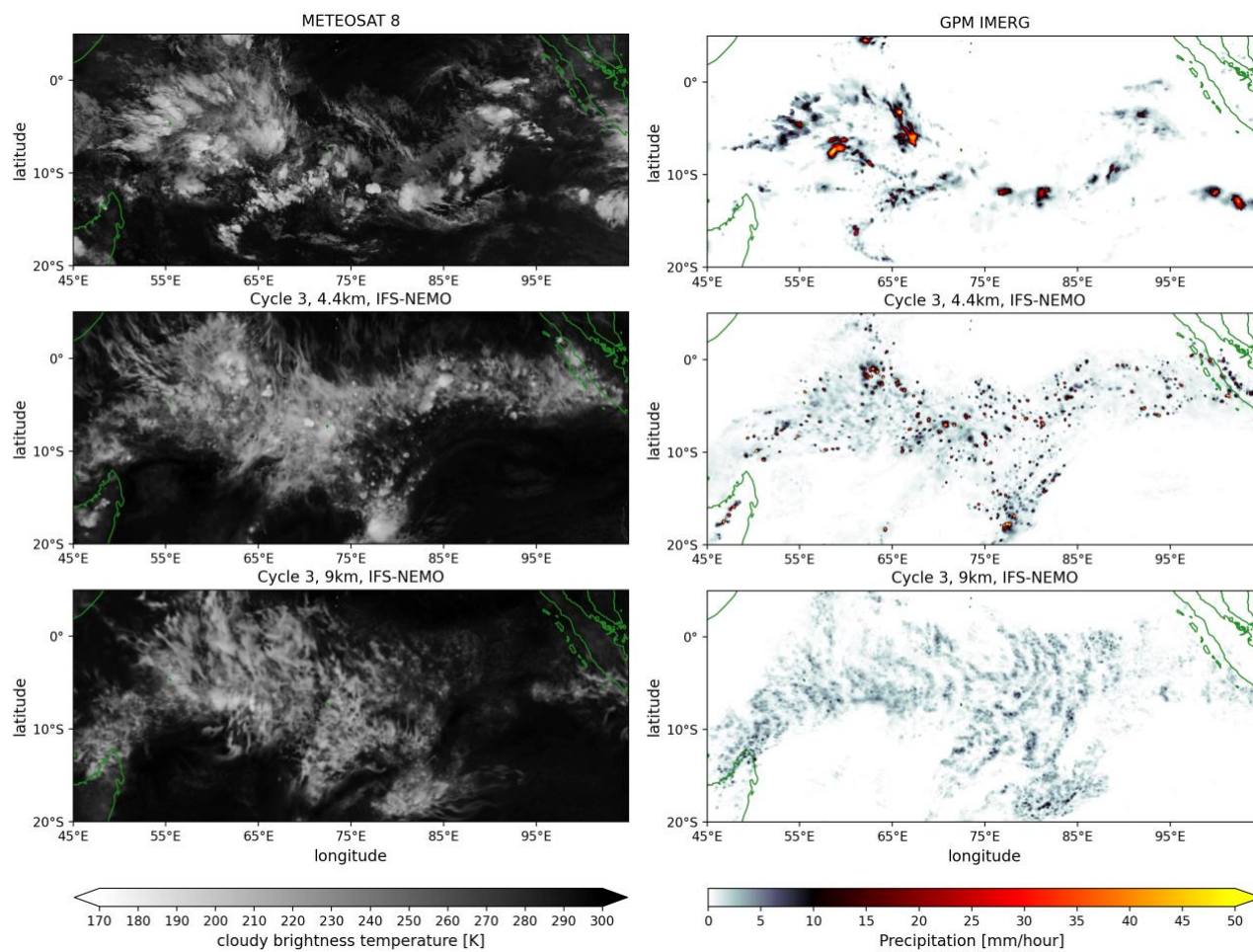
446

447

448

449

450



451

452 **Figure 6: Snapshot for 31/01/2020 at 21:00 UTC of infra-red brightness temperature (left) and hourly precipitation rate**  
 453 **(right) over the Indian Ocean**, from observations (Meteosat 8 SEVIRI channel 9 and GPM IMERG, 1st row), and at forecast  
 454 day 12 of IFS-NEMO 4.4 km (2nd row) and 9 km (3rd row) simulations. The simulations use the nextGEMS Cycle 3 setup  
 455 except that they are run with a satellite image simulator and are coupled to NEMO V3.4 (ORCA025).

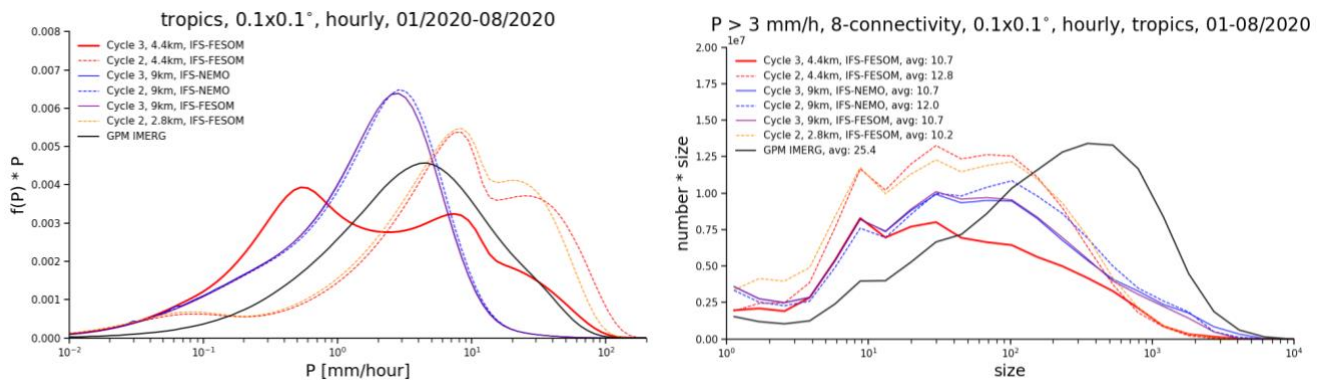
456

457 However, at 4.4 km resolution, the deep convection scheme is much less active, as the cloud base mass flux has been reduced  
 458 by a factor of 6 compared to its value at 9 km (see Section 3.1.1). This setup features more realistic precipitation intensities,  
 459 and particularly the strong precipitation of more than 10 mm/hour is close to the satellite retrieval GPM IMERG (Figure 7a),  
 460 while the Cycle 2 simulations with Deep Off overestimate and with Deep On underestimate intense precipitation. In contrast,  
 461 weak precipitation of 0.1 to 1 mm/hour is most strongly overestimated at 4.4 km resolution in Cycle 3. This is mostly  
 462 precipitation that stems from the weakly active convection scheme. Solutions of how to reduce this drizzle bias are being  
 463 worked on, e.g., through an increase of the rain evaporation rate.





464 A related issue is that the size of convective cells is too small, as illustrated by the size distribution of connected grid cells with  
 465 precipitation exceeding 3 mm/hour (Fig. 7b). The average size of a precipitation cell is rather similar in all simulations, and  
 466 only about half the value as in GPM IMERG. While GPM IMERG has a substantial number of precipitation cells that exceed  
 467 a size of  $10^3$  grid points, which for example would correspond to a precipitation object of  $5^\circ \times 2^\circ$ , this size is almost never  
 468 reached in the IFS simulations. The baseline simulations reach this size more often than the higher-resolution simulations, but  
 469 mainly in association with the spurious gravity waves, not because an MCS would be correctly represented. In summary, the  
 470 representation of intense precipitation has been improved from Cycle 2 to Cycle 3, but that has not led to more realistic  
 471 precipitation cell sizes. Even though it is possible that GPM IMERG overestimates precipitation cell size, cloudy brightness  
 472 temperature shows the same issue (Fig. 6). Work with other models (e.g., ICON, NICAM, SCREAM) has also shown that an  
 473 underestimation of precipitation cell size is a common issue in global km-scale resolution simulations, in some models even  
 474 leading to “popcorn” convection, and will require more attention in the future.  
 475



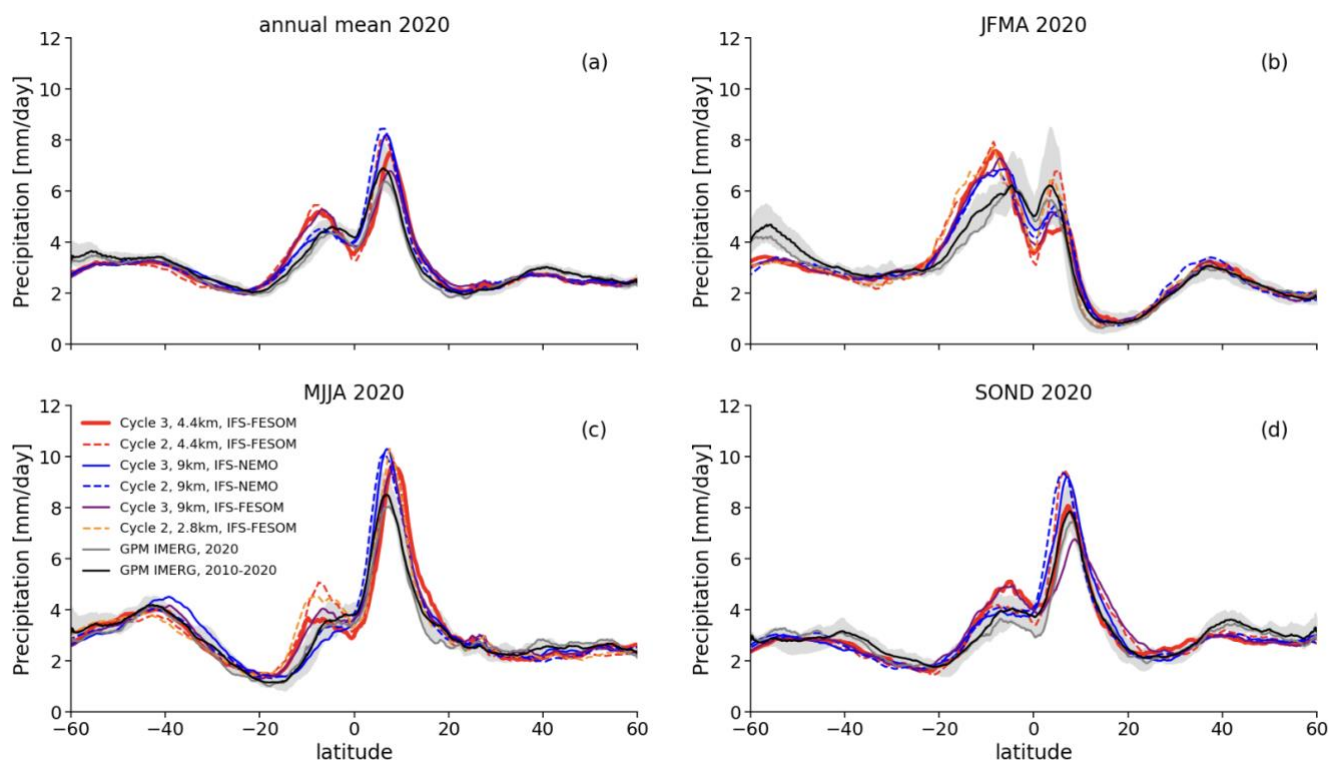
476  
 477 **Figure 7: (a) Frequency times bin intensity of hourly precipitation intensity in the tropics (30S-30N), conservatively**  
 478 **interpolated to a 0.1° grid from January to August 2020.** Following Berthou et al. (2019), the bins are exponential, meaning  
 479 that the area under the curve represents the contribution of that intensity range to the mean. (b) Histogram of precipitation cell  
 480 size times bin size, using a similar approach as in (a). The precipitation cell size is defined as the number of connected grid  
 481 cells on a 0.1° grid (also considering diagonal neighbours) where precipitation exceeds 3 mm/hour, counting cells in the whole  
 482 tropics (30°S-30°N), again from January to August 2020. The average precipitation cell size is given in the legend. The  
 483 observational estimate is from GPM IMERG.

484  
 485 As already mentioned in Section 3.1.1, the characteristics of meso-scale organisation of convection also affect the larger scales.  
 486 For example, in Cycle 2 simulations with Deep Off, the ITCZ often organises into a continuous and persistent line of deep  
 487 convection over the Pacific at  $5^\circ\text{N}$  (see Figure D1 in Appendix D) and as a consequence, the zonal mean precipitation is  
 488 strongly overestimated. This bias improved significantly from Cycle 2 to Cycle 3, when switching from a setup with no deep  
 489 convection scheme in Cycle 2 (at 2.8 and 4.4km resolution) to a setup with reduced cloud base mass flux in Cycle 3 (at 4.4km).



490 While the peak of precipitation around 5°N was overestimated by a factor of 2 during individual winter months in the 2.8 and  
 491 4.4km Cycle 2 run (see Figure D2 in Appendix D), the 4.4km Cycle 3 run shows a much reduced bias, and the peak at 5°N is  
 492 thus perfectly aligned with the GPM IMERG observations during September-December (Figure 8d). The 9 km baseline run  
 493 did not change significantly from Cycle 2 to Cycle 3 but it also shows some small improvements with regards to the  
 494 overestimation of the precipitation peak at 5°N.

495 Comparing the FESOM and NEMO runs, it is striking that all FESOM runs overestimate precipitation in the Southern  
 496 Hemisphere tropics around 10°S, hinting at a biased large-scale circulation, while NEMO runs show some good agreement  
 497 with observations. The different seasons (Figure 8b-d) show an overestimation of precipitation at 10°S only during January-  
 498 April in the NEMO runs, while FESOM runs overestimate precipitation at 10°S during most of the year. Additionally, the  
 499 FESOM runs also slightly underestimate precipitation at the equator (particularly during January-April), hinting at a double  
 500 ITCZ bias, which is a common issue in coupled simulations at km-scale resolutions during boreal winter, e.g. in ICON  
 501 (Hohenegger et al., 2023). Compared to ICON and other global coupled km-scale models that contributed to the DYAMOND  
 502 model intercomparison project (Stevens et al., 2019), the zonal mean precipitation biases in IFS nextGEMS Cycle 3 are of  
 503 similar nature and in part smaller than in the other models.



504  
 505 **Figure 8: Zonal-mean precipitation in nextGEMS Cycle 2 and 3, averaged over the year 2020 (a) and for different 4-**  
 506 **months periods in 2020, January-April (b), May-August (c) and September-December (d). Observations are from GPM**

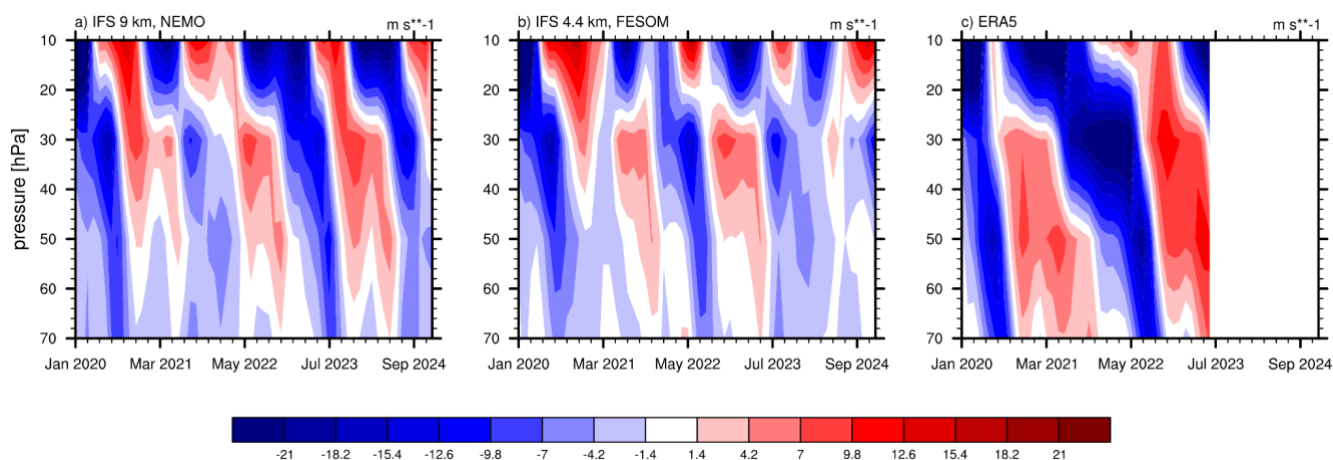




507 IMERG for the year 2020 and for the 2010-2020 climatological period, indicating the climatological range of individual years  
508 via the grey shading.

509

### 510 3.1.5 Stratospheric Quasi-Biennial Oscillation



511

512 **Figure 9: Time evolution of monthly-mean zonal winds, averaged over the equatorial band 10S-10N, for a) the IFS 9 km**  
513 **Cycle 3 simulation with NEMO, b) the IFS 4.4 km Cycle 3 simulation with FESOM, and c) the ERA5 reanalysis for reference.**

514 The Quasi-Biennial Oscillation (QBO) in the equatorial stratospheric winds is driven by momentum deposited by breaking  
515 small-scale convectively generated gravity waves (GWs) and large-scale Kelvin and Rossby-gravity waves (e.g., Baldwin et  
516 al., 2001). The QBO can have a downward influence on the troposphere (e.g., Scaife et al., 2022) and it is thus important to  
517 simulate it well in seasonal and decadal prediction models. As km-scale models explicitly resolve GWs to a large extent, they  
518 have a potential to better simulate the QBO than lower resolution models (e.g., CMIP), which fully rely on GW  
519 parametrizations. However, GW parametrizations are often tuned to get a good QBO in lower resolution models (Garfinkel et  
520 al., 2022; Stockdale et al., 2022) and at higher resolution the resolved GW forcing can be overestimated with less freedom for  
521 tuning. For example, whether parametrized deep convection is switched on or off has a large impact on resolved GWs, with  
522 fully resolved convection generating more than two times stronger GW forcing (Stephan et al., 2019; Polichtchouk et al., 2021)  
523 and a QBO period that is – as a result – too fast.

524 We find that the QBO is reasonably well simulated in the nextGEMS Cycle 3 simulations at 9 km and even at km-scale (4.4  
525 km) resolution (Fig. 9). The periodicity is reasonable, peaking at around 20 months at 30hPa for both simulations (calculated  
526 by performing FFT on the monthly timeseries). This can be probably further improved by tuning the strength of parametrized  
527 non-orographic GW drag, which is still on with reduced magnitude in both 9km and 4.4km simulations, reduced to 70% and  
528 35%, respectively, compared to that at 28 km resolution.



529 In the lower stratosphere below 40hPa, the amplitude of the QBO, however, is underestimated (compare panels a-b) to panel  
530 c) in Fig. 9), especially for the eastward phase. This deficiency is also observed in many lower-resolution models (Bushell et  
531 al., 2022). We hypothesise that the overall reasonable QBO simulation at km-scale resolution might partly be due to the  
532 parametrization for deep convection being still “slightly on” in the Cycle 3 simulations with IFS, as detailed in the previous  
533 section.

## 534 **3.2 Ocean, Sea ice, and Waves**

### 535 **3.2.1 Key issues and model developments**

536 From a model development point of view, one of the main purposes of the nextGEMS Cycle 3 simulations was to set up and  
537 test a fully-coupled global model that runs over multiple years and still does not show drift in global mean surface temperature  
538 and other main climate characteristics, prior to performing the final multi-decadal integrations foreseen in nextGEMS. To  
539 reduce drift (Figure 5), in particular over the Southern Ocean where the model in Cycle 2 had shown a strong warming over  
540 the ocean with time compared to the ERA5 range for 2020-2021, the FESOM ocean component has been updated to the latest  
541 release version 2.5 and coupling between the ocean and atmosphere has been improved.

#### 542 **Warm biases over the ocean**

543 The warming ocean in Cycle 2 leads to an overall warming of the atmosphere as well. The 4.4km IFS-FESOM simulations in  
544 Cycle 2 with 5km resolution in the ocean had shown a warming over the Southern Ocean in winter and year-round in the  
545 tropics. For Cycle 3, the latter has been significantly improved by tuning the TOA balance and by using partially active  
546 parametrized convection, while the former has been solved by a combination of different factors, namely (i) improvements in  
547 the consistency of the heat flux treatment between the atmosphere and ocean/sea ice component, (ii) heat is taken from the  
548 ocean in order to melt snow falling into the ocean, which had been overlooked before, (iii) the activation of a climatological  
549 runoff/meltwater flux around Antarctica (COREv2, Large and Yeager 2009), and (iv) a general update from FESOM2.1 to  
550 FESOM2.5 (Rackow et al. 2023c, <https://github.com/FESOM/fesom2/releases/tag/2.5/>). The resulting more realistic  
551 temperature evolution in Cycle 3 is discussed in Section 3.2.2.

#### 552 **Sea ice performance**

553 In Cycle 1 and 2, the sea ice representation in IFS-FESOM showed prominent deviations from the observed seasonal cycle in  
554 the Ocean and Sea Ice Satellite Application Facility (OSI-SAF) dataset. This could be addressed mainly by correcting the  
555 shortwave flux over ice with the release of FESOM version 2.5. The resulting sea ice performance in Cycle 3 is discussed in  
556 Section 3.2.3.

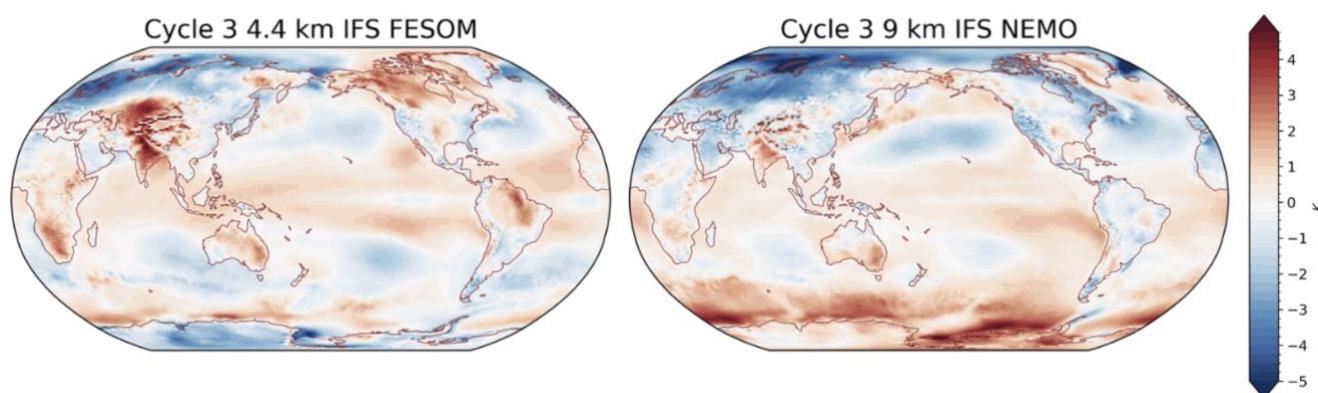
557



### 558 3.2.2 Improved Southern Ocean temperature evolution

559 As already mentioned in section 3.1.3, IFS-FESOM simulations in Cycle 2 (TCo2559 and NG5 grid in the ocean) had shown  
560 a warming over the Southern Ocean in winter and year-round in the tropics. For Cycle 3, the improvement in IFS-FESOM  
561 4.4km is particularly evident when comparing to the operational 9km IFS setup with NEMO V3.4. While the Southern Ocean  
562 shows a similar magnitude of anomalies in IFS-FESOM TCo2559-NG5 in year 5 compared to the first year, there appears to  
563 be an increase of anomalies over time in IFS-NEMO (Figure 10). This has been confirmed in a second set of IFS-FESOM  
564 simulations at TCo399 resolution (28km), and on the tORCA025 ocean grid (not shown).

565



566

567 **Figure 10: Anomaly of annual-mean 2m temperature in year 5 of the nextGEMS Cycle 3 simulations, initialised on 20**  
568 **January 2020, compared to the mean of ERA5 over 2020-2021.** (left) IFS-FESOM 4.4km/NG5, and (right) IFS-NEMO  
569 9km/ORCA025.

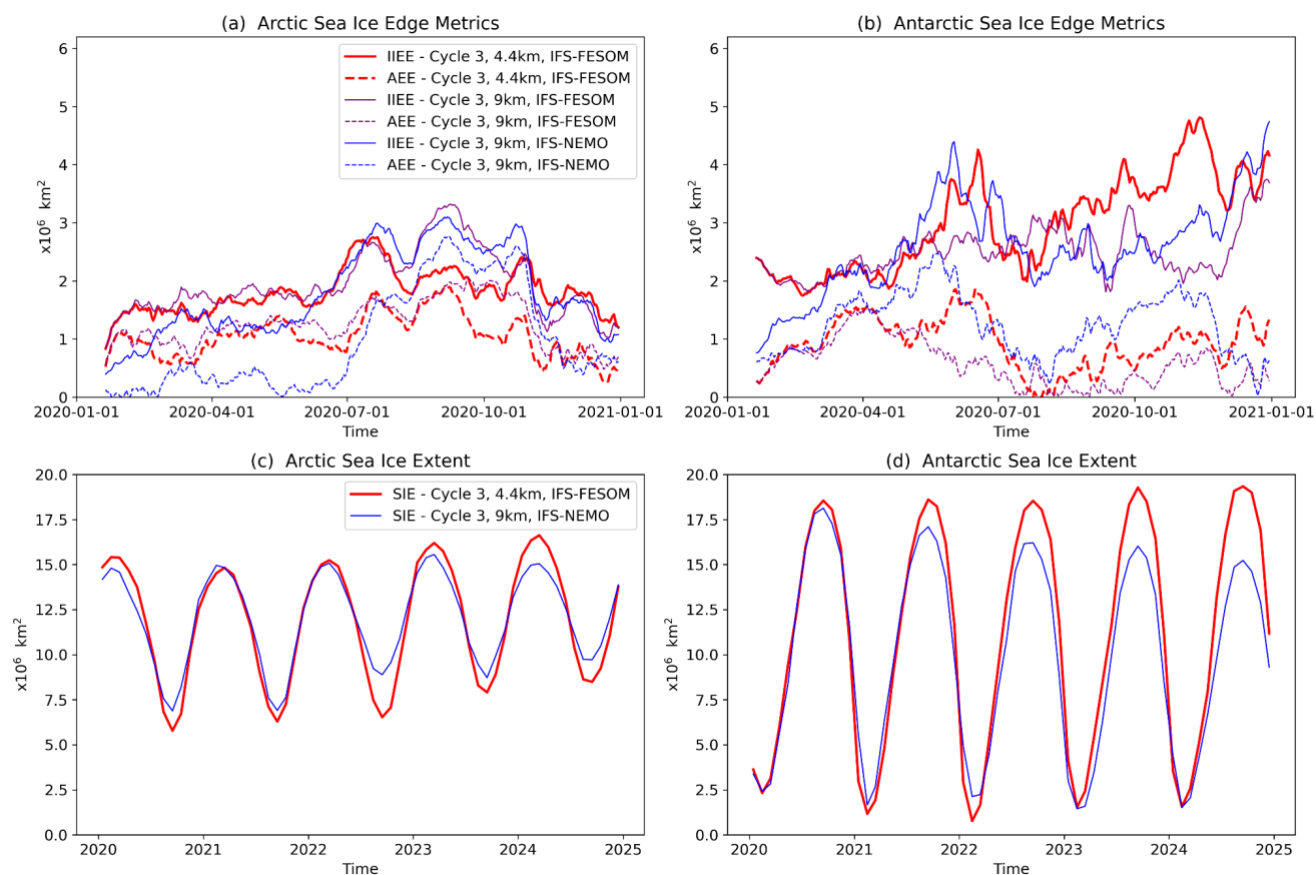
570

### 571 3.2.3 Integrated sea ice performance metrics

572 The performance of the nextGEMS Cycle 3 simulations is analysed in terms of the sea ice extent and sea ice edge position  
573 (Fig. 11). The Integrated Ice Edge Error (IIEE), the Absolute Extent Error (AEE), and the Sea Ice Extent (SIE) metrics are  
574 used for comparing the model simulations and daily 2020 remote-sensing sea ice concentration observations from the Ocean  
575 and Sea Ice Satellite Application Facility (OSI SAF). Specifically, the recently released Global Sea Ice Concentration climate  
576 data record (SMMR/SSMI/SSMIS), release 3 (OSI-450-a; OSI SAF 2022) is considered in our analysis. The IIEE is a  
577 positively defined metric introduced by Goessling et al. (2016), and it is commonly used for evaluating the correctness of the  
578 sea ice edge position in Arctic and Antarctic sea ice predictions (Zampieri et al. 2018, Zampieri et al. 2019). We compute the  
579 IIEE by summing the areas where the model overestimates and underestimates the observed sea ice edge, here defined by the  
580 15% sea ice concentration contour. The SIE is the hemispherically integrated area where the sea ice concentration is larger



581 than 15%. Finally, the AEE represents the absolute difference in the hemispheric SIE of models and observations, therefore  
 582 not accounting for errors arising from a different distribution of the ice edge in the two sets.  
 583



584  
 585 **Figure 11: (a) Arctic daily Integrated Ice Edge Error (IIEE; solid lines) and Absolute Extent Error (AEE; dashed lines)**  
 586 **for three different Cycle 3 simulations. (b) is the same as (a), but for Antarctic sea ice.** The IIEE and AEE metrics are  
 587 computed by comparing the three model runs against remote-sensing sea ice concentration observations from OSI-SAF. (c)  
 588 and (d) show the Arctic and Antarctic sea ice extent for two different Cycle 3 simulations from 2020 until the end of 2024.  
 589

590 All model configurations show substantial errors in representing the initial state. In the Arctic, the error grows in the first  
 591 simulation days in response to the active coupling between the sea ice components and the IFS atmospheric model (Fig. 11a).  
 592 In the Antarctic, an initial error growth takes place for the IFS-NEMO model configuration, while modest error mitigation is  
 593 seen for the two IFS-FESOM configurations (Fig. 11b). The latter feature suggests that a coupled setup could be better suited  
 594 to represent the Antarctic sea ice processes in the FESOM models, at least for this specific instance. Both in the Arctic and  
 595 Antarctic, the initial error of the IFS-NEMO configuration is substantially lower than that of the IFS-FESOM configurations.



596 This behaviour is expected since NEMO performs active data assimilation, while the sea ice in FESOM is only constrained by  
597 the ERA5 atmospheric forcing (Hersbach et al. 2020) imposed during the ocean-sea ice model spinup. In the Antarctic, the  
598 initial error differences diminish quickly and, after a couple of months, the errors of IFS-NEMO and IFS-FESOM are similar.  
599 In the Arctic, IFS-NEMO exhibits residual prediction skill over IFS-FESOM in late spring, four to six months after the  
600 initialization, possibly due to a more accurate description of the Arctic Ocean heat content influenced by the use of proper  
601 ocean data assimilation techniques. After the initialization, the pan-hemispheric sea ice model performance is similar for the  
602 three configurations, and attributing the error differences to the use of different model resolution or complexity is not obvious,  
603 confirming previous findings (e.g., Streffing et al. 2022; Selivanova et al., 2023). Overall, the model errors for the first year of  
604 simulations are in line with state-of-the-art seasonal prediction systems (Johnson et al. 2019; Mu et al. 2020; Mu et al. 2022),  
605 showing similar features in terms of seasonal error growth.

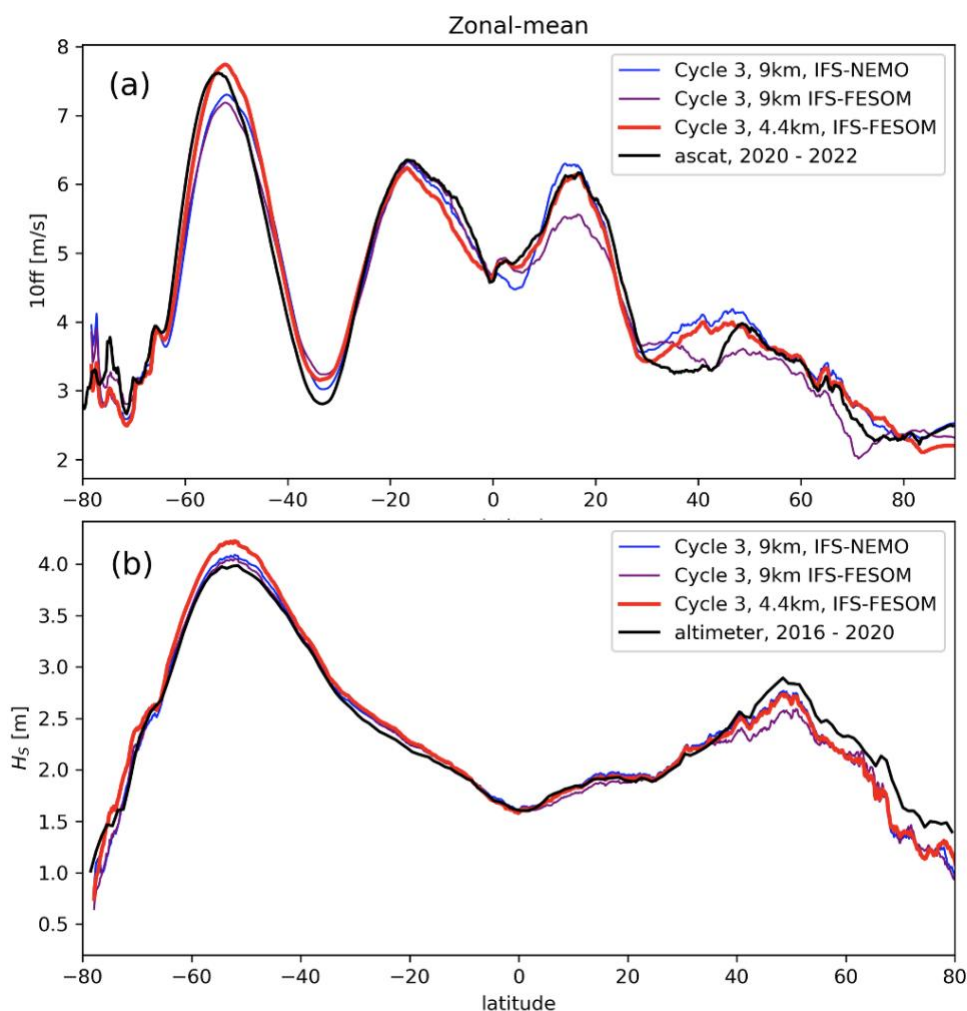
606  
607 When considering longer timescales (5-year simulations), model drifts are visible for the IFS-NEMO configuration and, to a  
608 lesser extent, for the IFS-FESOM setup. In particular, the NEMO setup appears to progressively lose the winter sea ice cover  
609 in the Southern Ocean (Fig. 11d). This behaviour is not compatible with the observed interannual variability of the Antarctic  
610 sea ice and it is likely due to the near-surface temperature warming, which is not affecting the IFS-FESOM setup. Our  
611 hypothesis is that the initialisation strategy for FESOM and NEMO accounts for part of the discrepancies in the multi-year  
612 drift between IFS-NEMO and IFS-FESOM. We found that active data assimilation improved the model performance for the  
613 initial months, while an uncoupled ocean spinup might be preferable for minimizing the drift towards the ocean model's  
614 equilibrium state during the 5-year coupled simulation. In the Arctic, the sea ice extent tends to increase progressively in both  
615 the FESOM and NEMO setups, with an additional dampening of the seasonal cycle observed for NEMO (Fig. 11c). Different  
616 multi-year drift regimes between NEMO and FESOM could be also attributed to diverse complexity of the underlying sea ice  
617 models. The more sophisticated physical parametrizations of the NEMO V3.4 configuration could respond more to the active  
618 coupling with IFS compared to the FESOM setups.

#### 619 **3.2.4 Wind and waves**

620 As written above in Section 2, in the IFS there is an active two-way coupling between the atmosphere and ocean waves. Surface  
621 wind stress generates ocean surface waves and in turn those waves modulate the wind stress. The increase in resolution from  
622 4.4km relative to the 9km for the IFS-FESOM simulations results in significant increases in wind speed in the storm tracks  
623 (~50S and ~45N; Fig. 12a), most likely due to the increased ability to resolve the intense winds in the extratropical cyclones.  
624 This increased resolution looks to be particularly important for the Southern Ocean, as the 4.4km simulation is the only one of  
625 the three simulations that can achieve winds of realistic intensity in this area. We also note a significant improvement in the  
626 trade winds (~15N) for the 4.4km IFS-FESOM simulation.



627



628

629

630

631

632

633

634

635

636

637

638

**Figure 12: Zonal-means of 10-metre wind speed ‘10ff’ over ocean (a) and significant wave height (b) in nextGEMS Cycle 3.** Observations in black are from Copernicus Marine Service for wind speed (‘ascat’; scatterometer combined with ERA5), and the ESA-CCI (v3) cross-calibrated altimeter record for wave height (‘altimeter’).

The waves in the storm tracks are also significantly larger (Fig. 12b). The increased wind is likely partly responsible for this increase. The second factor likely playing a role here is the change in fetch, i.e. the area of ocean over which the wind is contributing to wave growth. A notable decrease in mean sea ice concentration (more than ten percent) takes place in the 4.4km simulation (Fig. E1a), thereby freeing up the ocean surface here for wave growth. These changes can be directly seen in the wave field in the according areas (Fig. E1b). These waves then continue to grow with the wind as they propagate into the Southern Ocean, thereby contributing to the larger waves seen in this region. For the NH storm track, this points to an





639 improvement with respect to altimeter observations, but for the Southern Ocean the 4.4km simulation is now somewhat  
640 overestimating the waves.

### 641 **3.3 Land**

#### 642 **3.3.1 Key issues and model developments**

643  
644 Performing simulations at the km-scale inherently brings a richer picture in the atmosphere and ocean in terms of small-scale  
645 features, as more scales become explicitly resolved. To gain the full benefit of the resolution over land, it is important that the  
646 surface information is also at an equivalent or finer resolution. Therefore, work at ECMWF in recent years has been directed  
647 to provide the IFS surface model ECLand (Bousetta et al., 2021) with surface global ancillary information of a resolution down  
648 to 1 km or finer, and to include additional processes that become relevant at those scales. These developments had always the  
649 improvement of the operational IFS as a goal and focused, therefore, on timescales from days to a few months. nextGEMS  
650 simulations present a timely opportunity to test these changes in parallel before they become operational, and to assess their  
651 impact when fully coupled on multi-annual timescales. Most of the developments in this section are described in more detail  
652 by Bousetta et al. (2021). Here in this section, nextGEMS Cycle 2 and Cycle 3 will refer to IFS CY48r1 (ECMWF, 2023b)  
653 and CY49r1 (scheduled for 2024), respectively.

#### 654 **Km-scale surface information**

655  
656  
657 An improved land-water mask was included for nextGEMS Cycle 2. The original source belonging to the Joint Research  
658 Centre (JRC) had a nominal resolution of 30m. The mask was further improved by including glacier data and new land-water  
659 and lake fraction masks. In parallel, lake depth data was improved (Bousetta et al., 2021).

660  
661 Further changes to the land-water mask were tested in nextGEMS Cycle 3. The Land Use/Land Cover maps (LU/LC) used  
662 before nextGEMS Cycle 3 were based on those from GLCCv1.2 data (Loveland et al., 2000), which is based on observations  
663 from the Advanced Very High Resolution Radiometer (AVHRR) covering the period 1992–1993. They had a nominal  
664 resolution of about 1km. In nextGEMS Cycle 3, we used new maps, based on ESA-CCI, which exploit the high resolution of  
665 recent remote sensing products down to 300m and will pave the way to enable observation-based dynamic LU/LC maps in the  
666 future. These maps lead to a more realistic overall increase of low vegetation cover compared to the GLCCv1.2-based maps,  
667 at the expense of the high vegetation cover. The new conversion from ESA-CCI to the Biosphere-Atmosphere Transfer Scheme  
668 (BATS) vegetation types used by ECLand also reduces the presence of ambiguous vegetation types like ‘interrupted forest’ or  
669 ‘mixed forest’. In addition, work has been done on upgrading the Leaf Area Index (LAI) seasonality and its disaggregation  
670 into low and high-vegetation LAI. This improves, among others, the previously found overestimation of total LAI during  
671 March-April-May (MAM) and September-October-November (SON). This revised description of the vegetation will also be



672 used in the next operational IFS cycle (49R1), and an initial implementation and evaluation is presented in Nogueira et al  
673 (2021).

674

675 The thermodynamic effects of urban environments emerge at the surface as models refine resolution down to the km-scale and  
676 the rural-urban contrast sharpens. To determine where to activate the urban processes at the surface, a global map of urban  
677 land cover is used here in our nextGEMS Cycle 3 simulations. This map, based on information provided by ECOCLIMAP-  
678 SG at an initial 300m horizontal resolution (McNorton et al., 2023; Faroux et al., 2013), will also be used in the next operational  
679 IFS cycle (49R1).

680

### 681 **Km-scale surface processes**

682 The presence of the fine spatial information described above opens the path to simulate relevant km-scale processes and  
683 interactions. In particular, the representation of snow, 2-metre temperature, and urban areas was improved as detailed in the  
684 following.

685 A newly developed multi-layer snow scheme was implemented in IFS CY48r1 and was already used in the nextGEMS Cycle  
686 2 (Arduini et al. 2019), substituting the existing snow bulk-layer scheme. The new scheme dynamically varies the number of  
687 snow model layers depending on the snow depth and provides snow temperature, density, liquid water content and albedo as  
688 prognostic variables. In addition, snow and frozen soil parameters were modified for improved river discharge (Zsoter et al.,  
689 2022) and permafrost extent (Cao et al. 2022). An additional upgrade in nextGEMS Cycle 3 was a package of changes to  
690 ECLand which will be included in the next operational IFS cycle (49R1). This contains an improved postprocessing of 2-metre  
691 temperature reducing the warm bias present occasionally under very stable conditions. It also contains a significant upgrade  
692 to the representation of the near-surface impact of urbanized areas. For this purpose, the urban scheme developed in ECLand  
693 was activated. This scheme considers the urban environment as an interface connecting the sub-surface soil and the atmosphere  
694 above (McNorton 2021, McNorton 2023). The urban tile comprises both a canyon and roof fraction. In terms of energy and  
695 moisture storage, the uppermost soil layer is not specific to the tile but represents a grid-cell average. This results in a weighted  
696 average that accounts for both urban and non-urban environments. The albedo and emissivity values used in radiation exchange  
697 computations (McNorton 2021, McNorton 2023) are determined based on an assumption of an "infinite canyon," taking into  
698 account "shadowing." The roughness length for momentum and heat follows the model proposed by Macdonald et al. (1998)  
699 and varies according to urban morphology. Simplified assumptions regarding snow clearing and run-off are incorporated based  
700 on literature estimates (e.g., Paul & Meyer, 2001). Illustrative examples of urban cover characteristics and the impact of  
701 accounting for urbanised areas in Cycle 3 vs Cycle 2 simulations are highlighted in Section 4.3.



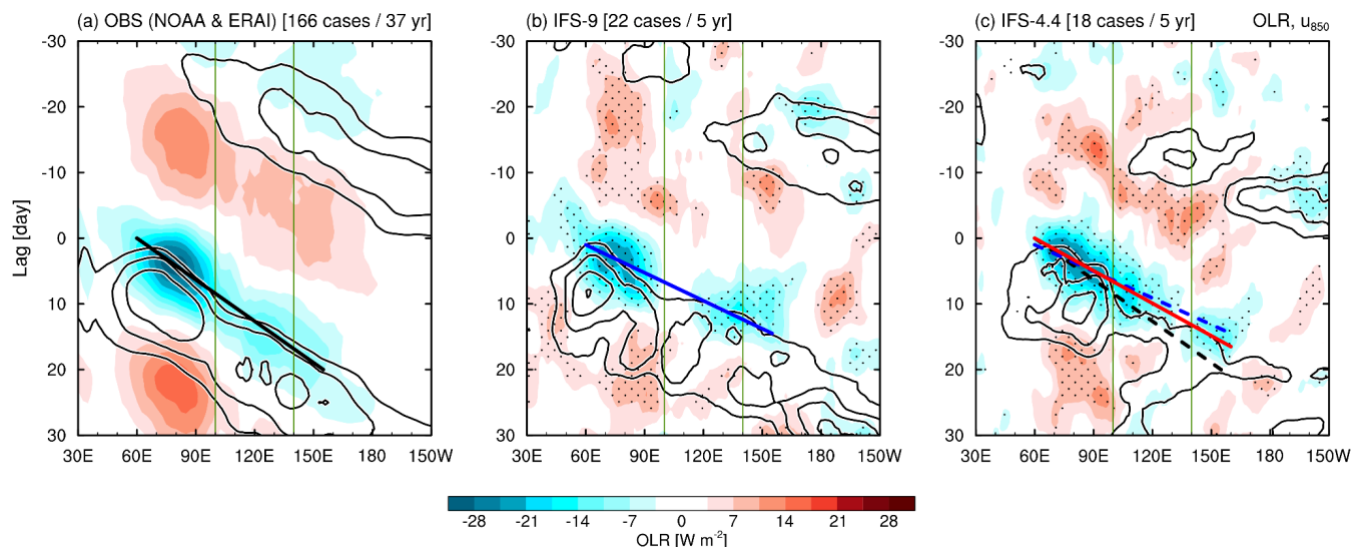
#### 702 **4 Selected examples of significant advances in km-scale nextGEMS simulations**

703 In this section, we will highlight three examples of notable advances in the Cycle 3 4.4km nextGEMS simulations that emerge  
704 due to the km-scale character of our simulations. Besides successes in the representation of the Madden-Julian Oscillation  
705 (MJO), an important variability pattern that is linked to the monsoons, we also provide examples of small-scale air-sea ice  
706 interactions in the Arctic, and touch on atmospheric impacts due to the new addition of km-scale cities in the IFS. We expect  
707 more in-depth process studies as part of ongoing analyses within the nextGEMS community and as part of dedicated future  
708 work.

#### 709 **4.1 MJO propagation and spectral characteristics of tropical convection**

710 The MJO is a dominant intraseasonal variability mode in the tropics, characterised by slow eastward propagation of large-  
711 scale convective envelopes over the Indo–Pacific warm pool (Madden and Julian, 1972). The MJO convection and circulations  
712 have profound impacts on weather and climate variability globally (Zhang, 2013), so that it is important to reproduce the MJO  
713 in global circulation models (GCMs) targeting seasonal-to-decadal simulations. Having the MJO well represented in models  
714 is indicative of a better tropical or global circulation. Because the reproducibility of the MJO is highly sensitive to the treatment  
715 of cumulus convection (e.g., Hannah and Maloney, 2011), many conventional GCMs that adopt cumulus parametrizations,  
716 which have uncertainties in the estimation of cumulus mass fluxes and moistening and heating rates, still struggle with  
717 simulating important MJO characteristics such as amplitudes, propagation speeds, and occurrence frequencies appropriately  
718 (e.g., Ling et al., 2019; Ahn et al., 2020; Chen et al., 2021). This issue might be improved by km-scale simulations as a result  
719 of more accurate representation of moist processes, as represented by the first success of an MJO hindcast simulation with  
720 NICAM (Miura et al. 2007), but also other physical processes (besides convection) play a role for skilful MJO simulations  
721 (Yano and Wedi, 2021).

722



723

724

725

726

727

728

729

730

731

732

733

734

735

736

737

738

739

740

741

742

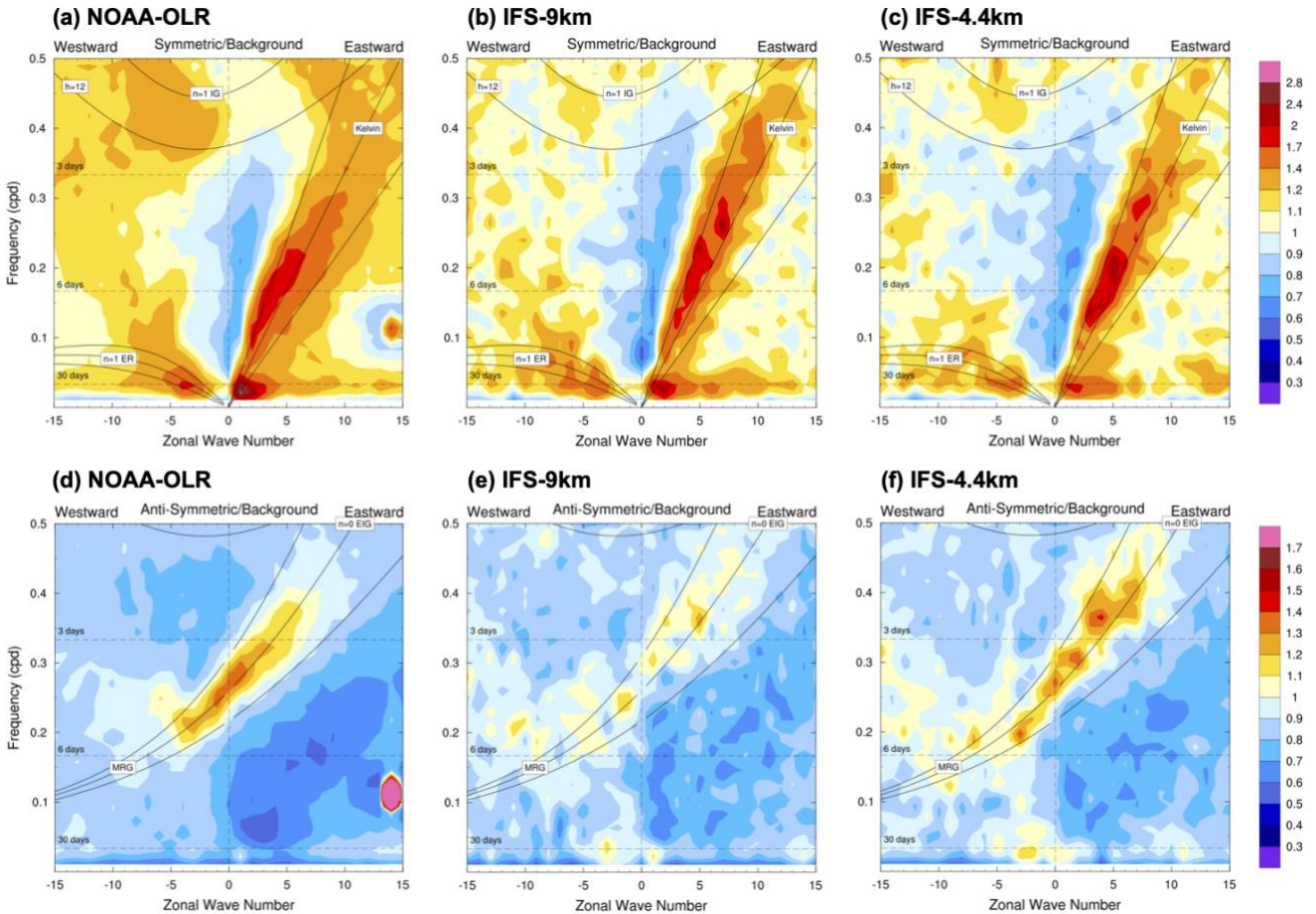
743

744

745

**Figure 13: Propagation characteristics of MJO convection and circulations composited from (a) observations and (b) IFS 9km simulation with NEMO and (c) IFS 4.4km simulation with FESOM.** Time–longitude diagrams of lagged-composite intraseasonal OLR (shading) and 850-hPa westerly wind anomalies (contours) averaged over 10°N–10°S. Contour interval is 0.5 m/s, with zero contours omitted. Stippling in (b) and (c) denotes statistical significance of OLR anomalies at the 90% level (All shading in (a) satisfies this significance). The number of detected MJO cases is denoted at the top of the figures together with analysis periods. Green lines indicate the longitudinal range over the Maritime Continent, and black, blue, and red lines indicate the centre of MJO convective envelopes for the observations, the 9 km simulation, and for the 4.4 km simulation, respectively.

Figure 13 illustrates the MJO propagation characteristics in the Cycle 3 4.4km IFS-FESOM simulation in comparison with the observations and the 9km IFS-NEMO simulation, using the MJO event-based detection method (Suematsu and Miura, 2018; Takasuka and Satoh, 2020). Note that the observational reference is made by the interpolated daily OLR from the NOAA polar-orbiting satellite (Liebmann and Smith, 1996) and ERA-Interim reanalysis (Dee et al. 2011) during the period of 1982–2018. While the 9km simulation already does a very good job and both the 9km and 4.4km simulations can reproduce the overall eastward propagation of MJO convection coupled with zonal winds (Figures 13b and 13c), the 4.4km simulation allows to improve even further in terms of amplitudes and propagation speeds. Specifically, MJO convective envelopes in the 4.4km simulation are continuously organised when they propagate into the Maritime Continent (see OLR anomalies in 100°–120°E), and their propagation speeds become slower than in the 9km simulation and thus closer to those in the observation. We hypothesize that km-scale resolutions and partially resolved convection can better represent convective systems around complex land-sea distributions and topography. Nevertheless, the 4.4km simulation still retains several biases compared to the observed MJOs such as much faster propagation and weaker convection amplitudes to the east of 120°E (i.e., the eastern part of the Maritime Continent).



746

747

748

749

750

751

752

753

754

755

756

757

758

759

**Figure 14: Wavenumber-frequency power spectra of equatorially (a-c) symmetric and (d-f) antisymmetric components of tropical convection measured by OLR anomalies in (a, d) observations, (b, e) IFS 9km simulation with NEMO, and (c, f) IFS 4.4km simulation with FESOM.** Power spectra are summed from 15°S to 15°N, and plotted as the ratio of raw to background power. Abbreviations of WIG, TD, ER, MRG, and EIG indicate westward inertia-gravity waves, tropical depressions, equatorial Rossby waves, mixed Rossby-gravity waves, and eastward inertia-gravity waves, respectively. Dispersion curves for corresponding equatorial waves are plotted for equivalent depths  $h = 12, 25,$  and  $50$  m.  $n$  denotes the number of meridional modes.

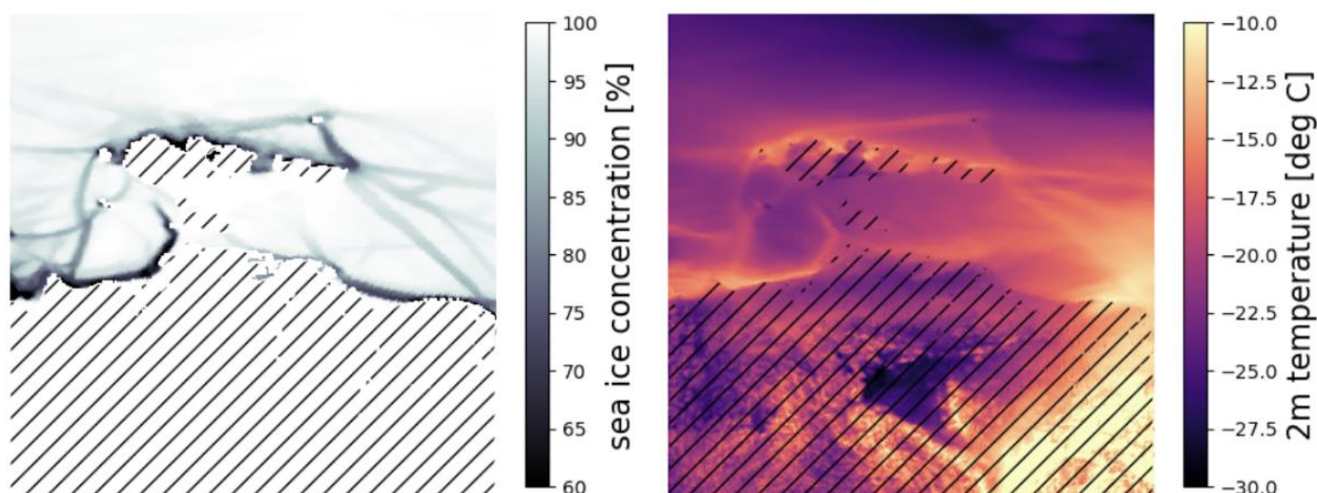
Notwithstanding the intricacies of tropical mesoscale circulations (Stephan et al, 2021), we further compare with linear Fourier analysis the appearance of convectively coupled equatorial wave activities between the observation and 9km and 4.4km simulations (Figure 14), following the methodology of Takayabu (1994) and Wheeler and Kiladis (1999). Several previous studies also evaluated the representation of equatorial waves in IFS simulations (Dias et al., 2018; Bengtsson et al., 2019). For the equatorially symmetric components of tropical convection (Figures 14a–c), the IFS simulations at both resolutions can





760 simulate Kelvin waves separated from the MJO, whereas the amplitudes of equatorial Rossby waves and tropical depression-  
761 type disturbances (i.e., westward-propagating systems in several-day periods) are somewhat underestimated especially in the  
762 4.4km simulation. Meanwhile, the representation of the equatorially antisymmetric wave modes are significantly improved in  
763 the 4.4km simulation; both  $n = 0$  eastward inertia-gravity waves and mixed Rossby-gravity waves can be reproduced with  
764 amplitudes as large as in the observation.

#### 765 4.2 Sea ice imprint on the atmosphere



766  
767 **Figure 15: Imprint of simulated Arctic sea ice leads on 2m-temperature in the Laptev Sea and East Siberian Sea.** (left)  
768 Sea ice concentration field, (right) 2m-temperature field. The panels depict 13 February 2020, 08:00, in the IFS-FESOM Cycle  
769 3 simulation with TCo2559 (4.4 km), coupled to the NG5 ocean (~4-5 km resolution in this area). Dashed lines represent land  
770 areas.

771 Leads are narrow open areas in the sea ice cover that typically form after deformation events, such as caused by a persisting  
772 Arctic storm over the ice cover. Individual leads can form typical ‘linear’ channels of several kilometres length, while the  
773 larger connected lead systems can extend up to hundreds of kilometres (Overland et al. 1995) or even cross the entire Arctic.  
774 They are detectable in satellite synthetic-aperture radar images (von Albedyll et al. 2023). Especially in winter, open leads can  
775 significantly impact the stability of the atmospheric column and other atmospheric parameters above them. A change in sea  
776 ice cover of 1% can cause near-surface temperature responses around 3.5 K (Lüpkes et al., 2008).

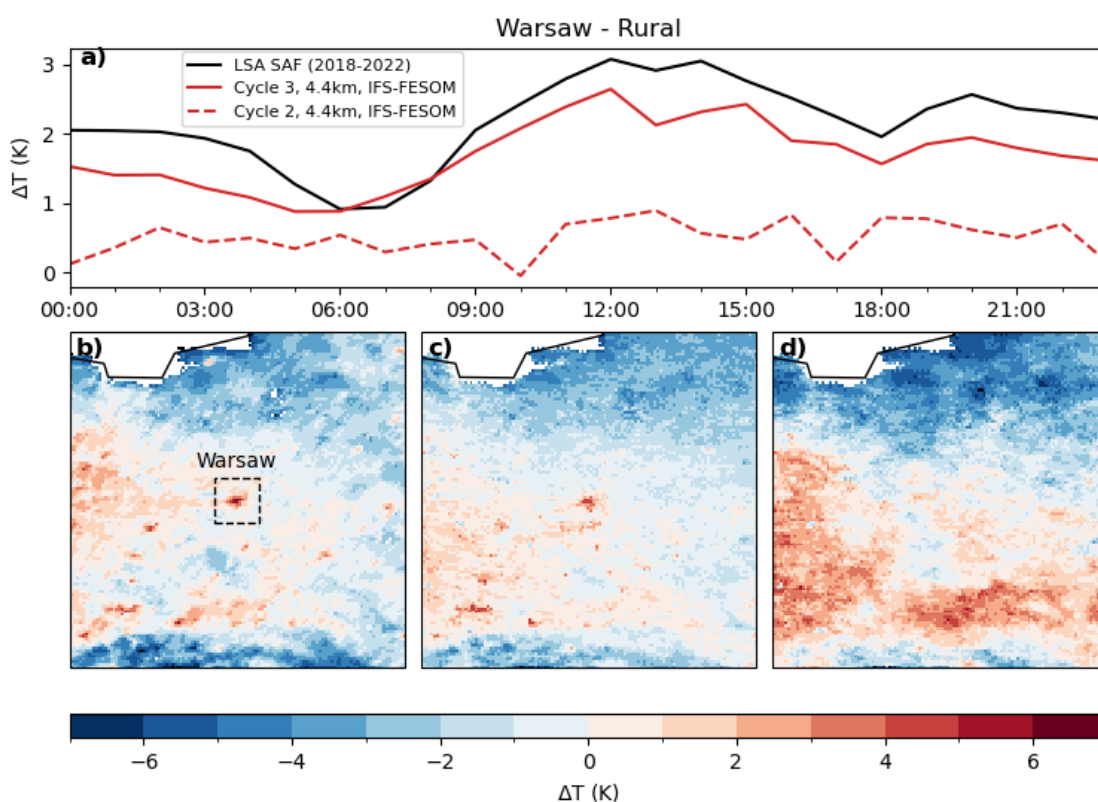
777 At the km-scale resolution employed here, there is first evidence of resolved linear kinematic features in the sea ice cover at a  
778 grid-spacing of ~4-5km in our coupled simulations (ECMWF News Item, 2022). With resolutions of 4.4km and 2.8km, the  
779 atmosphere can thus ‘see’ these narrow features in the sea ice cover and simulate a response explicitly. Similar to the effect





780 that meso-scale ocean eddies can have on the atmosphere above them (Frenger et al. 2013), we find that the leads in sea ice  
781 can strongly modulate the atmospheric state above them in our simulations. To give an example from the Arctic winter, north  
782 of Siberia in the Laptev and East Siberian Sea, due to the relatively warm ocean compared to the atmosphere, 2m-temperature  
783 anomalies over sea ice leads can often reach 10–20K against the surrounding closed sea ice cover background (Figure 15).  
784 While the realism with respect to the size, number, spatial distribution, and orientation of the simulated leads still needs to be  
785 quantified (Hutter et al. 2022), the direct simulation of sea ice lead effects within a coupled km-scale climate model is entirely  
786 novel and opens up new areas of research. Potential climate impacts of this air-ice-ocean interaction on the atmospheric  
787 column, such as Arctic clouds (Saavedra Garfias et al., 2023), will be one focus of our future work.

### 788 4.3 Cities and urban heat island effects



789

790

791 **Figure 16: Diurnal cycle of land surface temperature (LST) difference between the city of Warsaw and its rural**  
792 **surroundings**, for a) the summer months (JJA) during clear-sky conditions (5-year mean). The IFS 4.4km simulations are  
793 given with red lines (Cycle 2 dashed, Cycle 3 solid), observations from LSA SAF are given in black. The bottom panels show



794 JJA-mean clear-sky LST anomaly maps at 13:00 local time, with respect to the surrounding rural LST average, for b)  
795 observations from LSA SAF, for c) IFS 4.4km Cycle 3 with urban scheme, and for d) IFS 4.4km in Cycle 2 without urban  
796 scheme and using older land use/land cover maps.

797  
798 Between Cycles 2 and 3, significant improvements have been achieved in representing urban heat island effects around the  
799 globe at the km-scale (Fig. 16). To give an example, the difference in land surface temperature (LST) between the city of  
800 Warsaw and its more rural surroundings during the 5-year clear-sky hours (in the JJA season) depicts a clear urban heat island  
801 effect (Fig. 16, a), with temperature anomalies compared to the rural areas in exceedance of typically 1K over any given day,  
802 and exceeding 2K around noon. When comparing with observations from the Satellite Application Facility on Land Surface  
803 Analysis (LSA SAF) LST product (Trigo et al. 2008), the results in Cycle 3 show a closer fit to the satellite product than was  
804 possible in Cycle 2; both the average temperature difference over the day, as well as its temporal variability, is better captured  
805 (Fig. 16, a). Although the sub-diurnal variability is qualitatively well represented, the Cycle 3 modelled urban-rural contrast is  
806 systematically around 0.5 K smaller than in observations. We hypothesise that missing anthropogenic heating as well as an  
807 underestimation of the urban heat storage due to too low urban cover or building height may explain some of the discrepancies.  
808 In terms of spatial variability of LST JJA-mean clear-sky anomalies, our Cycle 3 4.4km IFS simulation (year 2020) matches  
809 km-scale details of the LSA SAF dataset (2018-2022) well (compare Fig. 16, b & c), while Cycle 2 4.4km IFS cannot provide  
810 this local detail in the absence of updated land use/land cover maps plus urban scheme (Fig. 16, d). Note also that the changes  
811 in high and low vegetation cover and vegetation types in Cycle 3 impact positively on the areas found to be too warm in Cycle  
812 2 in the South and East of Warsaw. These results illustrate clearly that high-resolution surface information as well as an urban  
813 scheme will be necessary in the context of the increasing need for local climate information on a city scale, and for local  
814 projections of direct socio-economic relevance.

## 815 **5 Summary and Conclusions**

816 In this paper, storm- and eddy-resolving simulations performed with the nextGEMS configurations of the ECMWF Integrated  
817 Forecasting System have been described and analysed. While we have also presented eddy-permitting simulations with IFS-  
818 NEMO as the ECMWF operational baseline configuration, we have focused mostly on IFS-FESOM runs that feature not only  
819 the highest atmospheric resolution (2.8km and 4.4km) but also an eddy-resolving ocean at 5km. The large-scale performance  
820 in terms of the mean state has been presented, such as top-of-the-atmosphere radiation balance and surface temperature biases,  
821 but also important variability patterns (e.g. MJO and QBO) that can be analysed in 5-year long simulations. The illustrated set  
822 of emerging advances in the km-scale nextGEMS simulations are first indications of the added value of km-scale modelling  
823 and explicit simulation of smaller scales. We expect to be able to show more of these examples once longer simulations will  
824 be available from the multi-decadal production simulations planned in nextGEMS for 2024. In this study it is the first time  
825 that the model configuration and quality of the simulations with IFS-FESOM have been described; and it thus represents a



826 significant milestone both in terms of documenting this novel model capability and the scientific readiness of the coupled  
827 modelling system.

828

829 A number of model developments along the nextGEMS model development cycles allowed to increase the realism of the km-  
830 scale simulations. For example, activating mass fixers for water vapour, cloud liquid, ice, rain and snow made global water  
831 non-conservation negligible and reduced energy non-conservation to an amount that is acceptable for long climate simulations,  
832 even though further progress could be made by adding an energy fixer that corrects temperature. Importantly, global water  
833 conservation turns out to be beneficial not only for long climate integrations, but also for the quality of ECMWF's medium-  
834 range weather forecasts. Work for ECMWF's recent operational IFS upgrade in June 2023 (48r1) showed that the model  
835 changes performed to fix the water and energy imbalances reduce the overestimation of mean precipitation at different  
836 timescales and improve the skill scores for the recent operational resolution upgrade for medium-range ensemble weather  
837 forecasts (ECMWF Newsletter 172, 2022). For example, the mean absolute error of precipitation against rain gauge  
838 measurements is about 2–3% smaller in 9 km forecasts that ensure global water conservation compared to 9km forecasts  
839 without water conservation. This is a great example of a model development from the nextGEMS multi-year simulations  
840 feeding into the improvement of the operational NWP system at ECMWF.

841

842 Variability patterns that can be studied with the 5-year simulations performed so far in nextGEMS are the Madden-Julian  
843 Oscillation (MJO) and the Quasi-Biennial Oscillation (QBO) in the equatorial stratospheric winds. The QBO is simulated with  
844 reasonable periodicity, which is typically challenging for km-scale models without any active parametrization for deep  
845 convection. The remaining shown deficiencies are likely due to the overly active vertical diffusion parametrization in stable  
846 conditions, which will be addressed in an upcoming version of the IFS. The MJO is similarly well represented in both the 9km  
847 and 4.4km simulations. In particular, however, MJO convective envelopes are continuously organised in the 4.4km simulation  
848 when they propagate over the Maritime Continent, which is closer to observations. We think that this is not just an effect of  
849 sampling different numbers of MJO events in our simulations and in the observations (simulated 5-year periods at 9km and  
850 4.4km resolution versus long-term observational period) since the observed MJO for shorter periods of time (e.g., 2011-2015)  
851 shows a similar result to the full observational record. The realistic representation of tropical variability and wave activity in  
852 the IFS at 9km and 4.4km is the result of 15 years of sustained efforts in model developments, notably convection, cloud-  
853 radiation interaction, and air-sea coupling (Bechtold et al. 2008, Dias et al 2018). The documented further improvements in  
854 the 4.4km simulation compared to 9km can possibly result from reduced cloud base mass fluxes (i.e., more weight on explicit  
855 convection), although the further detailed examination is left for our future work.

856

857 With our km-scale simulations that resolve mesoscale ocean eddies over large parts of the globe, we can also investigate  
858 coupled effects between sea ice leads, open narrow channels in the sea ice cover, and the atmosphere above them for the first  
859 time. Leads form during deformation events and can span over distances from several to hundreds of kilometres. From limited



860 observations and field campaigns it is known that sea ice leads can significantly impact the stability and temperature of the  
861 atmospheric column, especially in winter. We find that our model can resolve the linear features of the leads and represent  
862 explicitly the resulting heating of the atmosphere. This is a novel and promising approach that reveals new aspects of the air-  
863 ice-ocean interaction.

864

865 The nextGEMS model configurations are also starting points for the Climate Adaptation Digital Twin in the Destination Earth  
866 initiative, which aims to provide local climate information, for instance at the scale of cities, globally. The urban heat island  
867 effect, which is the phenomenon of higher temperatures in urban areas compared to rural areas, is an aspect of socio-economic  
868 importance that will need to be accurately represented by km-scale models in the future. In this study, we have shown that the  
869 implementation of an urban scheme in the IFS for nextGEMS Cycle 3 can significantly improve the simulation of land surface  
870 temperature (LST) over urban areas around the world, compared to previous model cycles that were missing specific urban  
871 tiles. The example of Warsaw illustrates the improvement in both temporal and spatial variability of land surface temperatures  
872 when compared to observations. We have also identified some limitations, such as nocturnal LST differences, which may be  
873 related to the lack of some anthropogenic heating in the model. Our first results here demonstrate the necessity and benefit of  
874 using an urban scheme in km-scale models for future efforts to provide reliable local climate information at the city scale.

875

876 While kilometre-scale model resolution is of benefit for the representation of the atmosphere, ocean, sea ice and land, it is also  
877 of importance for our understanding of other components of the climate system that have not been covered in this study yet,  
878 such as deep ocean circulation and ice sheet behaviour. For example, ocean heat transport at depth towards the Antarctic ice  
879 sheet and ice-shelf cavities is localised in narrow canyons (Morrison et al. 2020). To resolve bathymetric features like this and  
880 their potentially far-reaching impacts could be a strength of high-resolution models. Another example is the equilibration of  
881 the Antarctic Circumpolar Current, which is a balance of the wind-driven circulation and the opposing eddy-induced  
882 circulation cells. While transient ocean eddies can be parametrized to some degree, the effect of standing eddies (or meanders  
883 of this current) are beyond what parametrizations can achieve (Bryan et al., 2014). First studies indicate that explicit simulation  
884 of these effects with km-scale ocean models might be warranted to achieve higher confidence in projections of the Southern  
885 Ocean and global sea level rise (van Westen and Dijkstra, 2021; Rackow et al. 2022).

886

887 We have demonstrated that kilometre-scale modelling, which will soon enable multi-decadal simulations, has become feasible  
888 and offers advantages over lower-resolution models. The results presented here prove that our seamless model development  
889 approach, where numerical weather prediction models are extended for km-scale multi-decadal climate applications, is useful  
890 (Randall and Emanuel, 2024) and can benefit the original NWP application as well. As we have shown by running those  
891 models for 5 years, the km-scale simulations improve the representation of atmospheric circulation and extreme precipitation,  
892 but also enhance the coupling between the atmosphere, land, urban areas, ocean, and sea ice. We have revealed novel  
893 interactions among these components for the first time that will be further explored in ongoing work. With upcoming multi-



894 decadal simulations from the nextGEMS and Destination Earth projects we will be able to generate even more statistics on  
895 km-scale modelling soon, with an extended set of simulations from several models. These projects aim to provide accurate  
896 and globally consistent information on local climate change - at the scales that matter for individual cities or local impact  
897 modelling.

898

899

900

901

902

### 903 **Appendix A - Conservation properties of the IFS advection scheme and mass fixer approach**

904

905 The IFS uses a semi-Lagrangian (SL) advection scheme which is unconditionally stable and accurate and hence  
906 computationally efficient. It is also multi-tracer efficient as many tracers can be transported with a relatively small overhead:  
907 to advect a tracer or a prognostic variable (e.g. temperature, wind components), the upstream locations of model grid-points  
908 must be computed (departure points) and the tracer must be interpolated at these locations for each advected variable (for  
909 details, see Diamantakis and Vána 2021). However, despite being accurate and efficient, as a tracer transport scheme it lacks  
910 the property of conservation. In the absence of sources/sinks, the global mass of a tracer should remain constant, however, SL  
911 advection changes slightly its global mass. This change depends strongly on the spatial characteristics of the tracer such as  
912 smoothness of the field and its geographic location, with larger conservation errors for tracers that have sharp gradients and  
913 interact with the orography.

914

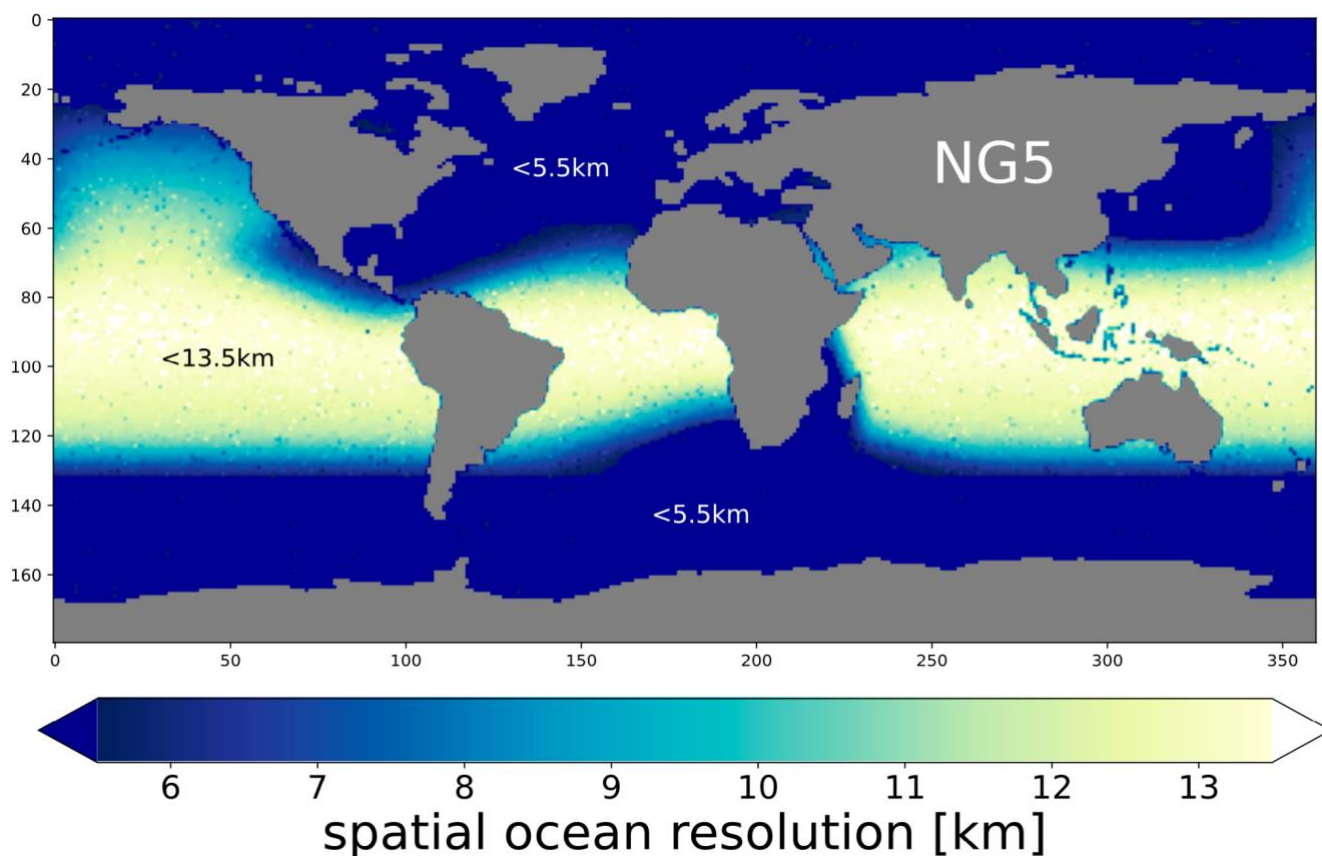
915 Conservation properties are important for water and energy budgets, especially for high resolutions. A practical solution that  
916 restores the global mass conservation of water tracers without altering the efficient and accurate numerical formulation of the  
917 IFS, is the mass fixer approach. However, simple mass fixers which change each tracer gridpoint value by the same proportion  
918 may result in unwanted biases in some regions. Hence, a more “local” approach is applied in the IFS advection scheme, which  
919 was originally developed and tested for atmospheric composition tracers yielding accurate results when compared against  
920 observations (Diamantakis and Fleming 2014, Diamantakis and Agusti-Panareda 2017). This is a “weighted” approach as the  
921 correction of the tracer field at each grid point depends on a weight factor which is proportional to a local error measure. The  
922 correction restores global conservation, using local criteria and it also preserves positive definiteness and monotonicity of the  
923 field.



924 **Appendix B**

925 The 5km nextGEMS ocean grid in this study (termed ‘NG5’) makes use of the multi-resolution mesh capabilities provided by  
926 the FESOM ocean-sea ice model (Figure B1). From nextGEMS Cycle 2 and following cycles, FESOM was run with this new  
927 eddy-resolving ocean grid with spacing of less than ~5km (at the poles) and around 13km in the tropics. This grid, specifically  
928 designed by the Alfred Wegener Institute (AWI) to better match the high atmospheric resolution of 4.4km in the IFS, allows  
929 to better resolve areas of particular interest at higher resolution, such as the Western boundary currents or the Southern Ocean.  
930 The mesh was created with the JIGSAW-GEO package (Engwirda, 2017).

931  
932



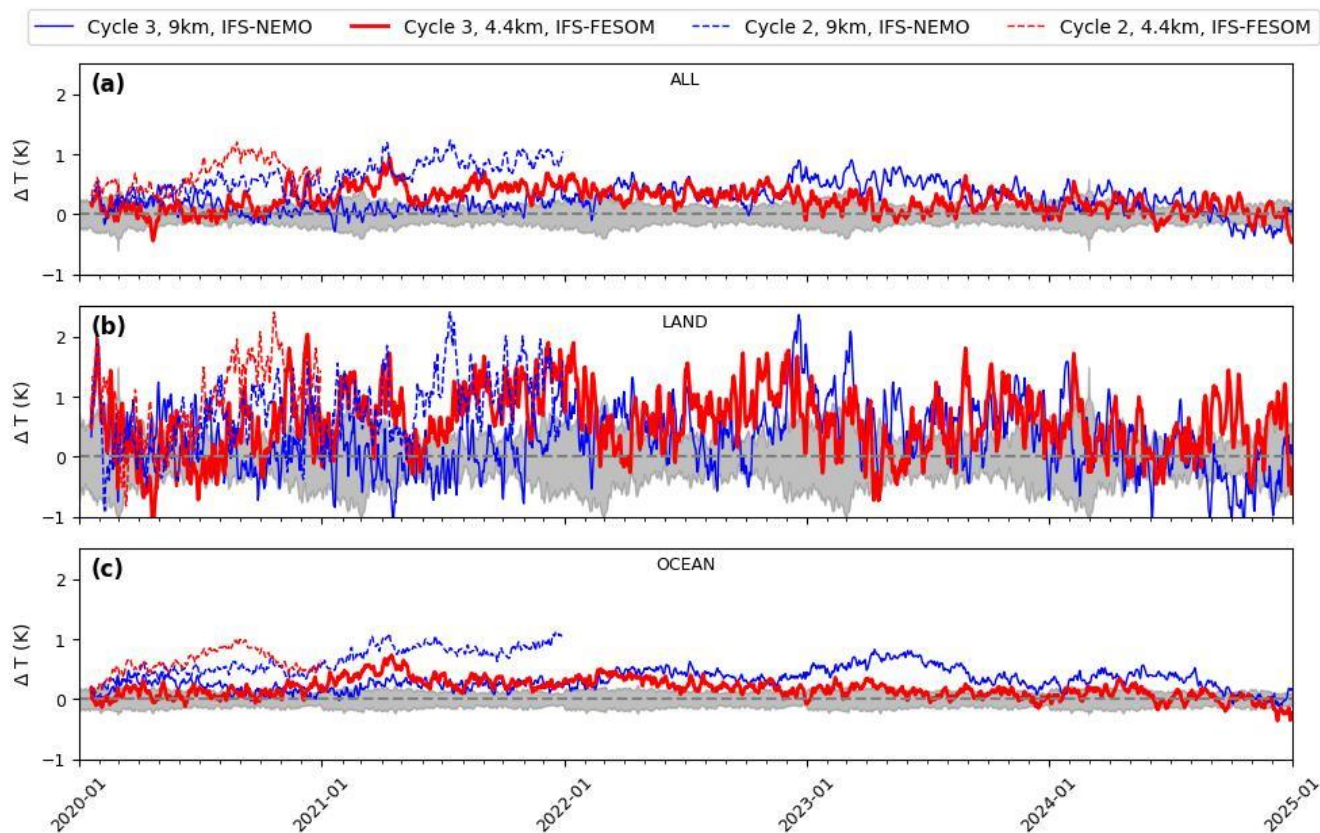
933  
934

**Figure B1: Spatial ocean resolution in the nextGEMS 5km grid, NG5 [km].**





935 **Appendix C**



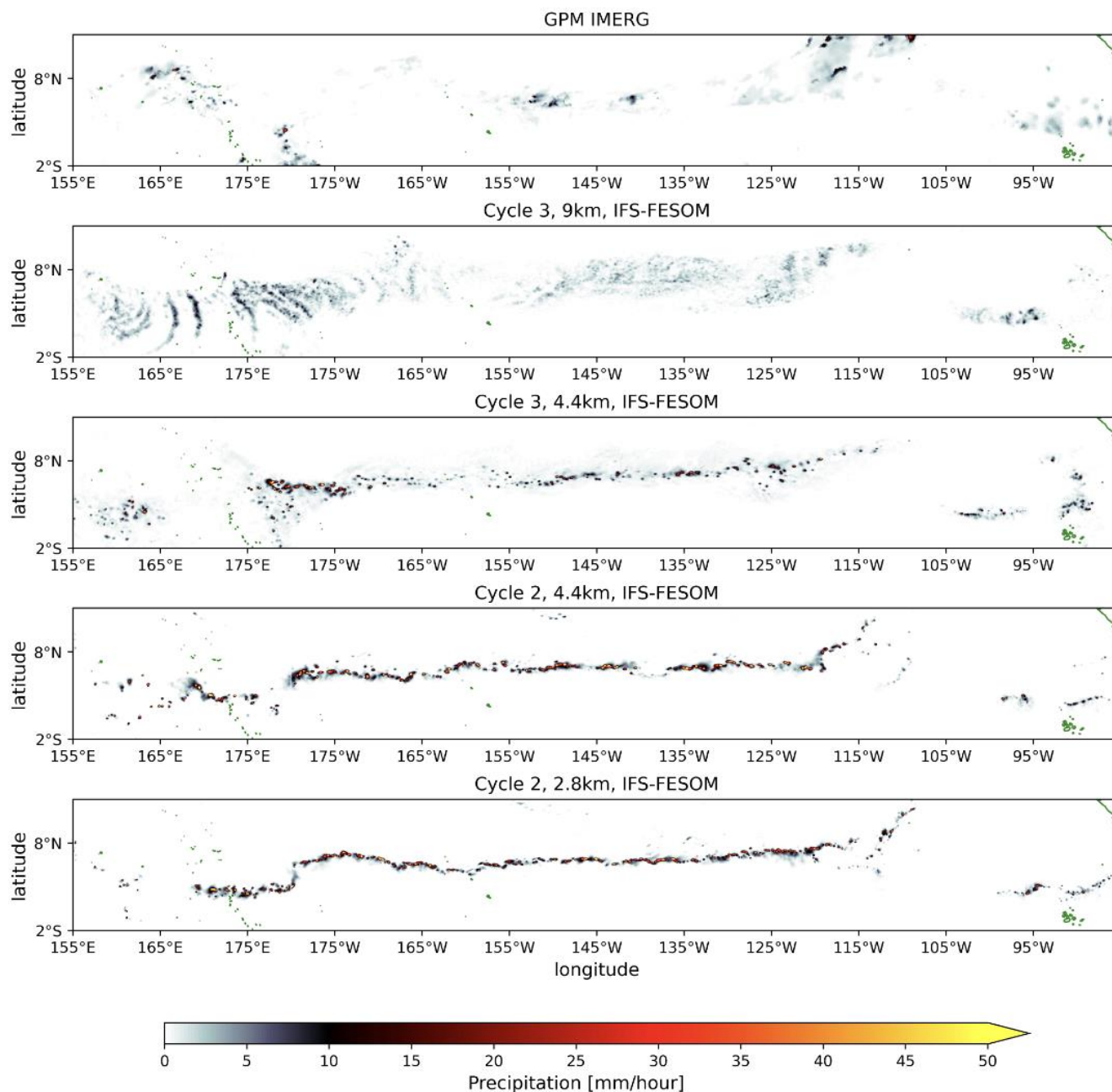
936 **Figure C1: Timeseries of mean 2-metre temperature in nextGEMS simulations for (a) global, (b) only over land, and**  
937 **(c) only over ocean with respect to ERA5, for the years 2020-2024. The shaded area shows the ERA5 standard deviation**  
938 **between 2012-2021.**

939

940



941 **Appendix D**



942

943

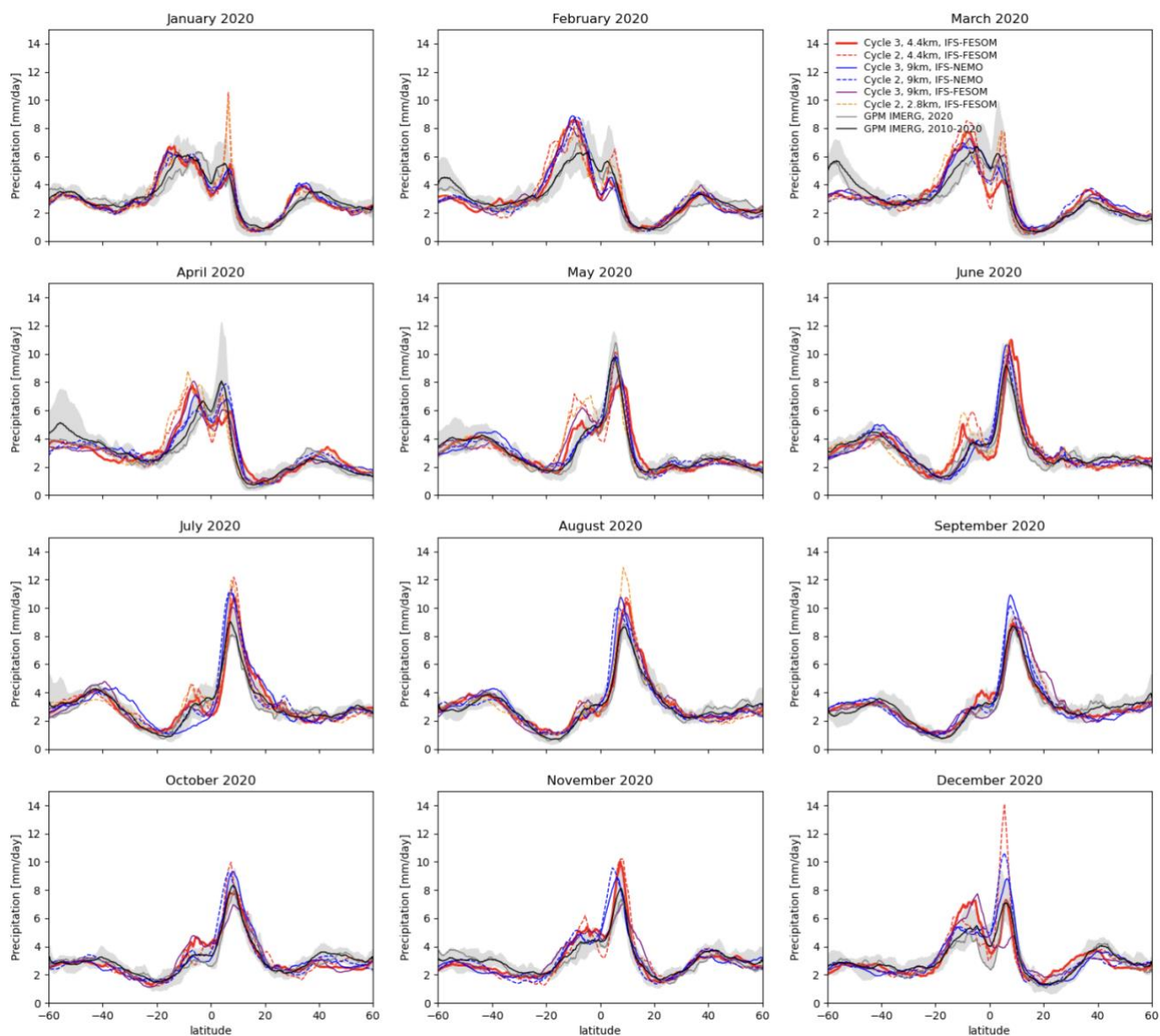
944

945

**Figure D1: Snapshots of precipitation in nextGEMS Cycle 2 and 3 simulations in the tropical Pacific at 5°N, compared to observations from GPM IMERG.** The ITCZ often organises into a continuous and persistent line of deep convection over the Pacific at 5°N in Cycle 2 at 4.4km and 2.8km resolution (lower two panels), with strongly overestimated zonal mean



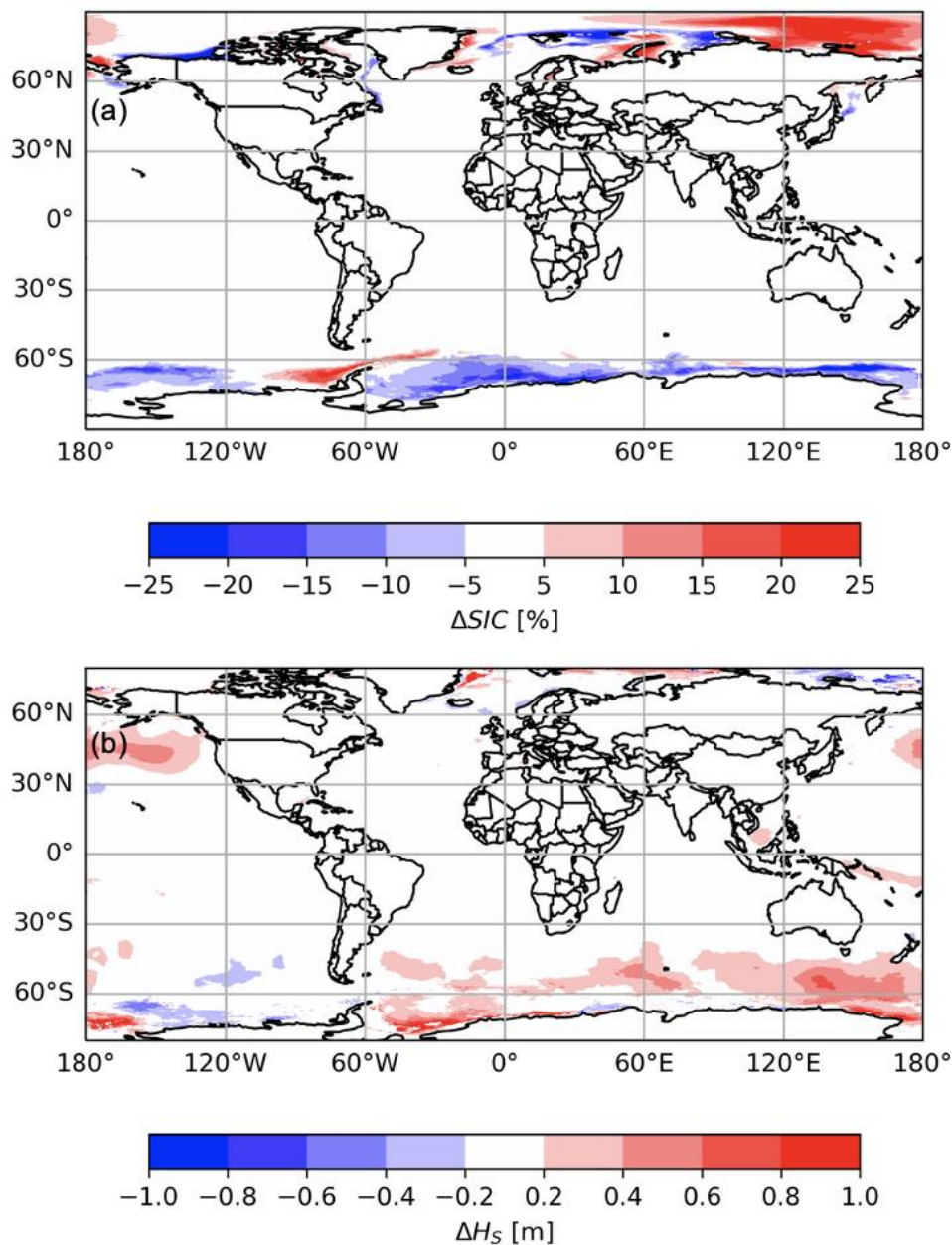
946 precipitation along this latitude. In Cycle 3 this has been addressed via a reduced cloud-base mass flux with 4.4km resolution.  
947 The 9km Cycle 3 simulation uses active deep convection parametrization (Deep On).  
948



949 **Figure D2: Zonal-mean precipitation for the individual months in the first year of Cycle 2 (dashed) and Cycle 3 (solid)**  
950 **simulations.** IFS-NEMO 9km simulations are in blue, while IFS-FESOM simulations are given in red (4.4km), orange  
951 (2.8km), and purple (9km).  
952  
953



954 **Appendix E**



955  
956 **Figure E1: Mean changes in sea ice concentration (a) and significant wave height (b) between the 4.4km and 9km IFS-**  
957 **FESOM simulations in nextGEMS Cycle 3 (4.4km minus 9km). Red (blue) indicates an increase (decrease) for the**  
958 **4.4km simulation.**  
959





## 960 **Code Availability**

961 The FESOM2.5 model is a free software and available from Github (<https://github.com/FESOM/fesom2>). The latest version 2.5 including  
962 all developments used in nextGEMS Cycle 3 is archived in a Zenodo repository, <https://doi.org/10.5281/zenodo.10225420> (Rackow et al.  
963 2023c). The ocean coupling interface to the Integrated Forecasting System (IFS) has been extracted for IFS-FESOM and is publicly available  
964 as part of the FESOM2.5 code above as well (folder `ifs_interface`). MultiIO, MIR, ECCODES and FDB are all free software and available at  
965 the ECMWF Github space, <https://github.com/ecmwf>. The IFS source code is available subject to a licence agreement with ECMWF.  
966 ECMWF member-state weather services and approved partners will be granted access. The IFS code without modules for data assimilation  
967 is also available for educational and academic purposes via an OpenIFS licence (see <http://www.ecmwf.int/en/research/projects/openifs>).  
968 For easier public access and review, the IFS code modifications from this study and developments detailed in section 3.1.1 for nextGEMS  
969 have also been separately archived in a Zenodo repository, <https://doi.org/doi/10.5281/zenodo.10223576> (Rackow et al. 2023b). Scripts and  
970 data to reproduce the figures and analysis of this paper can be found at <https://github.com/trackow/nextGEMS-paper/> (will be in Zenodo  
971 after review). Grib data in FDB were made available to hackathon participants using `gribscan` (Kölling, Kluff, and Rackow, 2024).

## 972 **Data Availability**

973 Data for our simulations are openly accessible and can be obtained either from the web (see DOIs below), from ECMWF's MARS archive,  
974 or directly from DKRZ's supercomputer Levante after registration (<https://luv.dkrz.de/register/>). The Cycle 2 data for 20 January 2020 to 31  
975 December 2020 of TCo2559-NG5 with deep convection parametrization disabled can be found at <https://dx.doi.org/10.21957/1n36-qg55>.  
976 The Cycle 2 data for TCo1279-ORCA025 (20 Jan 2020 to 31 December 2021) with deep convection parametrization active can be found at  
977 <https://dx.doi.org/10.21957/x4vb-3b40>. More Cycle 2 output, also for the nextGEMS sister model ICON, can be found at the World Data  
978 Center for Climate (WDCC), [https://dx.doi.org/10.26050/WDCC/nextGEMS\\_cyc2](https://dx.doi.org/10.26050/WDCC/nextGEMS_cyc2). Cycle 3 data for ICON and IFS can be found WDCC  
979 under [https://doi.org/10.26050/WDCC/nextGEMS\\_cyc3](https://doi.org/10.26050/WDCC/nextGEMS_cyc3) (Koldunov et al. 2023). Namelist files to reproduce the settings of the ocean,  
980 atmosphere, land, and wave model in the Cycle 3 simulations are archived in a Zenodo repository (Rackow et al. 2023a),  
981 <https://doi.org/10.5281/zenodo.10221652>. LSA SAF LST data are available from the LSA SAF data service under the link  
982 <https://datasaf.lsasvcs.ipma.pt/PRODUCTS/MSG/MLST/>.

## 983 **Author contributions**

984 TR led the writing of the paper and prepared the initial manuscript with TB and XPB. TR, TB, XPB, and IH performed the simulations. TB,  
985 XPB, RF, MD and TR developed the model code changes. The refactoring of the FESOM model has been led by DSi, NK, JS, and JH. Initial  
986 implementation of the IFS-FESOM single-executable coupling is joint work of KM and TR. NK created the 5km nextGEMS FESOM grid  
987 NG5 in discussions with TR. IP performed the QBO analysis. TB has analysed the precipitation characteristics and performed the TOA  
988 tuning. XPB contributed the 5-year temperature timeseries. SM performed TOA budget analyses. DT performed the MJO analyses. JB and  
989 JK contributed the wave model analyses. The city and urban heat island analyses are by XPB and ED. Sea ice performance indices are the  
990 work of LZ. TR performed the sea ice lead analysis. HFG provided ocean grid descriptions for coupling weight computations. In the paper,  
991 MD discussed the mass fixer approach and RF discussed the physics parametrizations. DSá added the multiIO section to the paper. TK, LK,  
992 and FZ helped with faster data access. All co-authors discussed and contributed to the final document.





993 **Competing Interests**

994 The authors declare that they have no conflict of interest.

995 **Acknowledgements**

996 This work used supercomputing resources of the German Climate Computing Centre (Deutsches Klimarechenzentrum, DKRZ) granted by  
997 its Scientific Steering Committee (WLA) under project ID 1235. We want to thank DKRZ staff for their continued support in terms of data  
998 handling, data hosting, and running of the presented Cycle 3 simulations, in particular Jan Frederik Engels, Hendryk Bockelmann, Fabian  
999 Wachsmann, Irina Fast, and Carsten Beyer. We want to thank colleagues at AWI for active discussions and their support towards the  
1000 upcoming multi-decadal simulations, in particular Suvarchal Kumar Cheedela, Bimochan Niraula, Rohit Ghosh, Sergey Danilov, and Patrick  
1001 Scholz. We also would like to thank all colleagues at ECMWF who are not co-authors but also had a substantial impact on km-scale model  
1002 development and modelling on climate timescales, e.g. Gabriele Arduini, Gianpaolo Balsamo, Magdalena Alonso Balmaseda, Margarita  
1003 Choulga, Jasper Denissen, Charles Pelletier, Christian Kuehnlein, Pedro Maciel, Joe McNorton, Simon Smart, Balthasar Reuter, James  
1004 Hawkes, Philipp Geier, Andreas Mueller, Michael Lange, Olivier Marsden, Sam Hatfield, Willem Deconinck, Matthew Griffith, Shannon  
1005 Mason, and Mark Fielding. We thank Philippe Lopez for providing the Meteosat 8 observations in Figure 6. We also want to thank the  
1006 international nextGEMS hackathon community, including many Early Career Researchers, who analysed our simulations in detail and helped  
1007 guide some of the model development efforts. This research has been supported by the European Commission Horizon 2020 Framework  
1008 Programme nextGEMS (grant no. 101003470). This work was also supported by the European Union's Destination Earth Initiative and  
1009 relates to tasks entrusted by the European Union to the European Centre for Medium-Range Weather Forecasts implementing part of this  
1010 Initiative with funding by the European Union.

1011 **References**

1012 Ahn, M. S., Kim, D., Kang, D., Lee, J., Sperber, K. R., Gleckler, P. J., ... & Kim, H. (2020). MJO propagation across the  
1013 Maritime Continent: Are CMIP6 models better than CMIP5 models?. *Geophysical Research Letters*, 47(11), e2020GL087250.

1014  
1015 Arduini, G., Balsamo, G., Dutra, E., Day, J. J., Sandu, I., Boussetta, S., & Haiden, T. (2019). Impact of a multi-layer snow  
1016 scheme on near-surface weather forecasts. *Journal of Advances in Modeling Earth Systems*, 11, 4687–4710.  
1017 <https://doi.org/10.1029/2019MS001725>

1018  
1019 Baldwin, M. P., et al. (2001), The quasi-biennial oscillation, *Rev. Geophys.*, 39(2), 179–229, doi:10.1029/1999RG000073.

1020  
1021 Bauer, P., Quintino, T., Wedi, N., Bonanni, A., Chrust, M., Deconinck, W., ... & Zanna, C. (2020). The ECMWF scalability  
1022 programme: Progress and plans. European Centre for Medium Range Weather Forecasts. <https://doi.org/10.21957/gdit22ulm>

1023



- 1024 Bauer, P., Dueben, P.D., Hoefler, T., Quintino, T., Schulthess, T., Wedi, N.P. The digital revolution of Earth-system science.  
1025 Nat Comput Sci 1, 104–113 (2021). <https://doi.org/10.1038/s43588-021-00023-0>  
1026
- 1027 Bauer, P., Quintino, T., and Wedi, N.P. (2022) From the Scalability Programme to Destination Earth, ECMWF Newsletter,  
1028 issue 171, pp. 15-22. DOI: 10.21957/pb2vnp59ks  
1029
- 1030 Bechtold, P., M. Köhler, T. Jung, M. Leutbecher, M. Rodwell, F. Vitart and G. Balsamo (2008). Advances in predicting  
1031 atmospheric variability with the ECMWF model: From synoptic to decadal time-scales. Quart. J. Roy. Meteor. Soc. 134,  
1032 1337-1351  
1033
- 1034 Bechtold, P., N. Semane, P. Lopez, J.-P. Chaboureau, A. Beljaars, and N. Bormann (2014). Representing equilibrium and  
1035 non-equilibrium convection in large-scale models. J. Atmos. Sci., 134, 1337-1351, <https://doi.org/10.1175/JAS-D-13-0163.1>.  
1036
- 1037 Becker, T., Bechtold, P. and Sandu, I., 2021: Characteristics of convective precipitation over tropical Africa in storm-  
1038 resolving global simulations. Quarterly Journal of the Royal Meteorological Society, 147(741), pp.4388-4407.  
1039 <https://doi.org/10.1002/qj.4185>  
1040
- 1041 ECMWF Newsletter 172: [https://www.ecmwf.int/en/newsletter/172/news/fixing-water-and-energy-budget-imbalances-](https://www.ecmwf.int/en/newsletter/172/news/fixing-water-and-energy-budget-imbalances-integrated-forecasting-system/)  
1042 [integrated-forecasting-system/](https://www.ecmwf.int/en/newsletter/172/news/fixing-water-and-energy-budget-imbalances-integrated-forecasting-system/), last access: 4 January 2024, Summer 2022.
- 1043 Beljaars, A. C. M., Brown, A. R. and Wood, N. (2004). A new parametrization of turbulent orographic form drag. Q. J. R.  
1044 Meteorol. Soc., 130, 1327-1347, <https://doi.org/10.1256/qj.03.73>.
- 1045 Bengtsson, L., J. Dias, M. Gehne, P. Bechtold, J. Whitaker, J.-W. Bao, L. Magnusson, S. Michelson, P. Pegion, S. Tulich and  
1046 G. Kiladis, 2019 : Convectively coupled equatorial wave simulations using the ECMWF IFS and the NOAA GFS cumulus  
1047 convection schemes in the NOAA GFS model. Mon. Wea. Rev, 147, 4005-4025 <https://doi.org/10.1175/MWR-D-19-0195.1>  
1048
- 1049 Bony, S., Stevens, B., Frierson, D. et al. Clouds, circulation and climate sensitivity. Nature Geosci 8, 261–268 (2015).  
1050 <https://doi.org/10.1038/ngeo2398>  
1051
- 1052 Boussetta, S.; Balsamo, G.; Arduini, G.; Dutra, E.; McNorton, J.; Choulga, M.; Agustí-Panareda, A.; Beljaars, A.; Wedi, N.;  
1053 Munõz-Sabater, J.; et al. ECLand: The ECMWF Land Surface Modelling System. Atmosphere 2021, 12, 723.  
1054 <https://doi.org/10.3390/atmos12060723>.  
1055



- 1056 Bozzo, A., Benedetti, A., Flemming, J., Kipling, Z., and Rémy, S.: An aerosol climatology for global models based on the  
1057 tropospheric aerosol scheme in the Integrated Forecasting System of ECMWF, *Geosci. Model Dev.*, 13, 1007–1034,  
1058 <https://doi.org/10.5194/gmd-13-1007-2020>, 2020.
- 1059
- 1060 Bryan, F. O., Gent, P. R., & Tomas, R.: Can Southern Ocean Eddy Effects Be Parameterized in Climate Models?,  
1061 *Journal of Climate*, 27(1), 411–425. Retrieved Dec 20, 2022, from [https://journals.ametsoc.org/view/journals/clim/27/1/jcli-  
1063 d-12-00759.1.xml](https://journals.ametsoc.org/view/journals/clim/27/1/jcli-<br/>1062 d-12-00759.1.xml), 2014.
- 1064 Bushell, A.C., Anstey, J.A., Butchart, N., Kawatani, Y., Osprey, S.M., Richter, J.H., Serva, F., Braesicke, P., Cagnazzo, C.,  
1065 Chen, C.-C., Chun, H.-Y., Garcia, R.R., Gray, L.J., Hamilton, K., Kerzenmacher, T., Kim, Y.-H., Lott, F., McLandress,  
1066 C., Naoe, H., Scinocca, J., Smith, A.K., Stockdale, T.N., Versick, S., Watanabe, S., Yoshida, K. and Yukimoto, S. (2022),  
1067 Evaluation of the Quasi-Biennial Oscillation in global climate models for the SPARC QBO-initiative. *QJR Meteorol Soc*,  
1068 148: 1459-1489. <https://doi.org/10.1002/qj.3765>
- 1069
- 1070 Cao, B., Arduini, G., and Zsoter, E.: Brief communication: Improving ERA5-Land soil temperature in permafrost regions  
1071 using an optimized multi-layer snow scheme, *The Cryosphere*, 16, 2701–2708, <https://doi.org/10.5194/tc-16-2701-2022>,  
1072 2022.
- 1073 Chen, G., Ling, J., Zhang, R., Xiao, Z., & Li, C. (2022). The MJO from CMIP5 to CMIP6: Perspectives from tracking MJO  
1074 precipitation. *Geophysical Research Letters*, 49(1), e2021GL095241.
- 1075 Crook, J., Klein, C., Folwell, S., Taylor, C.M., Parker, D.J., Stratton, R. and Stein, T. (2019) Assessment of the representation  
1076 of West African storm lifecycles in convection-permitting simulations. *Earth and Space Science*, 6(5), 818–835.  
1077 <https://doi.org/10.1029/2018EA000491>.
- 1078 Dai, A., T. Qian, K. E. Trenberth, and J. D. Milliman, 2009: Changes in Continental Freshwater Discharge from 1948 to  
1079 2004. *J. Climate*, 22, 2773–2792, <https://doi.org/10.1175/2008JCLI2592.1>.
- 1080 Danilov, S., Sidorenko, D., Wang, Q., and Jung, T.: The Finite-volume Sea ice–Ocean Model (FESOM2), *Geosci. Model*  
1081 *Dev.*, 10, 765–789, <https://doi.org/10.5194/gmd-10-765-2017>, 2017.
- 1082 Dee, D. P., Uppala, S. M., Simmons, A. J., Berrisford, P., Poli, P., Kobayashi, S., ... & Vitart, F. (2011). The ERA-Interim  
1083 reanalysis: Configuration and performance of the data assimilation system. *Quarterly Journal of the royal meteorological*  
1084 *society*, 137(656), 553-597.



- 1085 Diamantakis, M. and Váňa, F (2022). A fast converging and concise algorithm for computing the departure points in semi-  
1086 Lagrangian weather and climate models. *Q J R Meteorol Soc*, 148(743), 670–684, <https://doi.org/10.1002/qj.4224>  
1087
- 1088 Diamantakis, M. and Agusti-Panareda, A. (2017): A positive definite tracer mass fixer for high resolution weather and  
1089 atmospheric composition forecasts. [https://www.ecmwf.int/sites/default/files/elibrary/2017/17914-positive-definite-tracer-](https://www.ecmwf.int/sites/default/files/elibrary/2017/17914-positive-definite-tracer-mass-fixer-high-resolution-weather-and-atmospheric-composition.pdf)  
1090 [mass-fixer-high-resolution-weather-and-atmospheric-composition.pdf](https://www.ecmwf.int/sites/default/files/elibrary/2017/17914-positive-definite-tracer-mass-fixer-high-resolution-weather-and-atmospheric-composition.pdf).  
1091
- 1092 Diamantakis, M. and Flemming, J. (2014): Global mass fixer algorithms for conservative tracer transport in the ECMWF  
1093 model, *Geosci. Model Dev.*, 7, 965–979, <https://doi.org/10.5194/gmd-7-965-2014>.  
1094
- 1095 Dias, J., M. Gehne, G. N. Kiladis, N. Sakaeda, P. Bechtold and T. Haiden, 2018: Equatorial waves and the skill of NCEP and  
1096 ECMWF forecast systems. *Mon. Wea. Rev.* 146, 1763-1784. <https://doi.org/10.1175/MWR-D-17-0362.1>  
1097
- 1098 ECMWF (2023a): ECMWF IFS Documentation CY48R1 – Part III: Dynamics and Numerical Procedures. Reading, UK:  
1099 ECMWF, <https://doi.org/10.21957/26f0ad3473>, 2023.  
1100
- 1101 ECMWF (2023b): ECMWF IFS documentation CY48R1 – Part IV Physical processes. Reading, UK: ECMWF,  
1102 <https://doi.org/10.21957/02054f0fbf>, 2023.  
1103
- 1104 ECMWF (2023c): ECMWF IFS Documentation CY48R1 – Part VII: ECMWF Wave Model. Reading, UK: ECMWF,  
1105 <https://doi.org/10.21957/cd1936d846>, 2023.  
1106
- 1107 ECMWF News Item: [https://www.ecmwf.int/en/about/media-centre/news/2022/nextgems-probes-km-scale-resolutions-](https://www.ecmwf.int/en/about/media-centre/news/2022/nextgems-probes-km-scale-resolutions-integrated-forecasting-system/)  
1108 [integrated-forecasting-system/](https://www.ecmwf.int/en/about/media-centre/news/2022/nextgems-probes-km-scale-resolutions-integrated-forecasting-system/), last access: 4 January 2024, October 2022.  
1109
- 1110 Engwirda, D.: JIGSAW-GEO (1.0): locally orthogonal staggered unstructured grid generation for general circulation  
1111 modelling on the sphere, *Geosci. Model Dev.*, 10, 2117–2140, <https://doi.org/10.5194/gmd-10-2117-2017>, 2017.  
1112
- 1113 Fielding, M. D., S. A. K. Schäfer, R. J. Hogan, and R. M. Forbes (2020). “Parametrizing cloud geometry and its application  
1114 in a subgrid cloud-edge erosion scheme”. In: *Quarterly Journal of the Royal Meteorological Society* 146.729, pp. 1651–  
1115 1667. <https://doi.org/10.1002/qj.3758>.
- 1116 Forbes, R. M. and Tompkins, A. M. (2011). An improved representation of cloud and precipitation. *ECMWF Newsletter No.*  
1117 129, pp. 13-18.



- 1118 Forbes, R. M., Tompkins, A. M. and Untch, A. (2011). A new prognostic bulk microphysics scheme for the IFS. ECMWF  
1119 Tech. Memo. No. 649.
- 1120 Frenger, I., Gruber, N., Knutti, R. et al. Imprint of Southern Ocean eddies on winds, clouds and rainfall. *Nature Geosci* 6,  
1121 608–612 (2013). <https://doi.org/10.1038/ngeo1863>
- 1122
- 1123 Gao, K., Harris, L., Bender, M., Chen, J.-H., Zhou, L., & Knutson, T. (2023). Regulating fine-scale resolved convection  
1124 in high-resolution models for better hurricane track prediction. *Geophysical Research Letters*, 50, e2023GL103329.  
1125 <https://doi.org/10.1029/2023GL103329>
- 1126
- 1127 Garfinkel, C. I., Gerber, E. P., Shamir, O., Rao, J., Jucker, M., White, I., & Paldor, N. (2022). A QBO cookbook:  
1128 Sensitivity of the quasi-biennial oscillation to resolution, resolved waves, and parameterized gravity waves. *Journal of*  
1129 *Advances in Modeling Earth Systems*, 14, e2021MS002568. <https://doi.org/10.1029/2021MS002568>
- 1130
- 1131 Goessling, H. F., S. Tietsche, J. J. Day, E. Hawkins, and T. Jung (2016), Predictability of the Arctic sea ice edge,  
1132 *Geophys. Res. Lett.*, 43, 1642–1650, DOI:10.1002/2015GL067232.
- 1133
- 1134 Griffies, S. M., and Coauthors, 2015: Impacts on Ocean Heat from Transient Mesoscale Eddies in a Hierarchy of Climate  
1135 Models. *J. Climate*, 28, 952–977, <https://doi.org/10.1175/JCLI-D-14-00353.1>.
- 1136
- 1137 Gutjahr, O., Jungclaus, J. H., Brüggemann, N., Haak, H., and Marotzke, J.: Air-sea interactions and water mass  
1138 transformation during a katabatic storm in the Irminger Sea. *Journal of Geophysical Research: Oceans*, 127,  
1139 e2021JC018075. <https://doi.org/10.1029/2021JC018075>, 2022.
- 1140
- 1141 Hersbach H, Bell B, Berrisford P, et al. (2020). The ERA5 global reanalysis. *Q J R Meteorol Soc.* 146: 1999–2049.  
1142 <https://doi.org/10.1002/qj.3803>
- 1143
- 1144 Hewitt, H., Fox-Kemper, B., Pearson, B. et al. The small scales of the ocean may hold the key to surprises. *Nat. Clim.*  
1145 *Chang.* 12, 496–499 (2022). <https://doi.org/10.1038/s41558-022-01386-6>.
- 1146
- 1147 Hogan, R. J., and A. Bozzo, 2018: A flexible and efficient radiation scheme for the ECMWF model. *J. Adv. Modeling Earth*  
1148 *Sys.*, 10, 1990–2008, <https://doi.org/10.1029/2018MS001364>
- 1149





- 1150 Hohenegger, C., Korn, P., Linardakis, L., Redler, R., Schnur, R., Adamidis, P., Bao, J., Bastin, S., Behraves, M., Bergemann,  
1151 M., Biercamp, J., Bockelmann, H., Brokopf, R., Brüggemann, N., Casaroli, L., Chegini, F., Datsaris, G., Esch, M., George,  
1152 G., Giorgetta, M., Gutjahr, O., Haak, H., Hanke, M., Ilyina, T., Jahns, T., Jungclaus, J., Kern, M., Klocke, D., Kluft, L., Kölling,  
1153 T., Kornblueh, L., Kosukhin, S., Kroll, C., Lee, J., Mauritsen, T., Mehlmann, C., Mieslinger, T., Naumann, A. K., Paccini, L.,  
1154 Peinado, A., Praturi, D. S., Putrasahan, D., Rast, S., Riddick, T., Roeber, N., Schmidt, H., Schulzweida, U., Schütte, F., Segura,  
1155 H., Shevchenko, R., Singh, V., Specht, M., Stephan, C. C., von Storch, J.-S., Vogel, R., Wengel, C., Winkler, M., Ziemann, F.,  
1156 ICON-Sapphire: simulating the components of the Earth System and their interactions at kilometer and subkilometer scales,  
1157 *Geosci. Model Dev.*, <https://doi.org/10.5194/gmd-16-779-2023>, 2023.
- 1158
- 1159 Hutter, N., Bouchat, A., Dupont, F., Dukhovskoy, D., Koldunov, N., Lee, Y. J., et al. (2022). Sea Ice Rheology Experiment  
1160 (SIREx): 2. Evaluating linear kinematic features in high-resolution sea ice simulations. *Journal of Geophysical Research:*  
1161 *Oceans*, 127, e2021JC017666. <https://doi.org/10.1029/2021JC017666>
- 1162
- 1163 Hallberg, R.: Using a resolution function to regulate parameterizations of oceanic mesoscale eddy effects, *Ocean Modelling*,  
1164 Volume 72, 2013, Pages 92-103, ISSN 1463-5003, <https://doi.org/10.1016/j.ocemod.2013.08.007>.
- 1165
- 1166 Hannah, W. M., & Maloney, E. D. (2011). The role of moisture–convection feedbacks in simulating the Madden–Julian  
1167 oscillation. *Journal of Climate*, 24(11), 2754–2770.
- 1168
- 1169 Hogg, A. McC., Meredith, M. P., Chambers, D. P., Abrahamsen, E. P., Hughes, C. W., and Morrison, A. K. (2015). Recent  
1170 trends in the Southern Ocean eddy field, *J. Geophys. Res. Oceans*, 120, 257–267, doi:10.1002/2014JC010470.
- 1171
- 1172 Hortal, M. (2002) The development and testing of a new two-time-level semi-Lagrangian scheme (SETTLES) in the ECMWF  
1173 forecast model. *Quarterly Journal of the Royal Meteorological Society*, 128, 1671–1687.
- 1174 IFS nextGEMS cycle 2 4km 1-year simulation. <https://dx.doi.org/10.21957/1n36-qg55>, 2022.
- 1175 Johnson, S. J., Stockdale, T. N., Ferranti, L., Balmaseda, M. A., Molteni, F., Magnusson, L., Tietsche, S., Decremmer, D.,  
1176 Weisheimer, A., Balsamo, G., Keeley, S. P. E., Mogensen, K., Zuo, H., and Monge-Sanz, B. M.: SEAS5: the new ECMWF  
1177 seasonal forecast system, *Geosci. Model Dev.*, 12, 1087–1117, <https://doi.org/10.5194/gmd-12-1087-2019>, 2019.
- 1178 Jones PW. 1999. First- and second-order conservative remapping schemes for grids in spherical coordi- nates. *Mon. Wea. Rev.*  
1179 127: 2204–2210.



- 1180 Judt, F., Klocke, D., Rios-Berrios, R. et. al. 2021: Tropical Cyclones in Global Storm-Resolving Models, *JMSJ*, II, 2021-029.  
1181 <https://doi.org/10.2151/jmsj.2021-029>  
1182
- 1183 Judt, F., and R. Rios-Berrios, 2021: Resolved convection improves the representation of equatorial waves and tropical rainfall  
1184 variability in a global nonhydrostatic model. *Geophys. Res. Lett.*, 48, e2021GL093265,  
1185 <https://doi.org/10.1029/2021GL093265>.  
1186
- 1187 Jung, T., and Coauthors, 2012: High-Resolution Global Climate Simulations with the ECMWF Model in Project Athena:  
1188 Experimental Design, Model Climate, and Seasonal Forecast Skill. *J. Climate*, 25, 3155–3172, <https://doi.org/10.1175/JCLI->  
1189 [D-11-00265.1](https://doi.org/10.1175/JCLI-D-11-00265.1).  
1190
- 1191 Kluyver, T. et al. 2016: Jupyter notebooks – a publishing format for reproducible computational workflows. In *Positioning*  
1192 *and Power in Academic Publishing: Players, Agents and Agendas*, (eds Loizides, F. & Schmidt, B.) 87–90 (IOS Press, 2016).  
1193
- 1194 Keeley, S.P.E., Sutton, R.T. and Shaffrey, L.C. (2012), The impact of North Atlantic sea surface temperature errors on the  
1195 simulation of North Atlantic European region climate. *Q.J.R. Meteorol. Soc.*, 138: 1774-1783. <https://doi.org/10.1002/qj.1912>.  
1196
- 1197 Kodama, C., Ohno, T., Seiki, T., Yashiro, H., Noda, A. T., Nakano, M., et al. (2021). The nonhydrostatic icosahedral  
1198 atmospheric model for CMIP6 HighResMIP simulations (NICAM16-s): Experimental design, model description, and impacts  
1199 of model updates. *Geoscientific Model Development*, 14(2), 795–820. <https://doi.org/10.5194/gmd-14-795-2021>.  
1200
- 1201 Kodama, C., Yamada, Y., Noda, A. T., Kikuchi, K., Kajikawa, Y., Nasuno, T., et al. (2015). A 20-year climatology of a  
1202 NICAM AMIP-type simulation. *Journal of the Meteorological Society of Japan. Ser. II*, 93(4), 393–424.  
1203 <https://doi.org/10.2151/jmsj.2015-024>.  
1204
- 1205 Koehler, M., Ahlgrimm, M. and Beljaars, A. (2011). Unified treatment of dry convective and stratocumulus-topped boundary  
1206 layers in the ECMWF model. *Q. J. R. Meteorol. Soc.*, 137, 43-57, <https://doi.org/10.1002/qj.713>  
1207
- 1208 Koldunov, N. V., Aizinger, V., Rakowsky, N., Scholz, P., Sidorenko, D., Danilov, S., and Jung, T.: Scalability and some  
1209 optimization of the Finite-volumE Sea ice–Ocean Model, Version 2.0 (FESOM2), *Geosci. Model Dev.*, 12, 3991–4012,  
1210 <https://doi.org/10.5194/gmd-12-3991-2019>, 2019.  
1211



- 1212 Koldunov, Nikolay; Kölling, Tobias; Pedruzo-Bagazgoitia, Xabier; Rackow, Thomas; Redler, René; Sidorenko, Dmitry;  
1213 Wieners, Karl-Hermann; Ziemer, Florian Andreas (2023). nextGEMS: output of the model development cycle 3 simulations  
1214 for ICON and IFS. World Data Center for Climate (WDCC) at DKRZ. [https://doi.org/10.26050/WDCC/nextGEMS\\_cyc3](https://doi.org/10.26050/WDCC/nextGEMS_cyc3)  
1215
- 1216 Kölling, T., Kluff, L., & Rackow, T. (2024). gribscan (v0.0.10). Zenodo. <https://doi.org/10.5281/zenodo.10625189>  
1217
- 1218 Large, W.G., Yeager, S.G. The global climatology of an interannually varying air–sea flux data set. *Clim Dyn* 33, 341–364  
1219 (2009). <https://doi.org/10.1007/s00382-008-0441-3>  
1220
- 1221 Liebmann, B., & Smith, C. A. (1996). Description of a complete (interpolated) outgoing longwave radiation dataset. *Bulletin*  
1222 *of the American Meteorological Society*, 77(6), 1275-1277.  
1223
- 1224 Ling, J., Zhao, Y., & Chen, G. (2019). Barrier effect on MJO propagation by the Maritime Continent in the MJO Task  
1225 Force/GEWEX atmospheric system study models. *Journal of Climate*, 32(17), 5529-5547.  
1226
- 1227 Loeb, N. G., and Coauthors, 2018: Clouds and the Earth’s Radiant Energy System (CERES) Energy Balanced and Filled  
1228 (EBAF) Top-of-Atmosphere (TOA) Edition-4.0 Data Product. *J. Climate*, 31, 895–918, <https://doi.org/10.1175/JCLI-D-17-0208.1>.  
1229
- 1230
- 1231 Loveland, T.R.; Reed, B.C.; Brown, J.F.; Ohlen, D.O.; Zhu, Z.; Young, L.; Merchant, J.W. Development of a global land  
1232 cover characteristics database and IGB6 DISCover from the 1 km AVHRR data. *Int. J. Remote Sens.* 2000, 21, 1303–1330.  
1233
- 1234 Lott, F. and Miller, M. J. (1997). A new subgrid-scale orographic drag parametrization: Its formulation and testing. *Q. J. R.*  
1235 *Meteorol. Soc.*, 123, 101-127, <https://doi.org/10.1002/qj.49712353704>.  
1236
- 1237 Lüpkes, C., T. Vihma, G. Birnbaum, and U. Wacker (2008), Influence of leads in sea ice on the temperature of the  
1238 atmospheric boundary layer during polar night, *Geophys. Res. Lett.*, 35, L03805, doi:10.1029/2007GL032461.  
1239
- 1240 Macdonald, R. W., Griffiths, R. F., & Hall, D. J. (1998). An improved method for the estimation of surface roughness of  
1241 obstacle arrays. *Atmospheric Environment*, 32(11), 1857–1864. [https://doi.org/10.1016/s1352-2310\(97\)00403-2](https://doi.org/10.1016/s1352-2310(97)00403-2)  
1242
- 1243 Madden, R. A., & Julian, P. R. (1972). Description of global-scale circulation cells in the tropics with a 40–50 day period.  
1244 *Journal of Atmospheric Sciences*, 29(6), 1109-1123.



- 1245 Malardel, S., Wedi N., Deconinck W., Diamantakis M., Kuehnlein C., Mozdzyński G., Hamrud M., Smolarkiewicz P.: A  
1246 new grid for the IFS. ECMWF Newsletter 146:23–28. <https://doi.org/doi:10.21957/zwdu9u5i.>, 2016  
1247
- 1248 Marti, O., Nguyen, S., Braconnot, P., Valcke, S., Lemarié, F., & Blayo, E. (2021). A Schwarz iterative method to evaluate  
1249 ocean–atmosphere coupling schemes: implementation and diagnostics in IPSL-CM6-SW-VLR. *Geoscientific Model  
1250 Development*, 14(5), 2959-2975.  
1251
- 1252 McNorton, J. R., Arduini, G., Boussez, N., Agustí-Panareda, A., Balsamo, G., Boussetta, S., et al. (2021). An urban  
1253 scheme for the ECMWF integrated forecasting system: Single-column and global offline application. *Journal of Advances in  
1254 Modeling Earth Systems*, 13, e2020MS002375. <https://doi.org/10.1029/2020MS002375>  
1255
- 1256 McNorton, J., Agustí-Panareda, A., Arduini, G., Balsamo, G., Boussez, N., Boussetta, S., et al. (2023). An urban scheme  
1257 for the ECMWF Integrated forecasting system: Global forecasts and residential CO<sub>2</sub> emissions. *Journal of Advances in  
1258 Modeling Earth Systems*, 15, e2022MS003286. <https://doi.org/10.1029/2022MS003286>  
1259
- 1260 Miyakawa, T., H. Yashiro, T. Suzuki, H. Tatebe, and M. Satoh (2017), A Madden-Julian Oscillation event remotely  
1261 accelerates ocean upwelling to abruptly terminate the 1997/1998 super El Niño, *Geophys. Res. Lett.*, 44, 9489–9495,  
1262 doi:10.1002/2017GL074683.  
1263
- 1264 Miura, H., Satoh, M., Nasuno, T., Noda, A. T., & Oouchi, K. (2007). A Madden-Julian oscillation event realistically  
1265 simulated by a global cloud-resolving model. *Science*, 318(5857), 1763-1765.  
1266
- 1267 Mogensen, K. S., Magnusson, L., and Bidlot, J.-R.: Tropical cyclone sensitivity to ocean coupling in the ECMWF coupled  
1268 model, *J. Geophys. Res. Oceans*, 122, 4392– 4412, doi:10.1002/2017JC012753., 2017.  
1269
- 1270 Mogensen, K. S., Keeley, S., and Towers, P. (2012): Coupling of the NEMO and IFS models in a single executable,  
1271 ECMWF Technical Memorandum, 673, <https://doi.org/10.21957/rfplwzuol>  
1272
- 1273 Morrison, A. K., Hogg, A. McC., England, M. H., Spence, P.: Warm Circumpolar Deep Water transport toward Antarctica  
1274 driven by local dense water export in canyons, *Science Advances*, eaav2516, V6, N18 doi:10.1126/sciadv.aav2516, 2020.  
1275
- 1276 Mu, L., Nerger, L., Tang, Q., Loza, S. N., Sidorenko, D., Wang, Q., Semmler, T., Zampieri, L., Losch, M., & Goessling H.  
1277 F. (2020). Toward a data assimilation system for seamless sea ice prediction based on the AWI Climate Model. *Journal of  
1278 Advances in Modeling Earth Systems*, 12, e2019MS001937. DOI:10.1029/2019MS001937



- 1279
- 1280 Mu, L., Nerger, L., Streffing, J., Tang, Q., Niraula, B., Zampieri, L., Loza, S. L., Goessling, H. F. (2022) Sea-ice forecasts  
1281 with an upgraded AWI Coupled Prediction System. *Journal of Advances in Modeling Earth Systems*, e2022MS003176.  
1282 DOI:10.1029/2022MS003176
- 1283
- 1284 Müller, A., W. Deconinck, C. Kühnlein, G. Mengaldo, M. Lange, N. Wedi, P. Bauer et al., 2019: The ESCAPE project:  
1285 Energy-efficient Scalable Algorithms for Weather Prediction at Exascale. *Geosci. Model Dev.*, 12, 4425–4441,  
1286 <https://doi.org/10.5194/gmd-12-4425-2019>.
- 1287
- 1288 Nogueira, M., Boussetta, S., Balsamo, G., Albergel, C., Trigo, I. F., Johannsen, F., et al. (2021). Upgrading land-cover and  
1289 vegetation seasonality in the ECMWF coupled system: Verification with FLUXNET sites, METEOSAT satellite land  
1290 surface temperatures, and ERA5 atmospheric reanalysis. *Journal of Geophysical Research: Atmospheres*, 126,  
1291 e2020JD034163. <https://doi.org/10.1029/2020JD034163>.
- 1292
- 1293 Orr, A., Bechtold, P., Scinocca, J. F., Ern, M. and Janiskova, M. (2010). Improved middle atmosphere climate and forecasts  
1294 in the ECMWF model through a non-orographic gravity wave drag parametrization. *J. Climate*, 23, 5905-5926.,  
1295 <https://doi.org/10.1175/2010JCLI3490.1>.
- 1296
- 1297 OSI SAF Global sea ice concentration climate data record 1978-2020 (v3.0, 2022), OSI-450-a,  
1298 doi:10.15770/EUM\_SAF\_OSI\_0013. EUMETSAT Ocean and Sea Ice Satellite Application Facility. Data extracted from  
1299 OSI SAF FTP server: year 2020, Arctic and Antarctic data, accessed 03.01.2024
- 1300
- 1301 Overland, J. E., T. B. Curtin, and W. O. Smith Jr. (1995), Preface [to special section on Leads and Polynyas], *J. Geophys.*  
1302 *Res.*, 100(C3), 4267–4268, doi:10.1029/95JC00336.
- 1303
- 1304 Palmer, T. Climate forecasting: Build high-resolution global climate models. *Nature* 515, 338–339 (2014).  
1305 <https://doi.org/10.1038/515338a>
- 1306 Palmer, T., and Stevens, B. (2019): The scientific challenge of understanding and estimating climate change, *PNAS* 116  
1307 (49), 24390-24395, <https://doi.org/10.1073/pnas.1906691116>
- 1308
- 1309 Paul, M. J., & Meyer, J. L. (2001). Streams in the urban landscape. *Annual Review of Ecology and Systematics*, 32(1), 333–  
1310 365. <https://doi.org/10.1146/annurev.ecolsys.32.081501.114040>
- 1311





- 1312 Polichtchouk, I., Wedi, N. & Kim, Y.-H.(2021) Resolved gravity waves in the tropical stratosphere: Impact of horizontal  
1313 resolution and deep convection parametrization. *Q J R Meteorol Soc*, 148(742), 233–251. Available from:  
1314 <https://doi.org/10.1002/qj.4202>  
1315
- 1316 Prein, A. F., Langhans, W., Fossier, G., Ferrone, A., Ban, N., Goergen, K., Keller, M., Tölle, M., Gutjahr, O., Feser, F.,  
1317 Brisson, E., Kollet, S., Schmidli, J., van Lipzig, N. P. M., and Leung, R.: A review on regional convection-permitting  
1318 climate modeling: Demonstrations, prospects, and challenges, *Rev. Geophys.*, 53, 323–361, 2015.  
1319
- 1320 Randall, D. A., and K. Emanuel, 2024: The Weather–Climate Schism. *Bull. Amer. Meteor. Soc.*, 105, E300–E305,  
1321 <https://doi.org/10.1175/BAMS-D-23-0124.1>.  
1322
- 1323 Rackow, T., Sein, D. V., Semmler, T., Danilov, S., Koldunov, N. V., Sidorenko, D., Wang, Q., and Jung, T.: Sensitivity of  
1324 deep ocean biases to horizontal resolution in prototype CMIP6 simulations with AWI-CM1.0, *Geosci. Model Dev.*, 12,  
1325 2635–2656, <https://doi.org/10.5194/gmd-12-2635-2019>, 2019.  
1326
- 1327 Rackow, T., Danilov, S., Goessling, H.F. et al.: Delayed Antarctic sea-ice decline in high-resolution climate change  
1328 simulations. *Nat Commun* 13, 637, <https://doi.org/10.1038/s41467-022-28259-y>, 2022.  
1329
- 1330 Rackow, T., Pedruzo-Bagazgoitia, X., & Becker, T. (2023a). Namelist files and settings for multi-year km-scale nextGEMS  
1331 Cycle 3 simulations with IFS-FESOM/NEMO. Zenodo. <https://doi.org/10.5281/zenodo.10221652>  
1332
- 1333 Rackow, T., Becker, T., Forbes, R., & Fielding, M. (2023b). Source code changes to the Integrated Forecasting System (IFS)  
1334 for nextGEMS simulations. Zenodo. <https://doi.org/10.5281/zenodo.10223577>  
1335
- 1336 Rackow, T., Hegewald, J., Koldunov, N. V., Mogensen, K., Scholz, P., Sidorenko, D., & Streffing, J. (2023c). FESOM2.5  
1337 source code used in nextGEMS Cycle 3 simulations with IFS-FESOM. Zenodo. <https://doi.org/10.5281/zenodo.10225420>  
1338
- 1339 Saavedra Garfias, P., Kalesse-Los, H., von Albedyll, L., Griesche, H., and Spreen, G.: Asymmetries in cloud microphysical  
1340 properties ascribed to sea ice leads via water vapour transport in the central Arctic, *Atmos. Chem. Phys.*, 23, 14521–14546,  
1341 <https://doi.org/10.5194/acp-23-14521-2023>, 2023.  
1342
- 1343 Sámány, D., Valentini, M., Smart, S., Razvan, A., Geier, P., Hawkes, J., Quintino, T.: MultiIO: A framework for message-  
1344 driven data routing for weather and climate simulations. Submitted to Proceedings of the Platform for Advanced Scientific  
1345 Computing Conference, 2024.



- 1346
- 1347 Satoh, M., Stevens, B., Judt, F. et al. Global Cloud-Resolving Models. *Curr Clim Change Rep*5, 172–184 (2019).
- 1348 <https://doi.org/10.1007/s40641-019-00131-0>
- 1349
- 1350 Scaife, A. A., Baldwin, M. P., Butler, A. H., Charlton-Perez, A. J., Domeisen, D. I. V., Garfinkel, C. I., Hardiman, S. C.,
- 1351 Haynes, P., Karpechko, A. Y., Lim, E.-P., Noguchi, S., Perlwitz, J., Polvani, L., Richter, J. H., Scinocca, J., Sigmond, M.,
- 1352 Shepherd, T. G., Son, S.-W., and Thompson, D. W. J.: Long-range prediction and the stratosphere, *Atmos. Chem. Phys.*, 22,
- 1353 2601–2623, <https://doi.org/10.5194/acp-22-2601-2022>, 2022.
- 1354
- 1355 Schär, C., and Coauthors, 2020: Kilometer-Scale Climate Models: Prospects and Challenges. *Bull. Amer. Meteor. Soc.*, 101,
- 1356 E567–E587, <https://doi.org/10.1175/BAMS-D-18-0167.1>.
- 1357
- 1358 Scholz, P., Sidorenko, D., Gurses, O., Danilov, S., Koldunov, N., Wang, Q., Sein, D., Smolentseva, M., Rakowsky, N., and
- 1359 Jung, T.: Assessment of the Finite-volume Sea ice-Ocean Model (FESOM2.0) – Part 1: Description of selected key model
- 1360 elements and comparison to its predecessor version, *Geosci. Model Dev.*, 12, 4875–4899, [https://doi.org/10.5194/gmd-12-](https://doi.org/10.5194/gmd-12-4875-2019)
- 1361 [4875-2019](https://doi.org/10.5194/gmd-12-4875-2019), 2019.
- 1362
- 1363 Schulthess, T. C., P. Bauer, N. Wedi, O. Fuhrer, T. Hoefler, and C. Schär, 2019: Reflect- ing on the goal and baseline for
- 1364 exascale computing: A roadmap based on weather and climate simulations. *Comput. Sci. Eng.*, 21, 30–41,
- 1365 <https://doi.org/10.1109/MCSE.2018.2888788>.
- 1366
- 1367 Sein, D. V., Koldunov, N. V., Danilov, S., Wang, Q., Sidorenko, D., Fast, I., ... Jung, T. (2017). Ocean modeling on a mesh
- 1368 with resolution following the local Rossby radius. *Journal of Advances in Modeling Earth Systems*, 9, 2601–2614.
- 1369 <https://doi.org/10.1002/2017MS001099>
- 1370
- 1371 Selivanova, J., Iovino, D., and Cocetta, F.: Past and future of the Arctic sea ice in HighResMIP climate models, EGU sphere
- 1372 [preprint], <https://doi.org/10.5194/egusphere-2023-1411>, 2023.
- 1373
- 1374 Sidorenko, D., Goessling, H. F., Koldunov, N. V., Scholz, P., Danilov, S., Barbi, D., et al ( 2019). Evaluation of FESOM2.0
- 1375 coupled to ECHAM6.3: Pre-industrial and HighResMIP simulations. *Journal of Advances in Modeling Earth Systems*, 11.
- 1376 <https://doi.org/10.1029/2019MS001696>.
- 1377
- 1378 Siebesma, A. P., Soares, P. M., & Teixeira, J. (2007). A combined eddy-diffusivity mass-flux approach for the convective
- 1379 boundary layer. *J. Atmos. Sc.*, 64(4), 1230-1248, <https://doi.org/10.1175/JAS3888.1>



- 1380
- 1381 Simmons, A. J. and Strüfing, R.: Numerical forecasts of stratospheric warming events using a model with a hybrid vertical
- 1382 coordinate, *Q. J. Roy. Meteor. Soc.*, 109, 81–111, <https://doi.org/10.1002/qj.49710945905>, 1983.
- 1383
- 1384 Smart, S., Quintino, T., Quintino, T.: A Scalable Object Store for Meteorological and Climate Data. In *Proceedings of the*
- 1385 *Platform for Advanced Scientific Computing Conference*, 1–8, 2017.
- 1386
- 1387 Stephan, C. C., Strube, C., Klocke, D., Ern, M., Hoffmann, L., Preusse, P., & Schmidt, H. (2019). Gravity waves in
- 1388 global high-resolution simulations with explicit and parameterized convection. *Journal of Geophysical Research:*
- 1389 *Atmospheres*, 124, 4446–4459. <https://doi.org/10.1029/2018JD030073>
- 1390
- 1391 Stephan, C.C., Žagar, N. & Shepherd, T.G.(2021) Waves and coherent flows in the tropical atmosphere: New
- 1392 opportunities, old challenges. *Q J R Meteorol Soc*, 147: 2597–2624. Available from: <https://doi.org/10.1002/qj.4109>
- 1393
- 1394 Stevens, B., Sherwood, S.C., Bony, S. and Webb, M.J. (2016), Prospects for narrowing bounds on Earth's equilibrium
- 1395 climate sensitivity. *Earth's Future*, 4: 512-522. <https://doi.org/10.1002/2016EF000376>
- 1396
- 1397 Stevens, B., Satoh, M., Auger, L., Biercamp, J., Bretherton, C.S., Chen, X., Düben, P., Judt, F., Khairoutdinov, M., Klocke,
- 1398 D., Kodama, C., Kornblueh, L., Lin, S.-L., Putman, W., Shibuya, R., Neumann, P., Röber, N., Vannier, B., Vidale, P.-L.,
- 1399 Wedi, N. and Zhou, L. (2019) DYAMOND: the DYnamics of the Atmospheric general circulation Modeled On Non-
- 1400 hydrostatic Domains. *Progress in Earth and Planetary Science*, 6(1), 61. <https://doi.org/10.1186/s40645-019-0304-z>.
- 1401
- 1402 Stockdale, TN, Kim, Y-H, Anstey, JA, et al. Prediction of the quasi-biennial oscillation with a multi-model ensemble of
- 1403 QBO-resolving models. *Q J R Meteorol Soc.* 2022; 148(744), 1519–1540. <https://doi.org/10.1002/qj.3919>
- 1404
- 1405 Streffing, J., Semmler, T., Zampieri, L., & Jung, T. (2021). Response of Northern Hemisphere Weather and Climate to
- 1406 Arctic Sea Ice Decline: Resolution Independence in Polar Amplification Model Intercomparison Project (PAMIP)
- 1407 Simulations, *Journal of Climate*, 34(20), 8445–8457. DOI:10.1175/JCLI-D-19-1005.1
- 1408
- 1409 Streffing, J., Sidorenko, D., Semmler, T., Zampieri, L., Scholz, P., Andrés-Martínez, M., Koldunov, N., Rackow, T.,
- 1410 Kjellsson, J., Goessling, H., Athanase, M., Wang, Q., Hegewald, J., Sein, D. V., Mu, L., Fladrich, U., Barbi, D., Gierz, P.,
- 1411 Danilov, S., Juricke, S., Lohmann, G., and Jung, T.: AWI-CM3 coupled climate model: description and evaluation
- 1412 experiments for a prototype post-CMIP6 model, *Geosci. Model Dev.*, 15, 6399–6427, [https://doi.org/10.5194/gmd-15-6399-](https://doi.org/10.5194/gmd-15-6399-2022)
- 1413 2022, 2022.



- 1414
- 1415 Suematsu, T., & Miura, H. (2018). Zonal SST difference as a potential environmental factor supporting the longevity of the
- 1416 Madden–Julian oscillation. *Journal of Climate*, 31(18), 7549-7564.
- 1417
- 1418 Takasuka, D., & Satoh, M. (2020). Dynamical roles of mixed Rossby–gravity waves in driving convective initiation and
- 1419 propagation of the Madden–Julian oscillation: General views. *Journal of the Atmospheric Sciences*, 77(12), 4211-4231.
- 1420
- 1421 Takasuka, D., Kodama, C., Suematsu, T., Ohno, T., Yamada, Y., Seiki, T., et al. (2024). How can we improve the seamless
- 1422 representation of climatological statistics and weather toward reliable global K-scale climate simulations? *Journal of*
- 1423 *Advances in Modeling Earth Systems*, 16, e2023MS003701. <https://doi.org/10.1029/2023MS003701>.
- 1424
- 1425 Takayabu, Y. N. (1994). Large-scale cloud disturbances associated with equatorial waves Part I: Spectral features of the
- 1426 cloud disturbances. *Journal of the Meteorological Society of Japan. Ser. II*, 72(3), 433-449.
- 1427
- 1428 Taylor, M., Peter M. Caldwell, Luca Bertagna, Conrad Clevenger, Aaron Donahue, James Foucar, Oksana Guba, Benjamin
- 1429 Hillman, Noel Keen, Jayesh Krishna, Matthew Norman, Sarat Sreepathi, Christopher Terai, James B. White, Andrew G
- 1430 Salinger, Renata B McCoy, Lai-yung Ruby Leung, David C. Bader, and Danqing Wu. 2023. The Simple Cloud-Resolving
- 1431 E3SM Atmosphere Model Running on the Frontier Exascale System. In *Proceedings of the International Conference for*
- 1432 *High Performance Computing, Networking, Storage and Analysis (SC '23)*. Association for Computing Machinery, New
- 1433 York, NY, USA, Article 7, 1–11. <https://doi.org/10.1145/3581784.3627044>
- 1434
- 1435 Temperton, C., Hortal, M. and Simmons, A.J.: A two-time-level semi-Lagrangian global spectral model. *Quarterly Journal*
- 1436 *of the Royal Meteorological Society*, 127, 111– 127. <http://dx.doi.org/10.1002/qj.49712757107>, 2001.
- 1437
- 1438 Tiedtke, M. (1989). A comprehensive mass flux scheme for cumulus parametrization in large-scale models. *Mon. Wea. Rev.*,
- 1439 117, 1779-1800, [https://doi.org/10.1175/1520-0493\(1989\)117<1779:ACMFSF>2.0.CO;2](https://doi.org/10.1175/1520-0493(1989)117<1779:ACMFSF>2.0.CO;2).
- 1440
- 1441 Tiedtke, M. (1993). Representation of clouds in large-scale models. *Mon. Wea. Rev.*, 121, 3040-3061,
- 1442 [https://doi.org/10.1175/1520-0493\(1993\)121<3040:ROCILS>2.0.CO;2](https://doi.org/10.1175/1520-0493(1993)121<3040:ROCILS>2.0.CO;2).
- 1443
- 1444 Tomita, H., Miura, H., Iga, S.-I., Nasuno, T., & Satoh, M. (2005). A global cloud-resolving simulation: Preliminary results
- 1445 from an aqua planet experiment. *Geophysical Research Letters*, 32(8), L08805. <https://doi.org/10.1029/2005gl022459>.
- 1446



- 1447 Trigo, I.F., Monteiro, I.T., Olesen, F., Kabsch, E.: An assessment of remotely sensed land surface temperature. *J. Geophys.*  
1448 *Res.* 113, 1–12. <https://doi.org/10.1029/2008JD010035>, 2008.
- 1449
- 1450 Untch, A. and Hortal, M.: A finite-element scheme for the vertical discretization of the semi-Lagrangian version of the  
1451 ECMWF forecast model. *Quarterly Journal of the Royal Meteorological Society*, 130, 1505– 1530.  
1452 <http://dx.doi.org/10.1256/qj.03.173>, 2004.
- 1453
- 1454 van Westen, R. M., and Dijkstra, H. A.: Ocean eddies strongly affect global mean sea-level projections. *Sci. Adv.* 7  
1455 , eabf1674(2021). DOI:10.1126/sciadv.abf1674
- 1456
- 1457 Vivoda, J., P. Smolřková, and J. Simarro, 2018: Finite Elements Used in the Vertical Discretization of the Fully  
1458 Compressible Core of the ALADIN System. *Mon. Wea. Rev.*, 146, 3293–3310, <https://doi.org/10.1175/MWR-D-18-0043.1>.
- 1459
- 1460 von Albedyll, L., Hendricks, S., Hutter, N., Murashkin, D., Kaleschke, L., Willmes, S., Thielke, L., Tian-Kunze, X., Spreen,  
1461 G., and Haas, C.: Lead fractions from SAR-derived sea ice divergence during MOSAiC, *The Cryosphere Discuss.* [preprint],  
1462 <https://doi.org/10.5194/tc-2023-123>, in review, 2023.
- 1463
- 1464 Wang, C., Zhang, L., Lee, SK. et al.: A global perspective on CMIP5 climate model biases. *Nature Clim Change* 4, 201–205,  
1465 <https://doi.org/10.1038/nclimate2118>, 2014.
- 1466
- 1467 Wedi, N. P.: Increasing horizontal resolution in numerical weather prediction and climate simulations: Illusion or panacea?,  
1468 *Philos. T. Roy. Soc. A*, 372, 20130289, <https://doi.org/10.1098/rsta.2013.0289>, 2014.
- 1469
- 1470 Wedi, N.P., Polichtchouk, I., Dueben, P., Anantharaj, V.G., Bauer, P., Boussetta, S., Browne, P., Deconinck, W., Gaudin,  
1471 W., Hadade, I., Hatfield, S., Iffrig, O., Lopez, P., Maciel, P., Mueller, A., Saarinen, S., Sandu, I., Quintino, T. and Vitart, F.  
1472 (2020) A baseline for global weather and climate simulations at 1 km resolution. *Journal of Advances in Modeling Earth*  
1473 *Systems*, 12(11). <https://doi.org/10.1029/2020MS002192>.
- 1474
- 1475 Wengel, C., Lee, SS., Stuecker, M.F. et al. Future high-resolution El Niño/Southern Oscillation dynamics. *Nat. Clim. Chang.*  
1476 11, 758–765 (2021). <https://doi.org/10.1038/s41558-021-01132-4>
- 1477
- 1478 Wheeler, M., & Kiladis, G. N. (1999). Convectively coupled equatorial waves: Analysis of clouds and temperature in the  
1479 wavenumber–frequency domain. *Journal of the Atmospheric Sciences*, 56(3), 374-399.
- 1480





- 1481 Wieners, Karl-Hermann; Ziemen, Florian Andreas; Koldunov, Nikolay; Pedruzo-Bagazgoitia, Xabier; Rackow, Thomas;  
1482 Redler, René; Sidorenko, Dmitry; Kölling, Tobias (2023). nextGEMS: output of the model development cycle 2 simulations  
1483 for ICON and IFS. World Data Center for Climate (WDCC) at DKRZ. [https://doi.org/10.26050/WDCC/nextGEMS\\_cyc2](https://doi.org/10.26050/WDCC/nextGEMS_cyc2)  
1484 Yano, J.-I. and Wedi, N. P.: Sensitivities of the Madden–Julian oscillation forecasts to configurations of physics in the  
1485 ECMWF global model, *Atmos. Chem. Phys.*, 21, 4759–4778, <https://doi.org/10.5194/acp-21-4759-2021>, 2021.  
1486  
1487 Zampieri, L., Goessling, H. F., & Jung, T. (2018). Bright prospects for Arctic sea ice prediction on subseasonal time scales.  
1488 *Geophysical Research Letters*, 45, 9731–9738. DOI: 10.1029/2018GL079394  
1489  
1490 Zampieri, L., Goessling, H. F., & Jung, T. (2019). Predictability of Antarctic sea ice edge on subseasonal time scales.  
1491 *Geophysical Research Letters*, 46, 9719–9727. DOI: 10.1029/2019GL084096  
1492  
1493 Zhang, C. (2013). Madden–Julian oscillation: Bridging weather and climate. *Bulletin of the American Meteorological*  
1494 *Society*, 94(12), 1849-1870.  
1495  
1496 Zsoter E, Arduini G, Prudhomme C, Stephens E, Cloke H. Hydrological Impact of the New ECMWF Multi-Layer Snow  
1497 Scheme. *Atmosphere*. 2022; 13(5):727. <https://doi.org/10.3390/atmos13050727>